

The Old Dalby landslide: rock physics and electrical resistivity tomography monitoring

Auteur : Guérin, Alexis

Promoteur(s) : Nguyen, Frederic

Faculté : Faculté des Sciences appliquées

Diplôme : Master en ingénieur civil des mines et géologue, à finalité spécialisée en géologie de l'ingénieur et de l'environnement

Année académique : 2017-2018

URI/URL : <http://hdl.handle.net/2268.2/4635>

Avertissement à l'attention des usagers :

Tous les documents placés en accès ouvert sur le site le site MatheO sont protégés par le droit d'auteur. Conformément aux principes énoncés par la "Budapest Open Access Initiative"(BOAI, 2002), l'utilisateur du site peut lire, télécharger, copier, transmettre, imprimer, chercher ou faire un lien vers le texte intégral de ces documents, les disséquer pour les indexer, s'en servir de données pour un logiciel, ou s'en servir à toute autre fin légale (ou prévue par la réglementation relative au droit d'auteur). Toute utilisation du document à des fins commerciales est strictement interdite.

Par ailleurs, l'utilisateur s'engage à respecter les droits moraux de l'auteur, principalement le droit à l'intégrité de l'oeuvre et le droit de paternité et ce dans toute utilisation que l'utilisateur entreprend. Ainsi, à titre d'exemple, lorsqu'il reproduira un document par extrait ou dans son intégralité, l'utilisateur citera de manière complète les sources telles que mentionnées ci-dessus. Toute utilisation non explicitement autorisée ci-avant (telle que par exemple, la modification du document ou son résumé) nécessite l'autorisation préalable et expresse des auteurs ou de leurs ayants droit.

UNIVERSITY OF LIEGE
FACULTY OF APPLIED SCIENCES



The Old Dalby landslide: rock physics and electrical resistivity tomography monitoring

MASTER THESIS CONDUCTED FOR OBTAINING THE MASTER'S DEGREE IN MINING AND
GEOLOGICAL ENGINEERING BY ALEXIS GUÉRIN

supervised by Dr. Frédéric NGUYEN¹

Academic year 2017-2018

¹University of Liège, Faculty of Applied Sciences

Acknowledgments

First of all, I would like to thank particularly my supervisor, Dr Frédéric Nguyen, who advised me to do my internship at the British Geological Survey (BGS). He followed me since the beginning of my study and showed a great interest in my work. He was very good advice when I was blocking on certain points and was very helpful to me to synthesize my work. He carefully proofread the whole master thesis, what was extremely useful for the finalization of my work.

I would like to thank Dr Jonathan Chambers for accepting me at the British Geological Survey and for introducing me to the geophysical team. He showed great interest in my work and made my integration to the team very easy. I must say that I keep a very good memory of my stay at the BGS and that I miss a lot of people that I have met there.

I would like to thank all the people that have helped me during my stay at the British Geological Survey. In this particular Sebastian Uhlemann who has always been extremely available to help me in the processing of my data, and made it possible for me to run my inversion on the servers of the BGS even when I returned to Belgium. I also want to thank Matthew Kirkham for the time he has spent helping me in the lab, for his constant good mood and for introducing me to the coffee table at 11 AM, all the conversations really helped me improving my English. I am very grateful for the help from Dr. Ben Dashwood and Dr. David Gunn who have always showed great interest in my study and were always very helpful to clarify details related to the study of the Old Dalby site.

I thank the British Geological Survey for giving me the access to the monitoring data from Old Dalby, without the thesis would not have been possible.

In the same way, I really thank Annie Royen, who has always helped me stay motivated and provided a careful proofreading of my work.

And finally, I thank my family, especially my parents, who always supported me during my studies.

Abstract

Unexpected landslide failure can cause major damage, including human casualties. This study aims to prevent the risk of failure in a relict landslide located in a railway cutting by monitoring the subsoil saturation. The site is equipped with the PRIME system, a tool developed at the BGS to provide real-time 4D electrical resistivity monitoring. The subsoil is composed of Quaternary tills followed by a succession of Triassic mudstone of poor geotechnical characteristics. Laboratory characterization was realized on samples from boreholes drilled on site. It includes Atterberg limits, particle size analysis, resistivity-moisture measurements and suction-moisture measurements. The study of the resistivity at low moisture content highlighted the need to account for the residual water saturation in Waxman-Smits equation. From the 5TE probes installed in-situ, we proved that the parameters of the Waxman-Smits modelling varied in space. A new approach based on saturated resistivity mapping was applied to consider local heterogeneity of the subsoil in Waxman-Smits modelling. The Waxman-Smits modelling was established on both laboratory and in-situ measurements, which proved that the 5TE measurements could be used to fit a Waxman-Smits model. This new approach proved to greatly enhance the quality of the ERT-derived saturation modelling. We observed that there was a very high correlation between the cumulative effective infiltration and the ERT-derived saturation measurements. Especially, it was pointed out that the dynamic of the subsoil was restricted to the first three meters of subsoil and that, at higher depth, the subsoil was staying close to full saturation.

Résumé

Une rupture de glissement de terrain inattendue peut causer des dommages importants, y compris des pertes humaines. Cette étude vise à prévenir le risque de rupture d'un glissement de terrain anciennement actif situé dans une section de chemin de fer. Le site est équipé du système PRIME, un outil développé au BGS pour fournir un monitoring 4D de la résistivité électrique en temps réel. Le sous-sol est composé de tills du quaternaire suivis d'une succession d'argile du triassique. Des échantillons de carottes de forage extraites sur site ont été utilisés en laboratoire pour caractériser le sous-sol. L'étude comprend l'évaluation des limites d'Atterberg, une analyse granulométrique, des mesures de résistivité-humidité et des mesures d'humidité-suction. L'étude de la résistivité à faible teneur en eau a mis en évidence la nécessité de prendre en compte la saturation résiduelle de l'eau dans l'équation de Waxman-Smits. Sur base des sondes 5TE installées in situ, nous avons prouvé que les paramètres de la modélisation de Waxman-Smits variaient dans l'espace. Une nouvelle approche basée sur l'évaluation de la résistivité à saturation a été appliquée afin de tenir compte de l'hétérogénéité locale du sous-sol dans la modélisation de Waxman-Smits. La modélisation a été établie sur base des mesures en laboratoire et in situ, ce qui a permis de prouver que les mesures 5TE pouvaient être utilisées pour établir un modèle de Waxman-Smits. Cette nouvelle approche a permis d'améliorer la qualité du monitoring de la saturation du sous-sol. Nous avons ainsi pu montrer l'existence d'une très forte corrélation entre l'infiltration efficace et les valeurs de saturation converties sur base de l'ERT. En particulier, il a été montré que la dynamique du sous-sol était limitée aux trois premiers mètres du sous-sol et qu'à plus haute profondeur le sous-sol restait proche de sa pleine saturation.

Contents

1	Introduction	10
1.1	Landslide issues	10
1.2	The role of geophysical methods	10
1.3	The Old Dalby case study	11
2	Geology of East Midlands	14
2.1	Global setting	14
2.1.1	Triassic deposits	14
2.1.2	Mudstone deposition	15
2.1.3	Folding and faulting	16
2.2	Quaternary	17
2.2.1	Tills deposition	17
3	Theory	19
3.1	Core Characterization	19
3.1.1	Non contact resistivity	19
3.1.2	Galvanic	20
3.1.3	5TE	22
3.2	Atterberg limits	22
3.2.1	Liquid limit	23
3.2.2	Plastic limit	24
3.2.3	Plasticity index	25
3.3	Particle size analysis	25
3.3.1	Procedure	25
3.4	Compacted samples preparation	25
3.4.1	Generalities	25
3.4.2	Samples preparation	26
3.5	Resistivity-moisture content characterization	26
3.5.1	Archie's law	26
3.5.2	Waxman-Smits model	27
3.6	Soil-moisture characteristic curve	28
3.6.1	Soil Suction	28
3.6.2	Soil-moisture characteristic curve - Van Genutchen model	30
3.7	Site investigation	30
3.7.1	Electrical resistivity tomography	30
3.7.2	Inversion	30
3.7.3	Effect of temperature on resistivity	35

4	Old Dalby landslide study site	37
4.1	General presentation	37
4.2	Local geology	37
4.3	Core characterization	38
4.3.1	Geological log	38
4.3.2	Resistivity measurements on core	38
4.4	Landslide mechanism and activity	43
4.5	Monitoring (Prime System)	45
5	Laboratory characterization	46
5.1	Atterberg limits	46
5.1.1	Liquid limit	46
5.1.2	Plastic limit	46
5.1.3	Plasticity index	46
5.2	Particle size analysis	47
5.3	Resistivity-moisture content characterization	47
5.3.1	Resistivity coffins preparation	47
5.3.2	Measurements	49
5.4	Waxman-Smits	50
6	Field investigation	54
6.1	Data processing	54
6.2	Electrical resistivity monitoring data	54
6.2.1	Number of measurements vs. time	54
6.2.2	Resistance vs. time	56
6.2.3	Data error analysis	58
6.3	Rainfall and air temperature monitoring	58
6.4	5TE monitoring	58
6.4.1	Temperature modelling	62
6.5	Effect of water infiltration on 5TE based soil moisture	64
6.6	Reliability of 5TE based VMC/resistivity measurements for Waxman-Smits model fitting	67
6.7	Normalization of the Waxman-Smits model	68
6.7.1	Resistivity normalization	68
6.7.2	Normalization of the saturation	73
6.8	Importance of residual water saturation in Waxman-Smits model	73
6.9	Resistivity error model for weighted data fitting	76
7	Results	79
7.1	In-situ Waxman-Smits model	79
7.1.1	Data selection	79
7.1.2	Fitting of the model	80
7.2	Inversion results	83
7.2.1	Inversion parameters	83
7.2.2	Saturation imaging	83
7.2.3	Study of the decrease between June and September	85
7.3	Suction monitoring	88
8	Conclusions and recommendations for future works	90
9	Glossary of terms	92

A	Water in soils	97
B	Old Dalby geological log	98

1.1	Overview of the data processing from the laboratory and field data acquisition to the saturation and soil suction imaging	11
1.2	ERT-derived saturation imaging of the Old Dalby relict landslide	12
1.3	Comparison between the cumulative infiltration measured at the weather station and the mean ERT-derived saturation from the top 3 meters of Line 2	13
2.1	Lithostratigraphy of the East Midlands (Hobbs et al., 2002)	14
2.2	Permo-Trassic regional tectonic framework of the North Atlantic region, after Warrington and Ivimey-Cook (1992) & Hobbs et al. (2002)	15
2.3	Triassic lithofacies in England and the Southern North Sea, after Warrington and Ivimey-Cook (1992) & Hobbs et al. (2002)	16
2.4	Minor fault in the Cropwell Bishop and Blue Anchor formations. Westbury Formation is exposed at the top right section. Cropwell Bishop, Nottinghamshire (after Hobbs et al., 2002)	16
2.5	Extent of the last glaciations in Great Britain (after Gibbard and Clark (2011))	18
3.1	Non contact resistivity measurement assembly	19
3.2	NaCl cores used to calibrate the non contact resistivity device	20
3.3	Calibration of the non-contact resistivity measurements	20
3.4	Power fit law used to convert non contact resistivity measurements into resistivity	21
3.5	ABEM Terrameter SAS 300C (left) and 5TE probe (right)	21
3.6	Cone penetrometer used to evaluate liquid limit	23
3.7	Potential of soil water, water in plant cell and water in the atmosphere, from (Hartmann, 2003)	29
3.8	Common resistivity of rocks, soils and minerals (Loke, 1999)	31
3.9	Characteristics of different 2D arrays configurations types (from Sharma and Verma, 2015)	32
4.1	Location and geology of Old Dalby	37
4.2	Old Dalby material for laboratory testing	38
4.3	Old Dalby core. Comparison of the non contact resistivity imaging, with the galvanic resistivity measurements and the 5TE resistivity and moisture measurements	43
4.4	Old Dalby landslide geological context	44
4.5	Prime system principle	45
5.1	Liquid limit	47
5.2	Old Dalby Particle Size Analysis	48
5.3	Samples cutting in proctor mould	49
5.4	Resistivity coffins	49
5.5	Resistivity-Moisture dataset from the laboratory characterization of re-compacted samples from Old Dalby	50
5.6	Linear fit for $S < 0.4$	51

5.7	Evaluation of σ_{sat}	51
5.8	Moisture-saturation scatterplot.	52
5.9	Waxman-Smits model	53
6.1	Number of data per day and per selected subset, line 1 to 5 from top to bottom . . .	55
6.2	Outliers in line 1	56
6.3	Negative data in line 2	57
6.4	Resistance versus time (respectively line 1 to 5 from the top to the bottom)	59
6.5	Relative error versus time	60
6.6	Comparison between rainfall, evapotranspiration and infiltration data	61
6.7	Comparison between cumulative infiltration data and in-situ 5TE moisture sensors .	61
6.8	Effect of temperature correction on resistivity data	63
6.9	Temperature model of the Old Dalby subsoil	64
6.10	Comparison between the 5TE moisture content measurements and the effective infiltration calculated from the weather monitoring	65
6.11	Comparison between the 5TE moisture content measurements and the effective infiltration calculated from the weather monitoring	65
6.12	Comparison between the 5TE moisture content measurements and the effective infiltration calculated from the weather monitoring	66
6.13	Water content–resistivity relationship (from Hen-Jones et al., 2017)	67
6.14	Comparison between the conductivity and the moisture measurement of the 5TE. Moisture and conductivity are evaluated with independent measurement methods. .	68
6.15	Comparison between the conductivity and the moisture measurement of the 5TE. Moisture and conductivity are evaluated with independent measurement methods. .	69
6.16	Comparison between the conductivity and the moisture measurement of the 5TE. Moisture and conductivity are evaluated with independent measurement methods. .	70
6.17	Error on the resistivity measurement. For each sensor the 1st, the 5th, the 50th, the 95th and the 99th percentile of the resistivity measurement is shown.	71
6.18	Minimum resistivity observed for each cells (expressed in $\Omega.m$). The minimum observed resistivity is supposed to be close to the saturated resistivity	72
6.19	Waxman-Smits on resistivity ratio	73
6.20	Effect of 2 different physical models and 2 different fitting methods. Here the models are fitted on the points in black ($S>0.18$), for detailed results see TABLE. 6.4	74
6.21	Comparison between 2 different physical models and 2 different fitting methods. Here the models are fitted on all the points, for results see FIG. 6.5	75
6.22	Standard deviation model based on the laboratory measurements	77
6.23	Comparison between weighted data fitting and unweighted data fitting on the laboratory measurements	77
7.1	In black laboratory data, in blue Old Dalby cluster, in red, slip cluster, in green woods cluster. In solid (resp. dashed) line 99th (resp. 1st) percentile of the corresponding saturation (left) or VMC (right) range.	79
7.2	Sensors selected for fitting the Waxman-Smits model. The plotted values corresponds to the median resistivity (resp. resistivity ratio) measured in a given range of VMC (resp. saturation).	80
7.3	Top figure: Fitting of 5 modified Waxman-Smits model on the selected resistivity dataset. Lower figures: Comparison of the error of the fitted models with the error of the dataset	82
7.4	Resistivity (without temperature correction) of the first ERT. Values are expressed in $\Omega.m$	84

7.5	Comparison between the cumulative infiltration measured at the weather station and the mean ERT-derived saturation calculated for the top 3 meters of Line 2	84
7.6	ERT-derived Saturation (subplot 1) and resistivity (subplot 2) mean values calculated for the first three meters of each lines.	85
7.7	ERT derived saturation imaging of the subsoil	86
7.8	ERT-derived Saturation (subplot 1) and resistivity (subplot 2) mean values calculated for the first three meters of each lines.	87
7.9	Effect of resistivity ratio error on saturation evaluation	87
7.10	Water retention curve established from laboratory testing of compacted material drilled on site	88
7.11	Effect of resistivity ratio error on suction evaluation	88
7.12	ERT-derived suction imaging of the subsoil	89
8.1	Effect of data normalization on the resistivity-moisture data	91

3.1	5TE measurement specifications (from Decagon Inc. (2015))	22
4.1	Drift of the non contact measurement device during measurements	39
5.1	Plastic limit (in GMC)	47
5.2	Plastic limit, liquid limit and plasticity index (in GMC)	47
5.3	Proportion of gravel, sand, silt and clay	48
5.4	Parameters estimated to establish the Waxman-Smits model for Old Dalby site	52
6.1	Characteristics of "Woods" and "Slip" 5TE clusters	62
6.2	Parameters fitted for the temperature model	63
6.3	Minimum and maximum values of the calculated saturation resistivity	72
6.4	Results of the different fit of FIG. 6.20	74
6.5	Results of the different fit of FIG. 6.21	76
6.6	Results from the different fits of FIG. 6.23	78
7.1	Comparison between different non-linear fitting methods	82

Chapter 1

Introduction

1.1 Landslide issues

Every year, landslides produce important societal and economic impacts in the world. 7200 events have been recorded worldwide between 2007 and 2015, causing more than 26,000 fatalities and more than \$ 1.8 billion direct economic impacts (Kirschbaum et al., 2015; Uhlemann et al., 2016). In the UK, 759 landslides were recorded during the same period (Pennington et al., 2015). Half of which occurred in the 2012-2013 period due to an exceptionally wet year (Belcher et al., 2014; Uhlemann et al., 2016). Hence, water has an important role in landslide triggering and soil moisture imaging would enhance a better understanding of landslides (Uhlemann et al., 2016). The UK's recorded landslides are principally located in clays and tills: amongst 8835 inland landslides recorded by the Department of the environment (1994), 20% of it occurred in glacial tills, making tills the UK's superficial soil in which slope failure is most often reported (Trenter, 1999).

In the UK, most of the railway network was built 100-200 years ago for the development of the steam railway network. During the 19th century, tipping methods were common building practices and have left an ageing heritage of highly fissured, weak and heterogeneous structures (Chambers et al., 2014). These structures are still widely used today but are likely to fail under repeated climatic stresses (Perry et al., 2003): progressive geotechnical changes driven by seasonal wetting and drying, in addition to moisture content and pore-pressure variations can significantly reduce subsoil's strength (Uhlemann et al., 2016).

UK's railway earthworks often meet those particular conditions (repeated climatic stress, presence of slope, clay material) and their failure can cause important damages, including loss of serviceability, human casualties and reconstruction costs (Chambers et al., 2014). Hence, their monitoring is primordial in order to properly assess, mitigate and remediate their possible failure.

1.2 The role of geophysical methods

Landslides structures have been frequently studied through geophysical surveys (Jongmans and Garambois, 2007). However, studies aiming to understand the actual geotechnical processes causing failure are still scarce (Perrone et al., 2014; Uhlemann et al., 2016). Mitigating landslide issues relies on understanding its causes. Though essential for calibration and validation of the geophysical data, drilling data provides a sparse coverage that does not allow to point out the heterogeneities of the subsoil (Hermans, 2010).

Subsoil heterogeneities are commonly associated to lithological variations, but can also be linked to changes in both water saturation and subsoil alteration. In porous media, moisture content is directly linked to electrical resistivity. Thus, geophysical methods provide a useful tool for the characterization of unstable slopes heterogeneities. Especially when considering that electrical resis-

tivity imaging can image both lithological and moisture contrasts. Jackson et al. (2002) successfully monitored soil moisture in a road embankment in Kenya prior to slope failure, demonstrating the efficiency of the method. Using 2D resistivity imaging they monitored the changes in the soil moisture distribution after the construction of a roadway and were able to identify a rise in the moisture content in the toe of the embankment prior to slope failure event.

Maintenance works along railway lines can be extremely expensive when they suspend the rail traffic. Geophysical studies are non invasive and, apart from the installation, they do not have any impact on the railway network. Moreover, monitoring campaign result in time-space imaging, leading to real-time subsoil characterization. Thus geophysical studies are particularly convenient to assess slope instability and in case of failure the comprehension of the subsoil dynamic ensures the most cost-effective remediation strategies (USGS, 2017).

1.3 The Old Dalby case study

The Old Dalby study site provides a new approach on 4D electrical resistivity tomography. The site is affected by a relict landslide in a railway cutting along an operating railway line. The study aims to provide a reliable way of monitoring the subsoil water saturation in order to prevent damages triggered by a reactivation of the landslide. The site has been instrumented by the BGS PRIME system, which monitor on a daily basis the resistivity of the subsoil along a multi-electrode array and transmit it to a data server in real time. 5 resistivity profiles have been instrumented at the Old Dalby site, providing 4D data that will help understanding short and long term dynamics of the subsoil water movements. The saturation imaging is obtained by combination of in-situ resistivity measurements, data processing and laboratory data characterization. The different steps of the study are shown at FIG. 1.1.

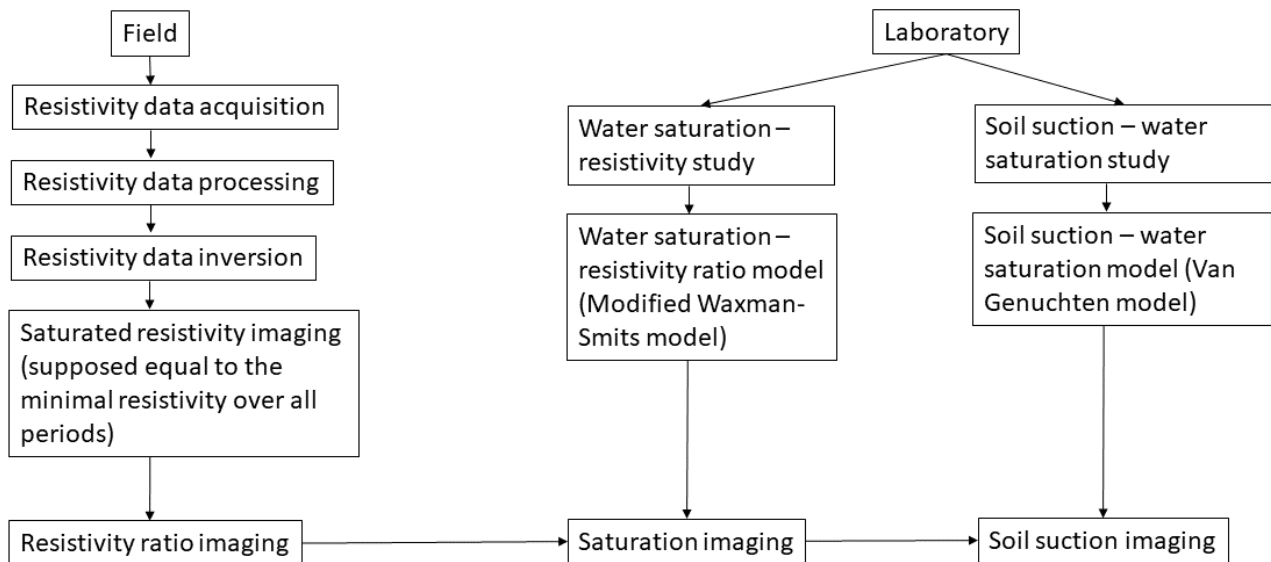


Figure 1.1: Overview of the data processing from the laboratory and field data acquisition to the saturation and soil suction imaging

This study of the Old Dalby site provided a complete characterization of a railway earthwork, from the subsoil characterization to the comprehension of the subsoil moisture dynamic. It includes local subsoil characterization based on drill cores and laboratory characterization of both resistivity and suction response to varying moisture content. Laboratory results were used to develop a model of the resistivity-moisture curve (Waxman-Smits model) and of the suction-moisture curve (van

Genuchten model). Electrical tomography monitoring was used to image the subsoil resistivity on a daily basis and the laboratory models were implemented to image the saturation and the suction variations of the subsoil over a period extending from October 2015 to February 2017 (FIG. 1.2). Results were compared to in-situ moisture and resistivity measurements obtained from buried 5TE probes (FIG. 1.3).

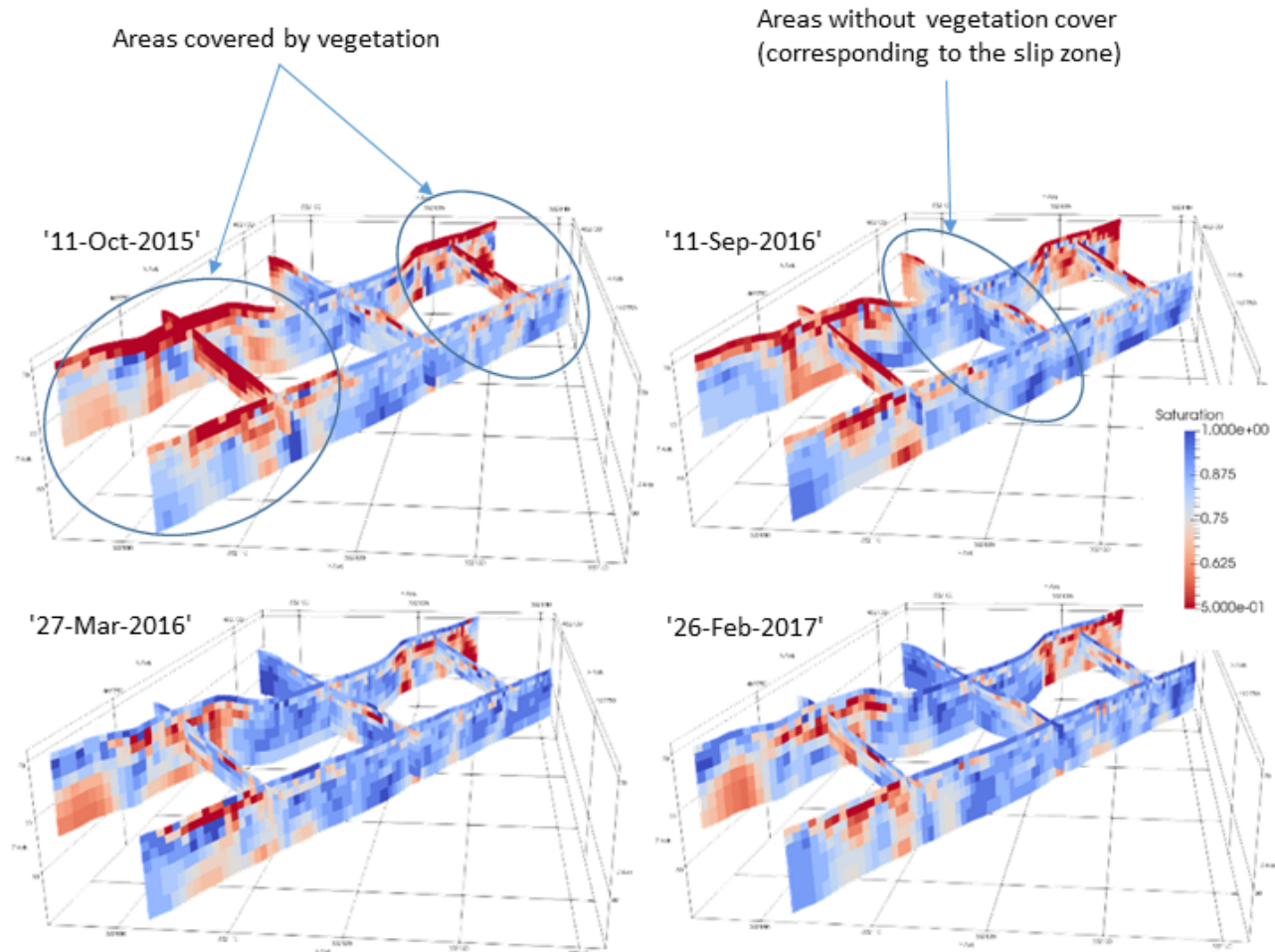


Figure 1.2: ERT-derived saturation imaging of the Old Dalby relict landslide

We showed that the moisture content was mainly varying in the top three meters of the subsoil and that at higher depth the ground was keeping moisture values close to saturation (FIG. 1.2). Also it was shown that the vegetation cover had a significant impact on the moisture dynamic: the area where vegetation is present shows low saturation values (lower than 50% in some areas) in autumn whereas the area of the landslide which has no vegetation at the surface stays nearly saturated all along the year (FIG. 1.2).

The data monitored at the weather station (temperature, precipitations) was used to calculate the cumulative water infiltration (FIG. 1.3). By comparing this information with the results from the saturation imaging we showed that, in the first meters of the subsoil, the saturation dynamic was highly correlated to the water infiltration. Also, we showed that the subsoil saturation imaging was consistent with both short-term and long-term water infiltration. Indeed, sharp saturation increases were observed after important episodes of precipitation and gradual saturation increase were observed due to the progressive accumulation of water in the subsoil (FIG. 1.3).

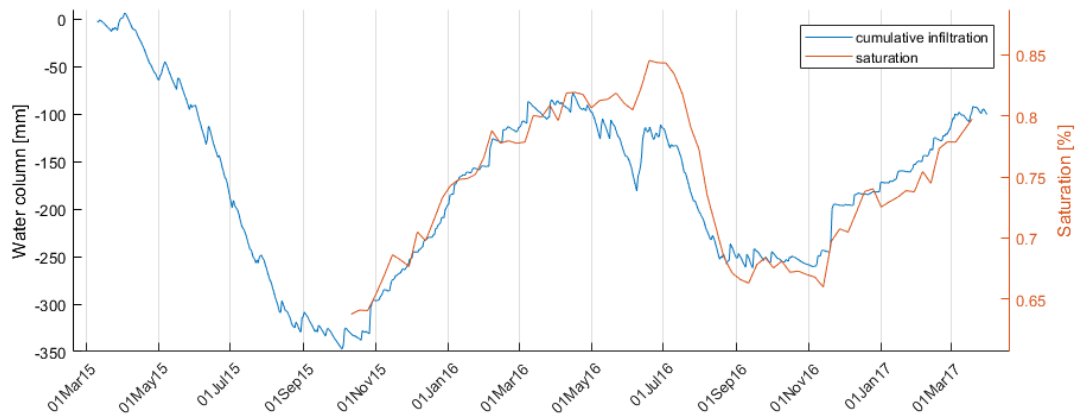


Figure 1.3: Comparison between the cumulative infiltration measured at the weather station and the mean ERT-derived saturation from the top 3 meters of Line 2

Chapter 2

Geology of East Midlands

The Old Dalby landslide study site is located on deposits from the Triassic, which mainly consists of mudstones. Those mudstones are covered by quaternary tills deposited during the last glaciations. The following section details more precisely the context in which the mudstone and the tills were deposited and describe the folding context of the area.

2.1 Global setting

During the late Carboniferous Period all the continental masses moved together to form the supercontinent of Pangea (Hobbs et al., 2002). At the start of the Permian, the tensional stresses within the Pangea resulted in the opening of a large infra-continental basin which led to the formation of the Atlantic Ocean. This basin was located at a latitude of 15-20° north of the equator, corresponding to the current position of the Sahara Desert (Fig. 2.2).

2.1.1 Triassic deposits

Following Warrington and Ivimey-Cook (1992), the climate of the basin during the Triassic was interpreted as being of a monsoonal nature. The encounter between the prevailing north-east winds and the Variscan mountains resulted in high rainfall events which led to periodic floods. The sediments of the Triassic Period in what is now called northern Europe were deposited within this framework. The denomination "Triassic" derives from the threefold lithostratigraphic division, observed in Germany, of Bundsandstein (sandstone), Muschelkalk (carbonate) and Keuper (mudstone). It extends from about 250 Ma to 205 Ma before the present time. Britain being located on the western part of the basin, the Muschelkalk facies is missing and the threefold division is not represented. The Triassic rocks are represented by the Sherwood Sandstone Group (formerly Bunter Sandstone), the Mercia Mudstone Group (formerly Keuper Marl) and the Penarth Group (formerly the Rhaetic) (FIG. 2.1) (Hobbs et al., 2002; Warrington and Ivimey-Cook, 1992).

The lowest division, the Sherwood Sandstone Group, constitutes an unfossiliferous sequence of sandstone, pebbly sandstone and conglomeratic sandstone. It was deposited in a braided stream fluvial environment which lasted for approximately 7 Ma from the beginning of the Triassic Period. Above

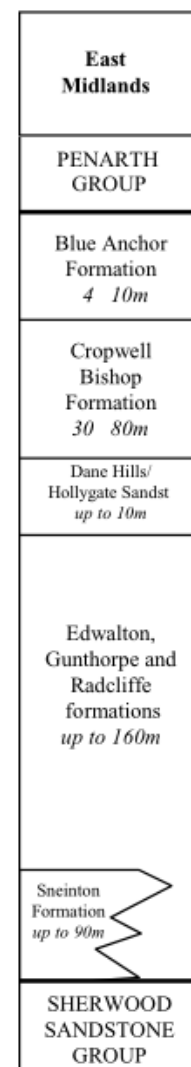


Figure 2.1: Lithostratigraphy of the East Midlands (Hobbs et al., 2002)

this is a 20 Ma complex basinal sequence, bounded by the Hardegsen unconformity (under), the Arden Sandstone (above) and its equivalents. It spans from Scythian to Carnian times. At the beginning of the period, the regional climate became progressively more arid. This led to the development of inland sabkhas, saline mudflats and temporary lakes which slowly replaced the fluvial environment of the Sherwood Sandstone Group. The Arden Sandstone is due to a brief episode (a few Ma) of deltaic or estuarine environment in which grey-green siltstone, mudstone and thick sandstone beds were deposited. The Mercia Mudstone Group follows the Arden Sandstone. It laid down during a 12 Ma period lasting from the end of the Carnian to the Rhaetian times. The Mercia Mudstone Group is described as basinal argillaceous evaporite bearing deposits. It includes both subaqueous and subaerial deposits. Only sulphates are present in the evaporite sequences because they result from the deposition of interstitial brines or shallow water, hyper-saline sabkha environments. At the end of the Triassic (Rhaetian times) starts a widespread marine transgression which marks the unconformity between the Mercia Mudstone Group and the Penarth Group. The base of the Penarth Group, the Westbury Formation, was deposited when the rising sea level flooded the mudflats. This episode laid down a widespread dark grey to black marine mudstone. The Westbury Formation is followed by mudstone and thin limestone beds of the Upper Penarth and Lias Groups (FIG. 2.3) (Hobbs et al., 2002).

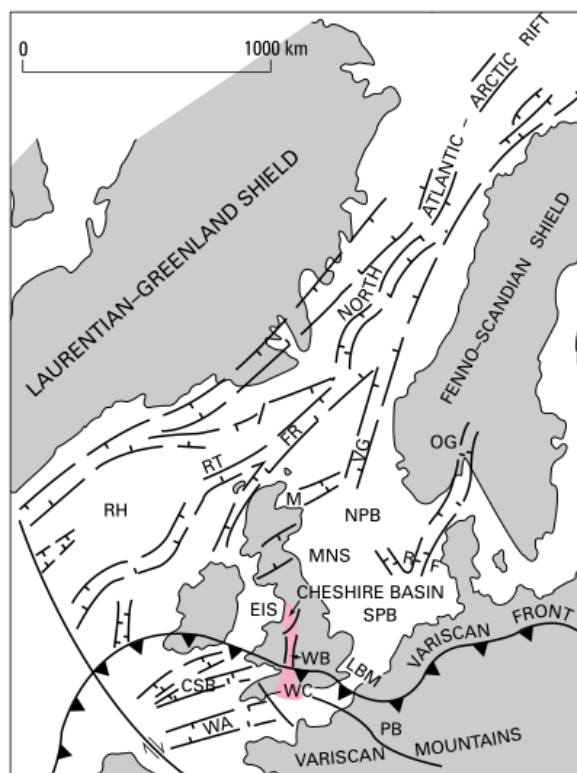


Figure 2.2: Permo-Triassic regional tectonic framework of the North Atlantic region, after Warrington and Ivimey-Cook (1992) & Hobbs et al. (2002)

2.1.2 Mudstone deposition

The Mercia Mudstone Group laid down in a mudflat environment following three processes:

1. accumulation of mud and silt in temporary lakes,
2. rapid settling-out of sheets of silt and fine sands by flash floods,

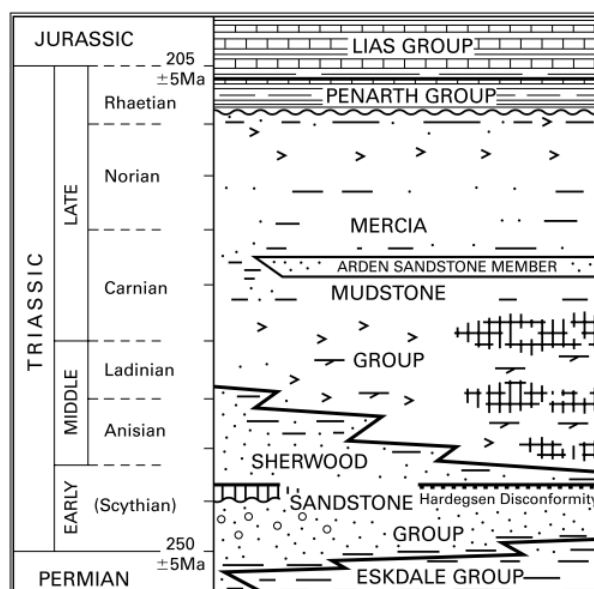


Figure 2.3: Triassic lithofacies in England and the Southern North Sea, after Warrington and Ivimey-Cook (1992) & Hobbs et al. (2002)

3. deposition of eolian dust on the wet mudflat surface.

The group comprises mainly red and, in a smaller proportion, green and grey mudstones and siltstones. The presence of substantial halite layers has been observed in the thicker basinal successions of Somerset, Worcestershire, Staffordshire and Cheshire. Sulphate deposits and sandstone beds are frequently observed at some stratigraphical levels. Large parts of the outcrop of the Mercia Mudstone are covered by Quaternary glacial tills (Hobbs et al., 2002).

2.1.3 Folding and faulting

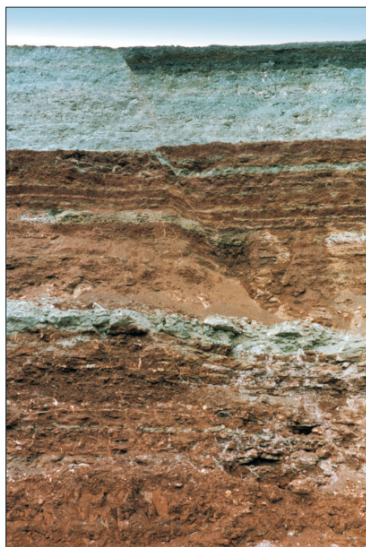


Figure 2.4: Minor fault in the Cropwell Bishop and Blue Anchor formations. Westbury Formation is exposed at the top right section. Cropwell Bishop, Nottinghamshire (after Hobbs et al., 2002)

The tectonic deformation too which the Mercia Mudstone Group has been subjected to is limited. The observed dips are generally less than five degrees, except in the vicinity of faults. Numerous small faults have been observed in the Nottingham and Worcester districts (fig. 2.4). Even if most of the faults have throws of less than 5 m, the displacement is generally sufficient to isolate blocks of minor aquifers formed between the succession of thin beds of dolomitic siltstone and sandstone of the Mercia Mudstone Group.

2.2 Quaternary

The Early and Middle Pleistocene, that extended from 2.6 to 0.125 Ma, was a period of major climate and earth system change driven by a progressive trend of global cooling (Lee et al., 2011).

Great Britain is located off the coast of continental Europe what makes it unique in its geographical setting. Great Britain was bathed by the North Atlantic Drift during interglacial periods, which ensured predominant cool, temperate maritime climates. This setting provided a sharp contrast to those during the glacial periods, where arctic-type conditions were predominant in the British Isles. During glacial periods, the appearance of cold winters lead to the development of sea-ice, periglacial conditions on land and build-up of glacial ice in mountain regions when the amount of precipitation was sufficient. The lowering of global sea level during glacial periods lead to the linking of British Isles to the Continent (Gibbard and Clark, 2011).

Due to the sharp contrast between the glacial and interglacial conditions, the geological record bears the imprint of the combined effects of these changes, providing a fundamental element to differentiate the multiple glaciation events in the stratigraphical subdivision. Evidence for glaciation, identified by tills and glaciofluvial sediments, is found over most of Britain. They are essentially lithological and the glacial limits are determined through the extent of these deposits. Moreover, the extent of ice masses in younger glaciations could be determined by geomorphological evidence, such as moraine ridges and ice-contact landforms (Gibbard and Clark, 2011).

2.2.1 Tills deposition

In lowland south and eastern Britain, depositional sequences tend to be represented by relatively subdued landforms. The sediments and associated features recorded the evidence of both glacial expansion and retreat of at least three glaciation episodes (Anglian, Wolstonian and Devensian, FIG. 2.5). The area south of the Thames remained unglaciated throughout the Pleistocene, but has been influenced by meltwater activity (Gibbard and Clark, 2011).

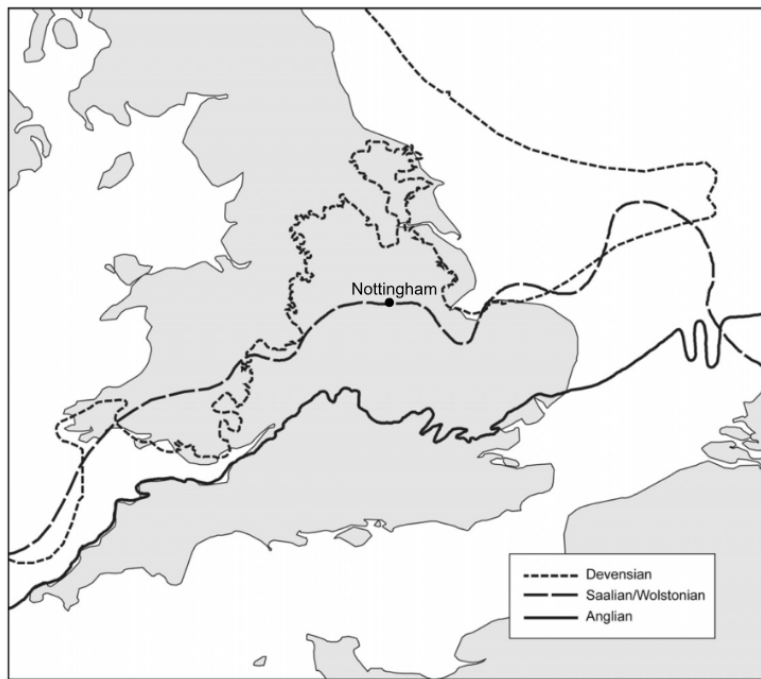


Figure 2.5: Extent of the last glaciations in Great Britain (after Gibbard and Clark (2011))

Chapter 3

Theory

3.1 Core Characterization

3.1.1 Non contact resistivity

Non-contacting resistivity imaging is a non-destructive method for continuous core logging. It can image the resistivity of an entire core without removing its liners. This leads to a spatially complete dataset that completes the extremely sparse and incomplete datasets from present practice of core-plugs subsampling (Jackson et al., 1997).

The principle of the measurement is based on induced current. A transmitter coil produces a primary magnetic field that induces electric currents in the core. These currents generate a secondary magnetic field inversely proportional to the resistivity of the core. As the secondary field is typically 10⁷ smaller than the primary field, the primary field must be removed from the secondary field and the residual field amplified in order to get an accurate measure. At low frequencies, the transmitter and the receiver signals have a 90° phase shift (Jackson et al., 1997).

To make the measurements, the core to image is placed on a table under which the non-contacting device has been placed. The device is located under the table so the core can be slide over it. The measuring instrument used was developed at the BGS. It is highly sensitive and needs several hours to warm-up and stabilize before starting the measurements. A voltmeter was used to increase the precision of the measurements (Fig. 3.1) .

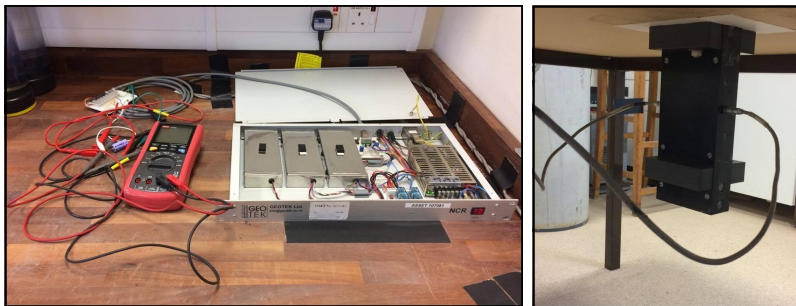


Figure 3.1: Non contact resistivity measurement assembly

The measurements depend on the resistivity of the core. To obtain a law that links our measurements to the resistivity of the core, we measure the current induced in cores of known resistivity and same geometrical characteristics. For this purpose, we use cores filled with an NaCl solution of equivalent 1, 10 and 30 $\Omega\cdot\text{m}$ resistivity, at 25°C (Fig. 3.2). The cores used for the calibration are 31 cm long and have the same diameter than the studied cores. The results of the calibration are shown in Fig. 3.3. The calibration cores need to be sufficiently long to avoid measurement effects at

each end. In our case, the results are stable between 10 and 21 cm from each end of the core, so the condition is satisfied.

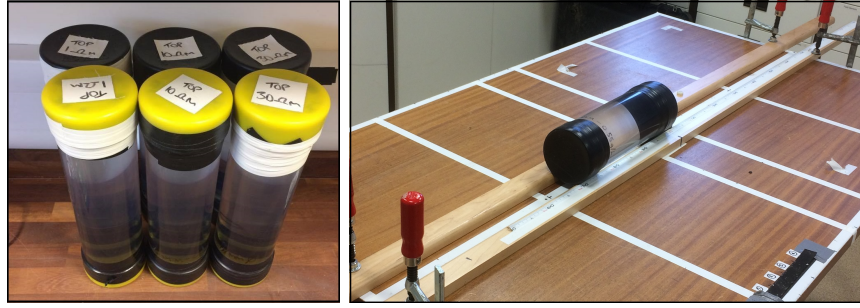


Figure 3.2: NaCl cores used to calibrate the non contact resistivity device

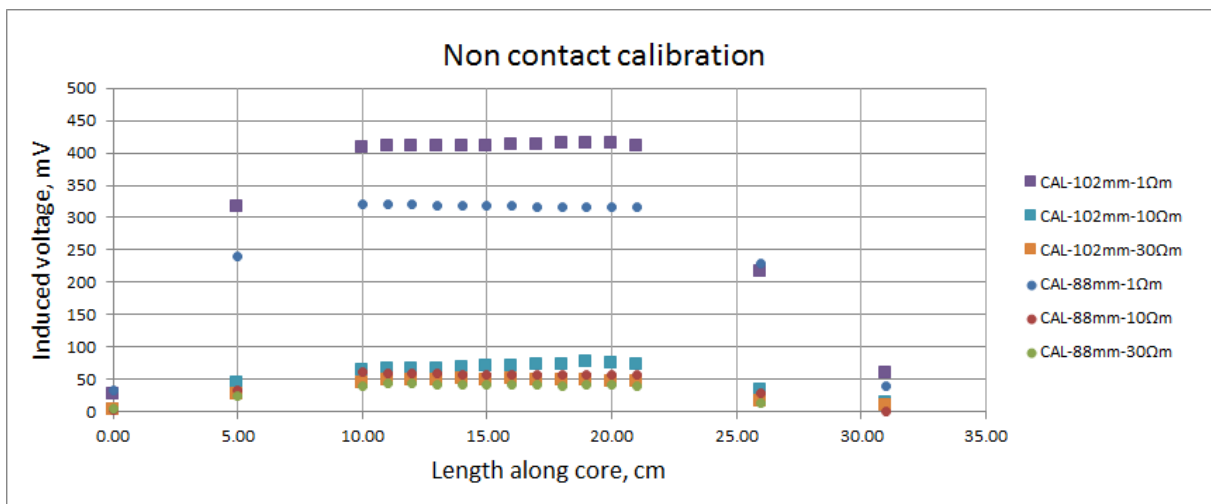


Figure 3.3: Calibration of the non-contact resistivity measurements

To convert the output values of the instrument (in mV) in term of resistivity, we record the mean stabilized output value of the calibration cores. A power fit law is then applied to interpolate the resistivity values from the values return from the non-contacting device (FIG. 3.4).

3.1.2 Galvanic

The electrical resistivity, ρ , of the core was measured by injecting a galvanic current, I , at its extremities. The measurements electrodes are then moved along the core with a constant spacing to calculate the resistivity. The measurements were done with an ABEM TERRAMETER SAS 300C (FIG. 3.5) which allows to calculate directly the resistance, R , of the core. Knowing the inner radius, r , of the core and the spacing, L , between the measurements electrodes, the resistivity of the core can be expressed as following:

$$\rho = \frac{R.A}{L} = \frac{R.\pi.r^2}{L} \quad (3.1.1)$$

The measurements were performed by pre-drilling the core plastic seal and introducing copper wires inside the core. Each measurement was done using 4 stacks.

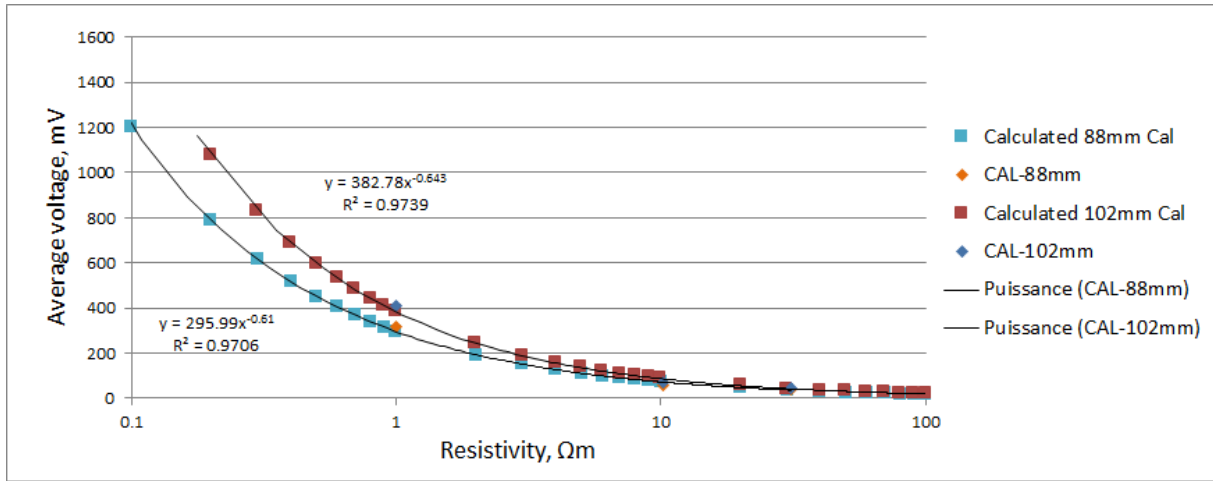


Figure 3.4: Power fit law used to convert non contact resistivity measurements into resistivity



Figure 3.5: ABEM Terrameter SAS 300C (left) and 5TE probe (right)

3.1.3 5TE

In addition to the galvanic and non contact measurements, a 5TE probe (FIG. 3.5) was used. Because the 5TE probe is very fragile, a specific tool was used to create a pilot-hole before each measurements (FIG. 3.5). The 5TE probe was tested on the core because it has the advantage of measuring the resistivity and the volumetric moisture content simultaneously and also because similar probes were installed at Old Dalby site. From the volumetric moisture content, Θ , we can easily retrieve the gravimetric moisture content, w :

$$w = \frac{m_w}{m_{dry}} = \frac{V_w}{V_{dry}} \frac{d_w}{d_{dry}} = \Theta \cdot \frac{d_w}{d_{dry}} \quad (3.1.2)$$

with m_w the mass of fluid contained in the pores, m_{dry} the mass of the dry soil sample, d_{dry} the dry density of the material and d_w the density of the fluid contained in the pores.

The measurement specification of the 5TE are shown at TABLE 3.1. The volumetric moisture content is determined by the 5TE sensor by measuring the dielectric constant of the media using capacitance/frequency domain technology. The salinity and textural effects are minimized by the sensor using a 70 MHz frequency, which makes the 5TE sensor accurate for most soils. The dielectric constant of the media is converted in volumetric water content for mineral soils using the Topp equation (Topp et al., 1980):

$$\Theta = -5.3 \cdot 10^{-2} + 2.92 \cdot 10^{-2} \cdot \epsilon_r - 5.5 \cdot 10^{-4} \cdot \epsilon_r^2 + 4.3 \cdot 10^{-6} \cdot \epsilon_r^3 \quad (3.1.3)$$

with Θ [m^3/m^3] the volumetric moisture content and $\epsilon_r = \epsilon/\epsilon_0$ [-] the dielectric constant, where ϵ_0 is the permittivity of free space. This relation is empirical and has been showed to be independent of texture, salinity, temperature and soil density.

	Volumetric Water Content	Temperature	Electrical Conductivity
Accuracy	Generic calibration equation: $\pm 0.03 \text{ m}^3/\text{m}^3$ ($\pm 3\%$ VWC) typ Medium Specific Calibration: \pm $0.02 \text{ m}^3/\text{m}^3$ ($\pm 2\%$ VWC)	$\pm 1^\circ\text{C}$	$\pm 10\%$ from 0 to 7 dS/m, user calibration required from 7 to 23 dS/m
Resolution	$0.0008 \text{ m}^3/\text{m}^3$ (0.08% VWC) from 0 - 50% VWC	0.1°C	0.01 dS/m from 0 to 7 dS/m, 0.05 dS/m from 7 to 23 dS/m
Range	0 - $1 \text{ m}^3/\text{m}^3$ (0 - 100% VWC)	- 40°C to + 50°C	0-23 dS/m

Table 3.1: 5TE measurement specifications (from Decagon Inc. (2015))

The temperature is measured with an onboard thermistor, and the electrical conductivity with stainless steel electrode array. The temperature effect on conductivity value is directly corrected by the probe using the temperature correction proposed by the US Salinity labs Handbook 60 (Decagon Inc., 2015; METER Group, 2017). Hence the subsoil conductivity and the VMC are measured through independent measurements.

3.2 Atterberg limits

The Atterberg limits, comprising the shrinkage limit (SL), the plastic limit (PL) and the liquid limit (LL), are a measure of the critical water contents of a fine-grained soil (Sowers, 1979). In our case, only the plastic and the liquid limits were evaluated. The Atterberg limits are performed on material smaller than $425 \mu\text{m}$ passing. Thus, the material requires the following preparation prior to the tests:

- dried in the 40°C oven,



Figure 3.6: Cone penetrometer used to evaluate liquid limit

- stirred into slurry,
- sieved at 425 μm passing,
- dried in the 40°C oven.

The 40°C oven is used to avoid any changes in the mineralogy of the clays.

3.2.1 Liquid limit

The liquid limit has been evaluated using the cone penetrometer method in compliance with British Standard BS1377:Part 2:1990:4.3.

3.2.1.1 Material

The liquid limit requires a cone penetrometer (Fig. 3.6) complying with requirements of BS200:Part 49, a flat glass plate (500 mm square and 10 mm thick), some metal cups (55 mm diameter and 40 mm deep), distilled water, palette knives and small containers to evaluate the moisture content.

3.2.1.2 Procedure

The liquid limit is evaluated as following (Head and Epps, 1992):

1. Select about 300 g of the prepared soil paste and place it on the glass plate. If the plastic limit is also to be done, place a small portion of sample in a small bag before adding to much water.
2. Check the cone penetrometer apparatus. It must comply with clauses 4.3.2.3 and 4.3.2.4 of BS1377:Part 2:1990. The most important points to check are the weight of the cone and the sharpness of the cone point.

3. Repeat the following procedure until you have 4 moisture content samples with a cone penetration ranging between 15 and 25 mm:
 - (a) Mix and work the soil paste on the glass plate with the spatula. Add distilled water so the first measurement give a cone penetration of about 15 mm.
 - (b) Place the soil in the cup.
 - (c) Adjust the cone near the upper end of the filled cup and reset the dial gauge.
 - (d) Drop the cone into the sample and hold the pressed position for 5 s.
 - (e) Measure cone penetration.
 - (f) Repeat penetration.
 - (g) Take a moisture content sample.
 - (h) Add distilled water.
4. Calculate and plot graph.
5. Report result.

To make any results admissible, the difference between the second and the first measurement must be of less than 0.5 mm. The average value is then recorded. If the second penetration is between 0.5 and 1 mm different from the first, a third measurement is realised and the average value is recorded if the overall difference in penetration does not exceed 1 mm. If it is not the case, the soil is removed from the cup and the procedure is repeated from stage 3.

3.2.2 Plastic limit

The plastic limit is evaluated in compliance with standards BS1377:Part 2:1990:5.3 and ASTM D4318.

3.2.2.1 Material

The hand of the operator is the most important piece of apparatus for this test, it should be clean and free from grease. Use the same glass plate and tools required for the liquid limit test. You will also need a separate glass plate for rolling of threads, a short length (≈ 100 mm) of 3 mm diameter metal rod and some containers to measure moisture content.

3.2.2.2 Procedure

The procedure of the stages has been described by Head and Epps (1992):

1. Take the soil samples you kept aside before performing the liquid limit test.
2. Take 20 g of sample and roll it into ball between the palms of the hands so it gets dryer. When slight cracks appear, divide the ball into two portions each of about 10 g. Further divide each portion into four equal parts.
3. Take one of the part and start with a 6 mm thread and roll it between the fingers of one hand and the surface of the glass plate. Repeat this until the thread crumbles when it has been rolled to 3 mm. The 3 mm metal rod serves as a reference.
4. Place the crumbled threads in the moisture container.

5. Repeat tests on the other three pieces of soil and place the crumbled threads in the same container. Repeat the same procedure on the second set of four equal parts but place the crumbled threads in a second container.
6. Calculate and report results, if the two results differ by more than 0.5% moisture content, the test should be repeated.

The results of the tests are expressed in terms of gravimetric moisture content (GMC), which means that we consider the mass of the samples in our calculations. The gravimetric moisture content, w , equivalent to each limit is calculated as following:

$$w = \frac{m_w - m_{dry}}{m_{dry}}$$

3.2.3 Plasticity index

The plasticity index (PI) is an evaluation of the plasticity of a soil. It measures the size of the range of water contents between which the soil exhibits plastic properties. It is defined as the difference between the liquid limit and the plastic limit ($PI = LL - PL$). A high PI is representative of clay, a low to moderate value is representative of silt and a value close to 0 (non-plastic) is representative of soils with little or no silt or clay (En.wikipedia.org, 2017).

Based on the PI, we have the following classification (Sowers, 1979; En.wikipedia.org, 2017):

- 0 : Non plastic
- <7 : Slightly plastic
- 7-17 : Medium plastic
- >17 : Highly plastic

3.3 Particle size analysis

3.3.1 Procedure

The particle size analysis (PSA) requires two samples of soils because the grain size range $< 63 \mu\text{m}$ and the grain size range $> 63 \mu\text{m}$ are analysed separately. The two samples are prepared as following:

- $< 63 \mu\text{m}$ We take a sample of about 50 g to which we add calgon to avoid flocculation. The sample is fixed to an automatic shaker for about 12 hours and is then sieved at $63 \mu\text{m}$. The undersize is collected wet and dried at 105°C before being analysed by the sedigraph. No weighting is required for the sedigraph.
- $> 63 \mu\text{m}$ We take a sample of about 300 g and put it in the 105°C oven to obtain its dry weight. We then sieve the sample at $63 \mu\text{m}$, collect the oversize and put it in the 105°C oven. The remaining material is then analysed by a common sieve analysis.

3.4 Compacted samples preparation

3.4.1 Generalities

A lot of civil engineering projects needs to use soils as "fill" material, which generally needs to be compacted to a dense state, in order to obtain satisfactory engineering properties. Thus, control of the degree of compaction is necessary to obtain satisfactory results at a reasonable cost (Head and Epps, 1992). The compaction test gives the following properties of the soils (Head and Epps, 1992):

1. The relationship between dry density and moisture content for a given degree of compactive effort
2. The optimum moisture content (OMC), which is described as the moisture content of a soil at which a given compactive effort will produce the maximum dry density
3. The maximum dry density, which is the dry density obtained at the OMC for a given compactive effort.

In our case the compaction test procedure was used to produce reproducible soil samples with properties similar to the in-situ undisturbed material. The optimal moisture content is assumed to be close to the plastic limit.

3.4.2 Samples preparation

The samples were prepared following the standard 'light' proctor compaction test (BS1377:Part 4:1990:3.3) assuming the optimum moisture content (OMC) was close to their plastic limit. Given the results from the Atterberg limits, the compaction was performed around 19% GMC. The proctor hammer and the compaction mould have the following properties

1. Weight of the hammer (rammer weight): 2.5Kg
2. Diameter of the hammer: 50mm
3. Drop: 300mm
4. Dimension of the compaction mould: $\Phi 101.2 \text{ mm} \times 116.3 \text{ mm}$
5. Finish: corrosion resistant

The compaction mould is filled with the clay material in three steps to ensure that the compaction is well spread over the entire volume of soil. For each soil layer, 25 hammer blows are released following a circular path along the surface of the material (Markwick, 1945).

3.5 Resistivity-moisture content characterization

3.5.1 Archie's law

The bulk electrical resistivity of porous rocks and sediments varies with the nature of the fluids contained in the pores and their respective degree of saturation. Archie et al. (1942) studied saturated sands within the context of determining petroleum reservoir characteristics. He proposed a relationship linking the resistivity of a water saturated sand with the resistivity of the fluids contained in the pores. The expression is written

$$\rho_0 = F \rho_w \quad (3.5.1)$$

Or

$$\sigma_0 = \sigma_w / F \quad (3.5.2)$$

Where ρ_0 (resp. σ_0) is the resistivity (resp. conductivity) of the sand saturated in brine, ρ_w (resp. σ_w) is the resistivity (resp. conductivity) of the brine, and F is the formation resistivity factor. The formation factor F is related to soil porosity ϕ and can be expressed (Archie et al., 1942)

$$F = a \cdot \phi^{-m} \quad (3.5.3)$$

Where a is a constant and m is the porosity exponent. Further investigations lead to the extension of the relation 3.5.1 to partially saturated sand, for water saturations down to about 0.15-0.2, we have (Archie et al., 1942)

$$\rho_0 = \rho_w F S^{-n} \quad (3.5.4)$$

Or

$$\sigma_0 = \frac{S^n}{F} \sigma_w \quad (3.5.5)$$

Where S is the water saturation and n is an empirical parameter, called saturation exponent, close to 2 for clean unconsolidated and consolidated sand (Archie et al., 1942). Archie's law only takes into account the conductivity of the rock due to the fluid content (Hermans, 2010). This can be a limitation for material in which the matrix resistivity is non negligible, i.e. clayey-sand where the electrical double layer can have a significant effect on the bulk resistivity. To overcome this limitation, Waxman and Smits (1968) developed a simple physical model that relates electrical bulk conductivity of partly saturated shaly sand to the water conductivity and the cation-exchange capacity per unit pore volume of the rock.

3.5.2 Waxman-Smits model

3.5.2.1 Saturated medium

Waxman and Smits (1968) developed a model taking into account the effect of the matrix resistivity. The model developed by Waxman and Smits (1968) consists of two resistance elements in parallel, describing the respective resistivity of the free electrolyte contained in the pore volume of the rock and the contribution of the exchange cations associated with the clay electrical double layer. Thus, we write

$$\sigma_0 = x\sigma_e + y\sigma_w \quad (3.5.6)$$

Where σ_0 is the bulk conductivity, σ_e is the clay exchange cations conductivity, σ_w is the equilibrating salt solution conductivity, and x and y are geometric parameters. The cation-exchange is responsible of a sharp increase in conductivity with increasing concentration of electrolyte in the dilute range (Waxman and Smits, 1968).

Let assume that the electric current transported by the counterions associated with the clay and that the current attributed to the ions in the pore water travels along the same tortuous path. The geometric factor x and y (3.5.6) are equal, and by analogy with the idea of formation resistivity factor (3.5.1) developed by Archie et al., 1942, we can write

$$\sigma_0 = \frac{1}{F}(\sigma_e + \sigma_w) \quad (3.5.7)$$

Where F is the formation resistivity factor. Hence, equation (3.5.7) is consistent with Archie's law, as we find back expression (3.5.1) for $\sigma_e = 0$. Defining the cation concentration per unit pore volume Q_v , and the average mobility of ions B , we can express equation (3.5.7) as

$$\sigma_0 = \frac{1}{F}(BQ_v + \sigma_w) \quad (3.5.8)$$

Where the parameters Q_v and B are respectively equal to

$$Q_v = \frac{(1 - \phi)d_s c}{100\phi} \quad (3.5.9)$$

And

$$B = 4.6 [1 - 0.6 \exp(-\sigma_w/1.3)] \quad (3.5.10)$$

Where ϕ is the soil porosity, d_s is the particle grain density, and c is the cation exchange capacity (meq/100g).

3.5.2.2 Partially saturated medium

When the material is unsaturated, the exchange ions associated with the clay become more concentrated in the remaining pore water (Waxman and Smits, 1968), hence we have

$$\sigma_e = \frac{BQ_v}{S} = \frac{\sigma_{e,sat}}{S} \quad (3.5.11)$$

Where $\sigma_{e,sat}$ is the clay exchange cations conductivity of the saturated soil. From equations (3.5.7) & (3.5.11), and by analogy with Archie's equation (3.5.5), we obtain Waxman-Smits relation, which describe the conductivity of a partially saturated shaly sand

$$\sigma_0 = \frac{S^n}{F} \left(\sigma_w + \frac{BQ_v}{S} \right) \quad (3.5.12)$$

Chambers et al. (2014) proposed a modification of Waxman-Smits equation to incorporate gravimetric moisture content, w , rather than saturation. Saturation S can be expressed as

$$S = \frac{wd_s(1-\phi)}{d_w\phi} \quad (3.5.13)$$

With d_s the particle grain density of the soil sample. Hence, equation (3.5.12) can be expressed as

$$\rho_0 = F \left(\frac{\phi d_w}{(1-\phi)d_s w} \right)^n \left[\frac{1}{\rho_w} + B \left(\frac{cd_w}{100w} \right) \right]^{-1} \quad (3.5.14)$$

This relation is true for $w < w_{sat}$, where w_{sat} is the minimum gravimetric moisture content for which the soil is saturated. Its value is given by (Eq. A.0.14):

$$w_{sat} = \frac{\phi d_w}{(1-\phi)d_s} \quad (3.5.15)$$

Thus, equation (3.5.14) becomes

$$\rho_0 = F \left(\frac{w_{sat}}{w} \right)^n \left[\frac{1}{\rho_w} + B \left(\frac{cd_w}{100w} \right) \right]^{-1} \quad (3.5.16)$$

To limit the number of parameters to determine during the fitting, we can write:

$$\rho_0 = F w_{sat} \left(\frac{w_{sat}}{w} \right)^{n-1} \left(\frac{\rho_w \rho_{e,sat}}{w \rho_{e,sat} + w_{sat} \rho_w} \right) \quad (3.5.17)$$

With $\rho_{e,sat} = 1/\sigma_{e,sat}$ the clay exchange cations resistivity of saturated soil.

3.6 Soil-moisture characteristic curve

3.6.1 Soil Suction

The water pressure measured by a piezometer below the water table is not the only pressure force acting in soils. In an unsaturated environment, even if void spaces are mainly occupied by air, it exists a force holding water between grains. Especially, if soils with equal moisture content but different particle size distribution are placed in contact with each other, water will displace from the coarser grain soil to the finer grain soil, demonstrating the presence of an acting force.

If water moves spontaneously from one soil to another, it means that the finer textured soil has a smaller water potential. We can make the analogy with an object falling spontaneously from a

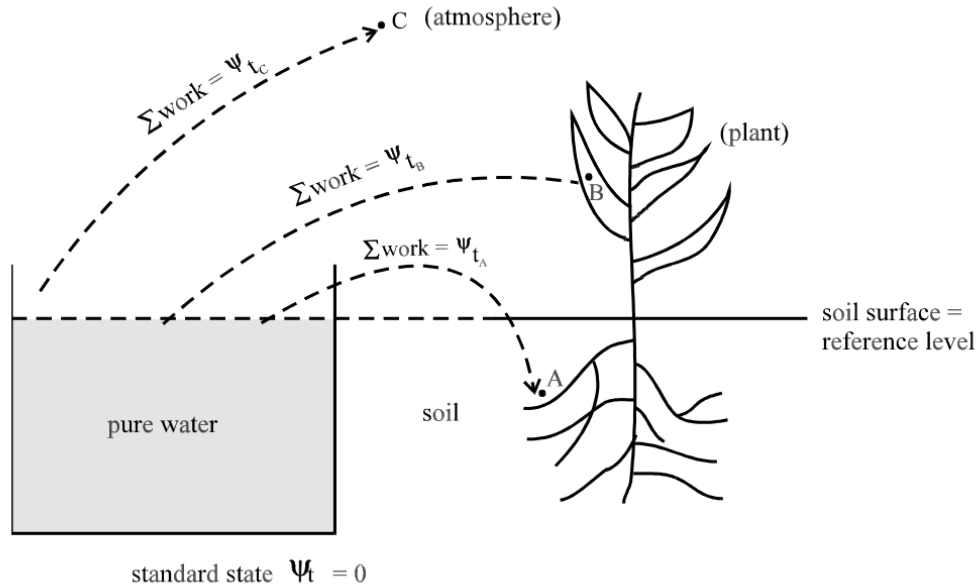


Figure 3.7: Potential of soil water, water in plant cell and water in the atmosphere, from (Hartmann, 2003)

higher to a lower elevation. The soil water potential expresses the specific potential energy (per unit mass) of soil water relative to that of water in a standard reference state. By convention, we assign to free and pure liquid water a water potential equal to zero (Hartmann, 2003).

The total potential of soil water is defined as “*the amount of work that must be done per unit quantity (mass, volume or weight) of pure free water in order to transport reversibly and isothermally an infinitesimal quantity of water from a pool of pure water at a specified elevation at atmospheric pressure (standard reference state) to the soil water at the point under consideration in the soil-plant-atmosphere-system*” (FIG. 3.7, Hartmann (2003)).

Soil suction, P , and total soil water potential, ψ_t , design the same property. In a simplified way, the soil suction can be view as the capacity of an unsaturated soil to keep its water content. This property of soils depends on the texture, on the size of the pores and on the degree of water saturation of the soil. If pure and free liquid water moves spontaneously into the soil, i.e. if work is accomplish by moving into the soil, the potential is negative. Inversely, if some work is required to move water into the soil, the potential is positive.

Soil water is subjected to various force field and each of them must be taken into account to establish the total potential of soil water ψ_t , these force field comprises the gravitational potential ψ_g , the osmotic potential ψ_o , the matrix potential ψ_m and the external gas pressure potential $\psi_{e.p.}$. Other additional terms are theoretically possible. Mathematically, we write:

$$\psi_t = \psi_g + \psi_o + \psi_m + \psi_{e.p.} + \dots \quad (3.6.1)$$

The soil suction is generally expressed as energy per unit volume of water ($\text{J/m}^3 = \text{N/m}^2 = \text{Pa}$) which is equivalent to pressure units. Another common approach is to express it as energy per unit weight of water, which is equivalent to height units ($\text{J/N} = \text{m}$). The logarithm of soil suction expressed in cm is defined as pF:

$$pF = \log_{10} \left(100 \frac{P[\text{N/m}^2]}{\gamma_w[\text{N/m}^3]} \right) \quad (3.6.2)$$

3.6.2 Soil-moisture characteristic curve - Van Genuchten model

The soil-moisture characteristic curve is defined as the relationship between water content and suction. The water content can be calculated per unit of volume (volumetric water content) or per unit of mass (gravimetric water content). Depending on the chosen calculation, a different information on the soil behaviour will be obtained. The shape of the curve is variable and depends on the soil properties and on the way of calculating the water content (volumetric or gravimetric). Suction pressures covers a large range of values, hence the soil-moisture characteristic curve is generally presented on a semi-logarithmic graph.

3.7 Site investigation

3.7.1 Electrical resistivity tomography

The aim of electrical methods is to determine the electrical resistivity of the subsurface. This is generally performed by injecting an electrical current I (order of mA) between a pair of electrodes and measuring the resulting voltage V (order of mV) between a second pair of electrodes. Evaluating the impedance ratio $Z = V/I$, we can easily transform the measurements in terms of apparent electrical resistivity ρ_a ($\Omega.m$), which gives an intuitive indicator of the actual underlying electrical resistivity value.

Different arrangements of the electrodes makes it possible to assess the apparent resistivity ρ_a at different depths and lateral positions. By plotting each measurement to their corresponding depth and lateral position, we obtain an apparent resistivity map called *pseudosection* (Loke, 1999). The inversion of the pseudosection gives a two- or three-dimensional (2-D or 3-D) resistivity section of the subsurface.

The resistivity section must, as far as possible, be interpreted in relation with the local geology (based on outcrops, borehole and supporting geophysical studies), as geological materials can cover a broad range of resistivity values with varying levels of saturation/alteration and different materials can have similar resistivity values. Thus, it is not possible to describe the lithology of the subsoil based on resistivity measurements only, see FIG. 3.8. If some laboratory tests have been performed, the geological interpretation should also incorporate the evaluated properties of the subsoil (Everett, 2013). In the case of this study, it enables to convert the resistivity data in terms of moisture content and soil suction.

3.7.2 Inversion

3.7.2.1 Introduction

The aim of an ERT campaign is to determine the resistivity distribution of the subsoil from the apparent resistivity values collected. Inverse problems are often ill-posed (due to existence, non-uniqueness or instability of the problem), and finding a satisfying mathematical solution itself is not sufficient. The solution has to be physically and geologically plausible (Hermans, 2010). Even if the solution existence is often verified, the noise contained in the data in addition to poor model conditioning can lead to invalid data interpretation. Also the existence of the solution does not mean it is unique. If a model different from zero has a zero image in the data domain, this solution can be added to the true model without any effect on the calculated data. Finally, the solution may be unstable, meaning that a small change in the data can have a significant effect on the calculated model. This is especially problematic when the data contains high amplitudes of noise (Hermans, 2010).

A common approach to regularize an ill-posed problem is to add a smoothness constraint and to consider the amplitude of noise in the inversion algorithm.

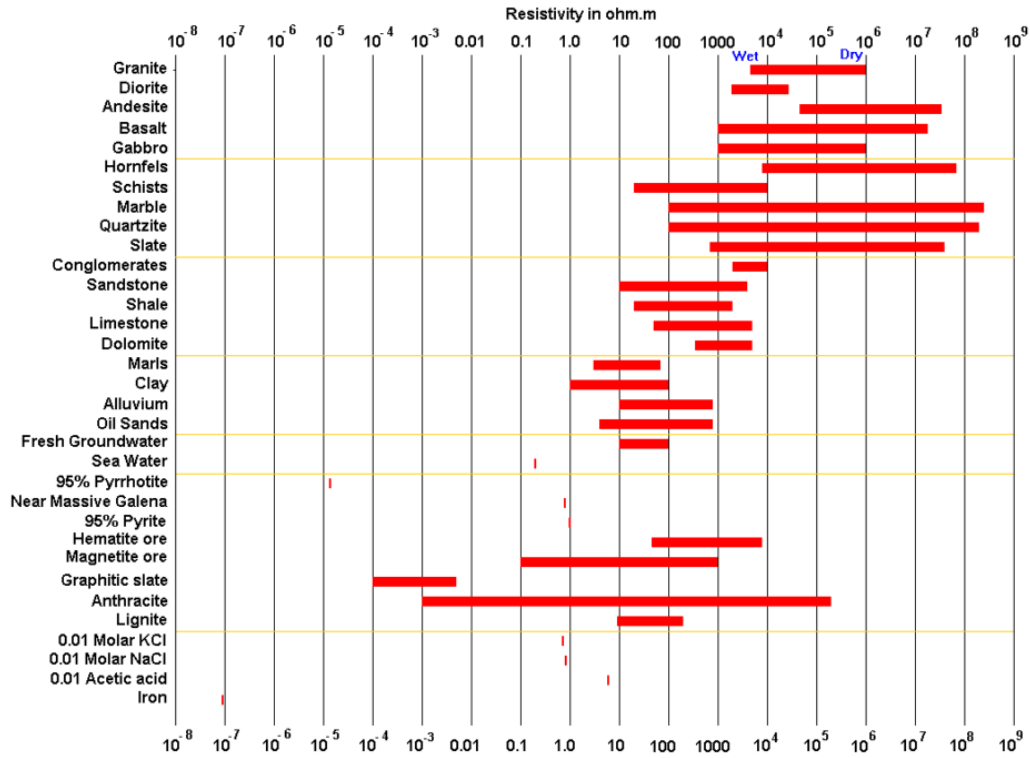


Figure 3.8: Common resistivity of rocks, soils and minerals (Loke, 1999)

3.7.2.2 Forward Problem

Ohm's law governs the relationship between resistivity, current and electrical potential. Combining Ohm's law with the conservation of current, as given by Poisson's equation, it is possible to calculate the electrical potential in a continuous medium (Sharma and Verma, 2015). Thus, the potential due to a point current source located at \vec{x}_s can be expressed as:

$$\nabla \cdot \frac{1}{\rho(\vec{x})} \nabla \phi(\vec{x}) = -I \delta(\vec{x} - \vec{x}_s) \quad (3.7.1)$$

With ρ the resistivity, ϕ the electrical potential and I the point-like injected current. The boundary conditions are written:

$$\alpha(\vec{x}) \frac{\partial \phi(\vec{x})}{\partial \vec{n}} + \beta(\vec{x}) \phi(\vec{x}) = 0 \quad (3.7.2)$$

From these equations, we see that if the resistivity distribution is known, the potential at any point of the surface or within the medium can be calculated. Note that equation (3.7.1) does not take into account the presence of finite electrodes that may influence practical measurements (Rücker, 2010). For simple models, analytical methods are used, but for more complex structures a finite-difference or a finite-element approach is generally preferred to calculate the distribution of the potential (Sharma and Verma, 2015).

The forward problem is a part of the inversion itself as it is carried out after every iteration to evaluate the data misfit between the measured data and the data calculated from the model (Hermans, 2010).

The available data from a resistivity survey are the positions of the electrodes, the current injected I and its resulting potential difference ΔV . For every electrodes configuration, there is an

associated geometrical factor k , which is used to convert the current and voltage measurements into apparent resistivity ρ_a (Sharma and Verma, 2015):

$$\rho_a = k \frac{\Delta V}{I} \quad (3.7.3)$$

This equation, which assumes that the earth is homogeneous for every electrodes configuration, represents the simplest form of the inverse problem (Sharma and Verma, 2015). The type of arrays configurations will have a direct impact on the conditioning of the inversion. Thus, there is a compromise between the array configuration and the resolution of the model (FIG 3.9).

Figure 3.9: Characteristics of different 2D arrays configurations types (from Sharma and Verma, 2015)

		Wenner	Wenner-Schlumberger	Dipole-dipole	Pole-Pole	Pole-dipole
1	Sensitivity of the array horizontal structures	****	**	*	**	**
2	Sensitivity of the array vertical structures	*	**	****	**	*
3	Depth of Investigation	*	**	***	****	***
4	Horizontal Data coverage	*	**	***	****	***
5	Signal Strength	****	***	*	****	**

Here each star represents degree of effectiveness of the method (4 stars being most effective)

3.7.2.3 Inversion algorithm

Problematic Considering a dataset d composed of N measured apparent resistivity, we show previously that if we know the M values of the resistivity model m , then we can calculate the electrical potential at any point of the surface or within the subsurface. Hence, there is a function g that links the M values of the resistivity model to the N values of measured apparent resistivity. This express the *forward problem* of the inversion and can be mathematically written:

$$d = g(m) \quad (3.7.4)$$

If such a relation exists, there might be an inverse function, g^{-1} , that links the model domain to the data domain. Unfortunately, not all functions admit an inverse functions. In order for a function $g : M \rightarrow D$ to admit an inverse, it must have the property that, on the part of the domain considered, for every d in D there must be one, and only one m in M so that $g(m) = d$. This property ensures that a function $g : D \rightarrow M$ will exist having the necessary relationship with g (Aster et al., 2013). Mathematically we would have:

$$m = g^{-1}(d) \quad (3.7.5)$$

In practice, we can only use a finite number of electrodes covering part of the surface, hence the resistivity inversion is an ill-posed problem and the model calculated from the inversion is non unique. Hence, more than one resistivity model will produce solutions consistent with the observed data (Sharma and Verma, 2015).

Newton minimizing algorithm If we assume the function $f(\mathbf{m})$ to be twice continuously differentiable, we can write Taylor series approximation:

$$f(\mathbf{m}^0 + \Delta\mathbf{m}) \approx f(\mathbf{m}^0) + \nabla f(\mathbf{m}^0)^T \Delta\mathbf{m} + \frac{1}{2} \Delta\mathbf{m}^T \nabla^2 f(\mathbf{m}^0) \Delta\mathbf{m} \quad (3.7.6)$$

Here, we want to find \mathbf{m}^* so that \mathbf{m}^* is a minimum of the objective function $f(\mathbf{m})$. Thus, $f(\mathbf{m}^*)$ will be a minimum iff $\nabla f(\mathbf{m}^*) = 0$. The gradient of $f(\mathbf{m})$ in the vicinity of \mathbf{m}^0 can be approximate

by the first terms of Taylor series:

$$\nabla f(\mathbf{m}^0 + \Delta \mathbf{m}) \approx \nabla f(\mathbf{m}^0) + \nabla^2 f(\mathbf{m}^0) \Delta \mathbf{m} \quad (3.7.7)$$

Setting the gradient (3.7.7) equal to zero, we have:

$$\nabla^2 f(\mathbf{m}^0) \Delta \mathbf{m} = -\nabla f(\mathbf{m}^0) \quad (3.7.8)$$

And solving equation (3.7.8) for successive \mathbf{m}^k , leads to Newton's method for minimizing $f(\mathbf{m})$.

Given a twice continuously differentiable function $f(\mathbf{m})$, and an initial solution \mathbf{m}^0 , Newton's method writes:

1. Solve $\nabla^2 f(\mathbf{m}^k) \Delta \mathbf{m} = -\nabla f(\mathbf{m}^k)$
2. Let $\mathbf{m}^{k+1} = \mathbf{m}^k + \Delta \mathbf{m}$
3. Let $k = k + 1$

The sequence stops when the sequence converges to a solution with $\nabla f(\mathbf{m}) = 0$ (Aster et al., 2013).

Gauss-Newton method The principle of the Gauss-Newton method is based on the minimization of the 2-norm of the residuals. Explicitly, for a non-linear system of equations $\mathbf{G}(\mathbf{m}) = \mathbf{d}$, the goal is to find the model vector \mathbf{m} ($\mathbf{m} \in \mathbb{R}^n$) that best fit the data vector \mathbf{d} ($\mathbf{d} \in \mathbb{R}^m$) in the sense of minimizing the 2-norm of the residuals.

Assuming that the measurements errors are normally distributed, the maximum likelihood principle leads us to minimizing the sum of squared errors normalized by their respective standard deviations σ_i . The objective function $f(\mathbf{m})$ to minimize is written:

$$f(\mathbf{m}) = \sum_{i=1}^m \left(\frac{G(\mathbf{m})_i - d_i}{\sigma_i} \right)^2 \quad (3.7.9)$$

For further convenience, let write:

$$f_i(\mathbf{m}) = \frac{G(\mathbf{m})_i - d_i}{\sigma_i} \quad \text{with } i = 1, \dots, m \quad (3.7.10)$$

and

$$\mathbf{F}(\mathbf{m}) = \begin{bmatrix} f_1(\mathbf{m}) \\ \vdots \\ f_m(\mathbf{m}) \end{bmatrix} \quad (3.7.11)$$

Let calculate $\nabla f(\mathbf{m})$ and $\nabla^2 f(\mathbf{m})$.

$$\nabla f(\mathbf{m}) = \sum_{i=1}^m \nabla (f_i(\mathbf{m})^2) \quad (3.7.12)$$

The elements of the gradient are

$$\nabla f(\mathbf{m})_j = 2 \sum_{i=1}^m f_i(\mathbf{m}) \frac{\partial f_i(\mathbf{m})}{\partial m_j} \quad (3.7.13)$$

$$= 2 \cdot \mathbf{F}(\mathbf{m})^T \cdot \frac{\partial \mathbf{F}(\mathbf{m})}{\partial m_j} \quad (3.7.14)$$

Let express $\mathbf{J}(\mathbf{m})$ the Jacobian of $\mathbf{F}(\mathbf{m})$

$$\mathbf{J}(\mathbf{m}) = \begin{bmatrix} \frac{\partial f_1(\mathbf{m})}{\partial m_1} & \cdots & \frac{\partial f_1(\mathbf{m})}{\partial m_n} \\ \vdots & \ddots & \vdots \\ \frac{\partial f_m(\mathbf{m})}{\partial m_1} & \cdots & \frac{\partial f_m(\mathbf{m})}{\partial m_n} \end{bmatrix} \quad (3.7.15)$$

We can rewrite equation (3.7.12)

$$\nabla f(\mathbf{m}) = 2\mathbf{J}(\mathbf{m})^T \mathbf{F}(\mathbf{m}) \quad (3.7.16)$$

Proceeding similarly to calculate the ∇^2 term

$$\nabla^2 f(\mathbf{m}) = \sum_{i=1}^m \nabla^2 (f_i(\mathbf{m})^2) \quad (3.7.17)$$

$$= \sum_{i=1}^m \mathbf{H}^i(\mathbf{m}) \quad (3.7.18)$$

With $\mathbf{H}^i(\mathbf{m})$ the Hessian of $f_i(\mathbf{m})^2$. The j, k element of $\mathbf{H}^i(\mathbf{m})$ is

$$H_{j,k}^i(\mathbf{m}) = \frac{\partial^2 (f_i(\mathbf{m})^2)}{\partial m_j \partial m_k} \quad (3.7.19)$$

$$= \frac{\partial}{\partial m_j} \left(2f_i(\mathbf{m}) \frac{\partial f_i(\mathbf{m})}{\partial m_k} \right) \quad (3.7.20)$$

$$= 2 \left(\frac{\partial f_i(\mathbf{m})}{\partial m_j} \frac{\partial f_i(\mathbf{m})}{\partial m_k} + f_i(\mathbf{m}) \frac{\partial^2 f_i(\mathbf{m})}{\partial m_j \partial m_k} \right) \quad (3.7.21)$$

Neglecting the term with second order derivative, we can write

$$\nabla^2 f(\mathbf{m}) \approx 2\mathbf{J}(\mathbf{m})^T \mathbf{J}(\mathbf{m}) \quad (3.7.22)$$

This approximation is reasonable as we approach the optimal parameters \mathbf{m}^* but can be unrealistic for non-linear least squares problems in which the values of $f_i(\mathbf{m})$ are large.

Equations (3.7.16) and (3.7.22) leads to Gauss-Newton method. The algorithm is the same as for Newton method, but equation (3.7.8) is written

$$\mathbf{J}(\mathbf{m}^k)^T \mathbf{J}(\mathbf{m}^k) \Delta \mathbf{m} = -\mathbf{J}(\mathbf{m}^k)^T \mathbf{F}(\mathbf{m}^k) \quad (3.7.23)$$

Even if it works well in practice, Gauss-Newton method is based on Newton's method and have the same limitations. Also, the method is inappropriate when the matrix $\mathbf{J}(\mathbf{m}^k)^T \mathbf{J}(\mathbf{m}^k)$ is singular (Aster et al., 2013).

Levenberg-Marquardt method In geophysics, data generally contains noise, and having a model that perfectly fits the data can lead to unrealistic results. At some point, and especially for high numbers of iterations, additional reduction of the RMS can lead to modelling of the noise. To overcome this limit of the Gauss-Newton method and obtain smoother models, Levenberg-Marquardt method consider a additional regularization term in the objective function to minimize. Let write $\phi(\mathbf{m})$ the function to minimize, we have

$$\phi(\mathbf{m}) = \sum_{i=1}^m \left(\frac{G(\mathbf{m})_i - d_i}{\sigma_i} \right)^2 + \lambda \sum_{i=1}^m m_i^2 \quad (3.7.24)$$

Thus, equation (3.7.23) becomes

$$\left(\mathbf{J}(\mathbf{m}^k)^T \mathbf{J}(\mathbf{m}^k) + \lambda \mathbf{I} \right) \Delta \mathbf{m} = -\mathbf{J}(\mathbf{m}^k)^T \mathbf{F}(\mathbf{m}^k) - \lambda \mathbf{m}^k \quad (3.7.25)$$

And using a positive value of λ ensures that the matrix $(\mathbf{J}(\mathbf{m}^k)^T \mathbf{J}(\mathbf{m}^k) + \lambda \mathbf{I})$ is non singular (Aster et al., 2013).

Occam's inversion Occam's method allows to take into account *a priori* information to improve the quality of the model. In fact, the regularization term is modified so that it takes into account the way adjacent parameters of the model varies. A common way of evaluating the variation of adjacent parameters of the model is to consider the first order difference matrix \mathbf{L} ($\mathbf{L} \in \mathbb{R}^{n \times n}$)

$$\mathbf{L} = \begin{bmatrix} -1 & 1 & 0 & \cdots & 0 & 0 \\ 0 & -1 & 1 & \cdots & 0 & 0 \\ 0 & 0 & -1 & \cdots & 0 & 0 \\ \vdots & \vdots & \vdots & \ddots & \vdots & \vdots \\ 0 & 0 & 0 & \cdots & -1 & 1 \\ 0 & 0 & 0 & \cdots & 0 & 0 \end{bmatrix} \quad (3.7.26)$$

Where anisotropy can be taken into account by weighting the different direction of space. Hence

$$\mathbf{W}_m = \alpha_x \mathbf{L}_x^T \mathbf{L}_x + \alpha_z \mathbf{L}_z^T \mathbf{L}_z \quad (3.7.27)$$

In general, this approach is more realistic as it is reliable to assume that the changes in the subsoil are smooth and continuous. But in some cases where sharp boundaries in the medium are expected (e.g. faulting, strong geological contrast) this assumption can lead to unexpected results.

Writing $\mathbf{W}_d = \text{diag}(1/\sigma_1, \dots, 1/\sigma_m)$ the objective function to minimize becomes

$$\phi(\mathbf{m}) = \|\mathbf{W}_d (\mathbf{G}(\mathbf{m}) - \mathbf{d})\|^2 + \lambda \|\mathbf{W}_m \mathbf{m}\|^2 \quad (3.7.28)$$

And equation (3.7.25) becomes

$$\left(\mathbf{J}(\mathbf{m}^k)^T \mathbf{J}(\mathbf{m}^k) + \lambda \mathbf{W}_m^T \mathbf{W}_m \right) \Delta \mathbf{m} = - \left(\mathbf{J}(\mathbf{m}^k)^T \mathbf{F}(\mathbf{m}^k) + \lambda \mathbf{W}_m^T \mathbf{W}_m \mathbf{m}^k \right) \quad (3.7.29)$$

This expression is general for any matrix \mathbf{W}_m . Thus, this matrix can easily be change to incorporate statistical information or to evaluate higher order difference matrix (Aster et al., 2013; Hermans, 2010; Sharma and Verma, 2015).

3.7.3 Effect of temperature on resistivity

The electrical resistivity of the subsoil is influenced by temperature variations. Above 0°C it decreases linearly by about 2%/°C with increasing temperatures (Hayley et al., 2007; Uhlemann et al., 2016). The resistivity changes induced by seasonal temperature variation can be of the same order than the resistivity variations induced by hydrological processes. Hence, the effect of the temperature on the resistivity needs to be corrected to avoid misinterpretation of the monitoring data.

We first develop a time-depth temperature model of the subsoil. Then we determine the law that models the variation of resistivity with temperature. Finally we apply the resistivity-temperature law on the resistivity model obtained from the inversion, which allows to correct the effect of temperature on resistivity.

3.7.3.1 Temperature modelling

Seasonal temperature changes in the subsoil is described by (Chambers et al., 2014; Uhlemann et al., 2016)

$$T(z, t) = T_{mean} + \frac{\Delta T}{2} e^{-(z/d)} \sin \left(\frac{2\pi}{365} t + \phi - \frac{z}{d} \right) \quad (3.7.30)$$

Where

- $T(z, t)$ [°C]: is the temperature at day t [days] and depth z [m],

- T_{mean} [°C]: is the mean yearly temperature,
- ΔT [°C]: is the yearly peak-to-trough amplitude of the air temperature variation,
- d [m]: is the characteristic penetration depth of the temperature variations, and
- ϕ [-]: is the phase offset.

3.7.3.2 Temperature correction

If a model of the subsoil temperature changes have been established, we can apply a temperature correction on the resistivity model. Two approaches can be considered to explain the variation of resistivity with temperature. One approach is to consider an exponential law (Hermans, 2010)

$$\frac{\rho_{25}}{\rho_T} = e^{-\frac{A}{R}(\frac{1}{T} - \frac{1}{298})} \quad (3.7.31)$$

And the other is to consider a linear model (Hayley et al., 2007)

$$\frac{\rho_{25}}{\rho_T} = 1 + m (T - 25) \quad (3.7.32)$$

Where ρ_{25} is the resistivity at 25°C [$\Omega \cdot m$], ρ_T is the resistivity at temperature T [$\Omega \cdot m$], A is the activation energy of conduction [$J \cdot mol^{-1}$], R is the universal gas constant [$J \cdot mol^{-1} \cdot K^{-1}$], T is the temperature (in [°K] for the exponential model and in [°C] in the linear model), and m is the fractional change in conductivity by degree celsius. A value of 0.02 is generally used for the parameter m (Chambers et al., 2014; Hayley et al., 2007).

In the case of this study, a linear model similar to equation 3.7.32 was considered to characterize the resistivity change due to temperature variations.

Chapter 4

Old Dalby landslide study site

4.1 General presentation

The Old Dalby landslide study site relies on a relict landslide where the PRIME system (see SECTION 4.5) has been installed. The PRIME system is a tool developed by the British Geological Survey to provide real-time 4D electrical resistivity monitoring. The monitoring survey profiles are divided in 5 lines covering the relict landslide and its surroundings. The 5 monitoring lines are labelled L1, L2, L3, L4, L5 and are visible at FIG. 4.1. The gathering of the geophysical information and the laboratory data should allow a better understanding of the short and long term dynamics of the water movement in the subsoil. The resistivity data covers a 1.5 years period ranging from October 2015 till March 2017 with daily measurements.

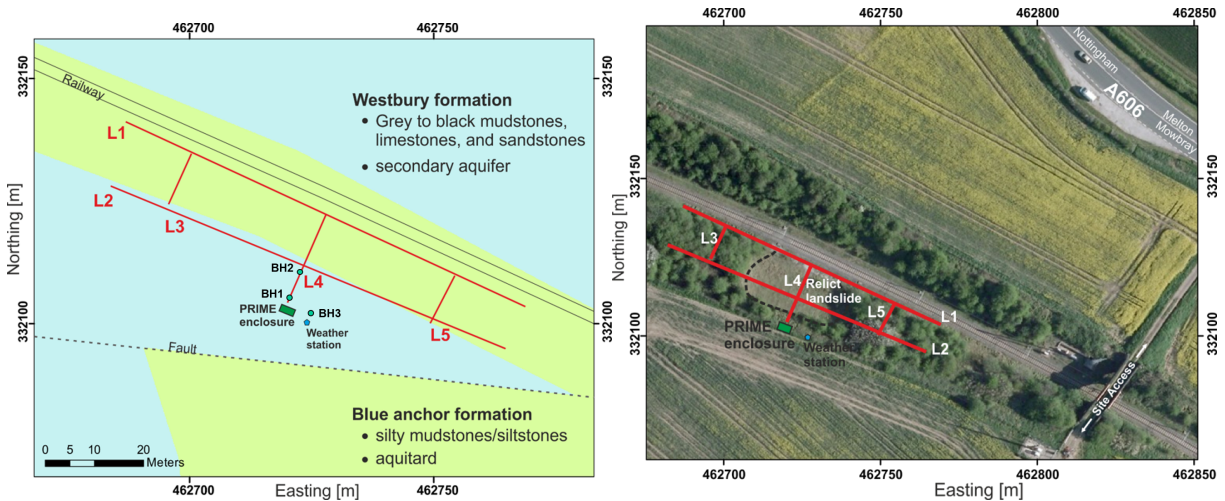


Figure 4.1: Location and geology of Old Dalby

4.2 Local geology

The subsoil of Old Dalby is essentially composed of clayey material. More precisely it is composed of the Westbury Formation and the Blue Anchor Formation, which are covered by quaternary glacial tills, the Thrussington Tills. At the Old Dalby site, the Thrussington Tills are likely to result from the shuffling of the Cropwell Bishop Formation. A geological log of a borehole drilled above the railway cutting is described in SECTION. 4.3.

The material used for the laboratory testing consists of glacial tills from auger drilling (FIG. 4.2). It contains coarse pebbles and has a high clay/silt fraction with a brownish tint. The location of the drilling is shown at Fig. 4.1, where the BH1, BH2 and BH3 labels corresponds to drillings located:

BH1: Downslope of weather station - 0.5-0.9 m

BH2: On bench BH - 0.8-1.3 m

BH3: Near weather station - 0.6-1.2 m

The results from the soil characterisation laboratory testing is described precisely in CHAPTER 5.



Figure 4.2: Old Dalby material for laboratory testing

4.3 Core characterization

4.3.1 Geological log

A core was drilled on top of Old Dalby railway cutting (next to the weather station) to improve the knowledge of its subsoil. The drill core is 6.84 m long and was sealed into 6 cores of 1.00 m and 1 core of 0.84 m. The different parts of the core can be seen at FIGURE 4.3, where the lithology is represented with its corresponding electrical resistivity and moisture content values. The geological description of the core (see ANNEX B for more details) can be synthesized as following:

- The first 0.65 m of soil contains loose darkish reddish brown sandy gravel and round pebbles. The observation of the round pebbles and of the fragments of pottery drain suggests the presence of an old drainage system.
- From 0.65 m to 5.85 m, the core is relatively uniform and corresponds to the Thrussington Tills. The tills are stiff and have a uniform reddish brown tint with calcareous clasts inclusions. The tills are locally disturbed by the presence of horizontal fractures. Those fractures are not necessarily characteristic of the subsoil as they could have been triggered by the drilling process.
- The area ranging from 5.85 m to 5.95 m marks the transition from the Thrussington Tills to the Westbury Formation. It corresponds to a loose uniform darkish brown sandy layer.
- From 5.95 m to 6.84 m, we found the Westbury Formation. It is a stiff greyish black clay with occasional angular gravel. Like in the tills, we observe the presence of some horizontal fractures, but these are believed to be drilling artefacts.

4.3.2 Resistivity measurements on core

The electrical properties of the core have been studied and were compared to the observed lithology. Even if the cores were well preserved, sealed in a plastic cylinder and conserved in a cold chamber, they are likely to have lost a small percentage of their water content and the results obtained might differ slightly from the results that would be obtained in-situ. To avoid temperature deviation, the cores were let to equilibrate to room temperature ($\approx 22^\circ\text{C}$) before the measurements. The following measurements were made on each core samples: galvanic measurements, non contact resistivity measurements and 5TE measurements.

Each of these measurements aims to calculating the resistivity so that the results from the different methods can be compared. Especially the comparison of the results makes it possible to

assess the reliability of the in-situ 5TE measurements. Unfortunately, no moisture samples could be taken on the core, so that no information on the reliability of the moisture content calculated from the 5TE measurements could be gathered.

The sealed cores had to be open to realise their geological description. They are now recovered by black tape where the cutouts were made. To avoid the measurement effect that the tape appears to have on the results, the measurements of the non contact were made at the opposite of the adhesive tape that seals the cores. To optimize the consistency between the non contact measurements made on each core and minimize the drift effect, we performed the measurements made on each core directly one after the others. We see in Table 4.1 that the drift remained low between each core measurement.

Table 4.1: Drift of the non contact measurement device during measurements

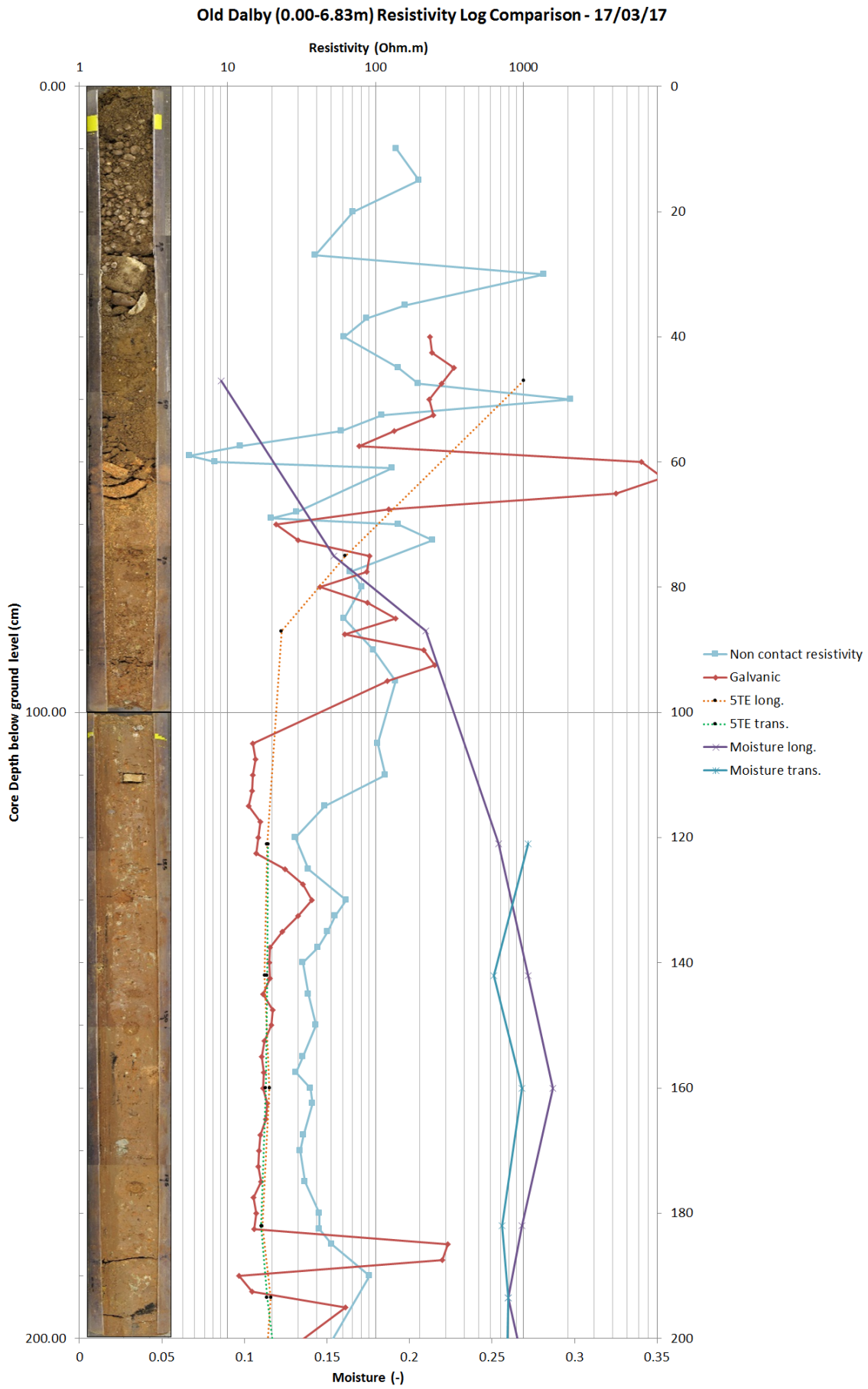
Core n°	0-1 m	1-2 m	2-3 m	3-4 m	4-5 m	5-6 m	6-6.83 m
Background start	0.007V	0.010V	0.014V	0.014V	0.007V	0.011V	0.025V
Background end	0.009V	0.012V	0.013V	0.011V	0.009V	0.009V	0.024V
Drift	0.002V	0.002V	0.000V	-0.004V	0.001V	-0.002V	0.000V

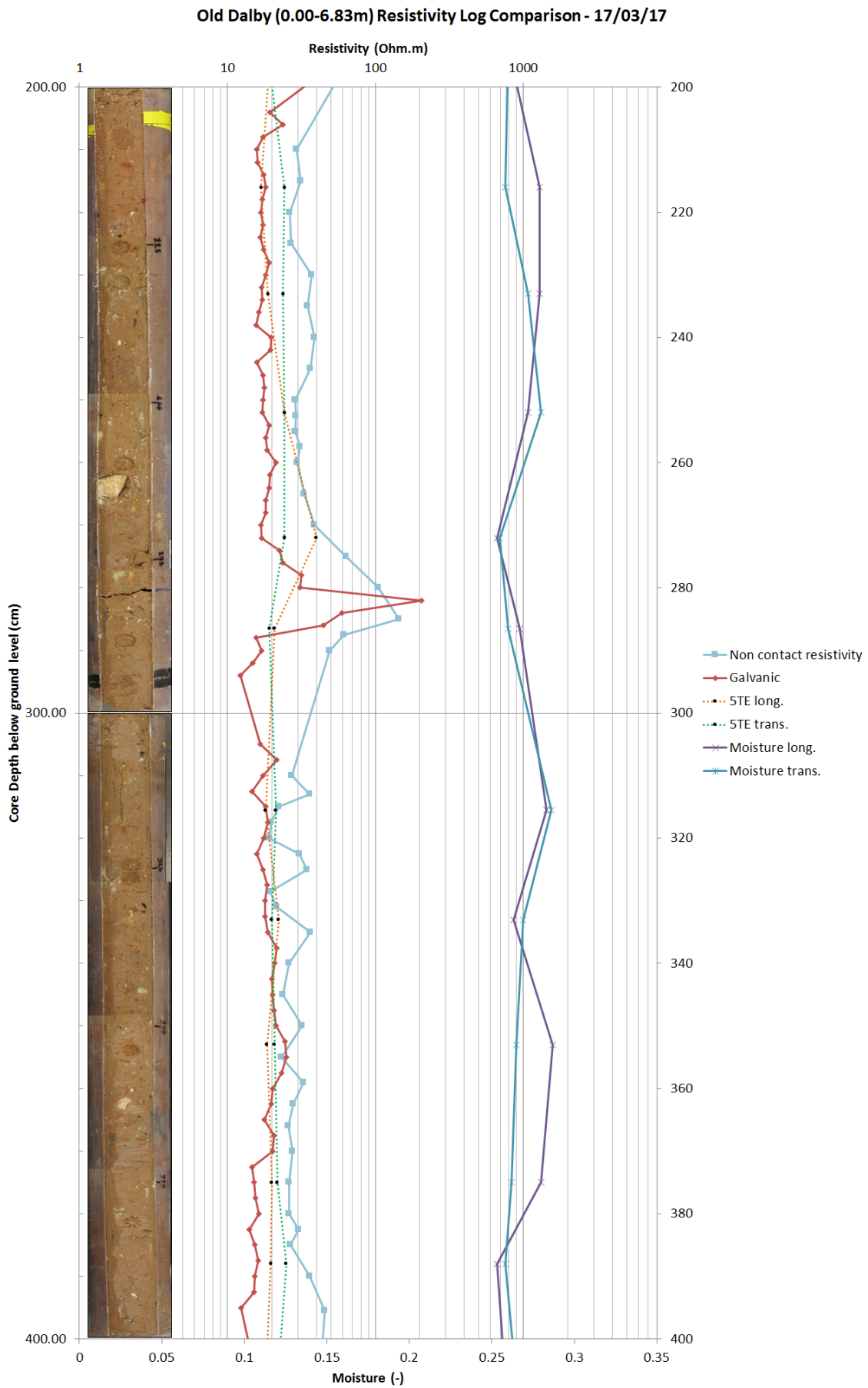
There is no data for the galvanic and the 5TE measurements in the top 40 cm because the poor electrode contact in this area prevented the measurement for being taken.

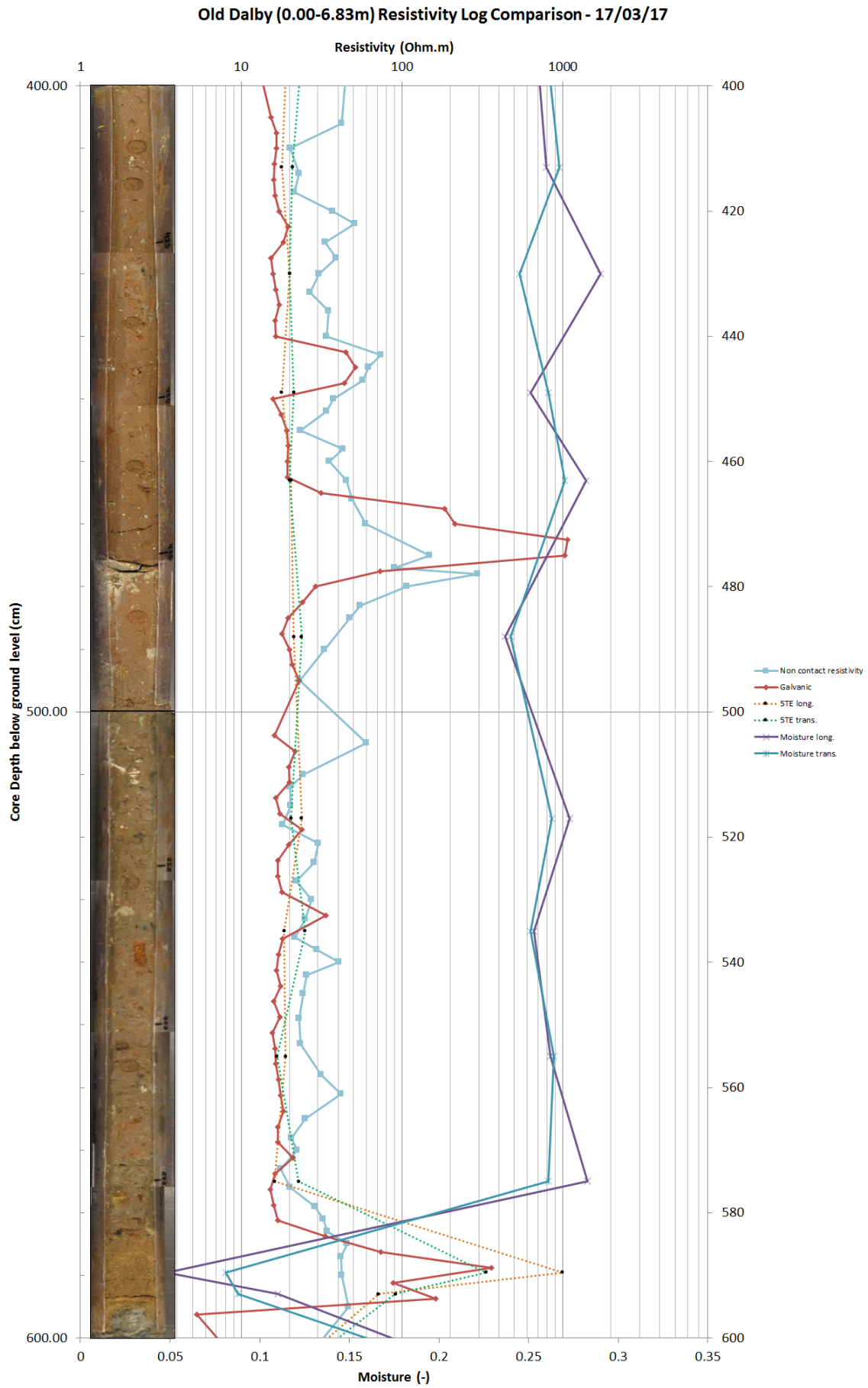
When we look at the results from FIG. 4.3, we observe a few Dirac-like resistivity increases of the galvanic and the non contact measurements (0.60 m, 1.85 m, 2.8 m, 4.7 m, 6.4 m). By comparing these observations with the pictures of the core, we realise that those sharp increases are systematically due to the presence of a crack or a fractured area. The resistivity increase that we observe between 5.85 m and 5.95 m is slightly different because it has a plateau shape. The observation of the core has allowed to link this resistivity contrast to the presence of a loose uniform sandy layer.

The 5TE probe shows that the top 1 m core has a lower moisture content. This could be attributed to bad conservation of the core or to low moisture content when the coring was done. Below 2 m core depth, the moisture content stabilize between 0.25 and 0.30 volumetric moisture content. Assuming a dry density of the till ranging between 1.3 and 1.6, the gravimetric moisture content would be comprise between 0.16 and 0.23. This means that the till is at its plastic limit and hence susceptible to deformation and slipping.

In comparison with the galvanic measurements, the non contact resistivity measurements tend to over-estimate the resistivity. Nevertheless, for each core the offset with the galvanic measurements seems to be constant and the same trend is represented with both methods. The non contact method has the strength to be non-intrusive as it doesn't require the sealed cores to be opened. The non contact method is very efficient for the recognition of cracks, fractured areas and resistivity contrasts (e.g. the sandy layer between 5.80 and 6 m depth) but is not reliable to measure precisely the absolute resistivity of a given part of the core. When no fractures are present, the 5TE measurements give resistivity values close to those of the galvanic measurements.







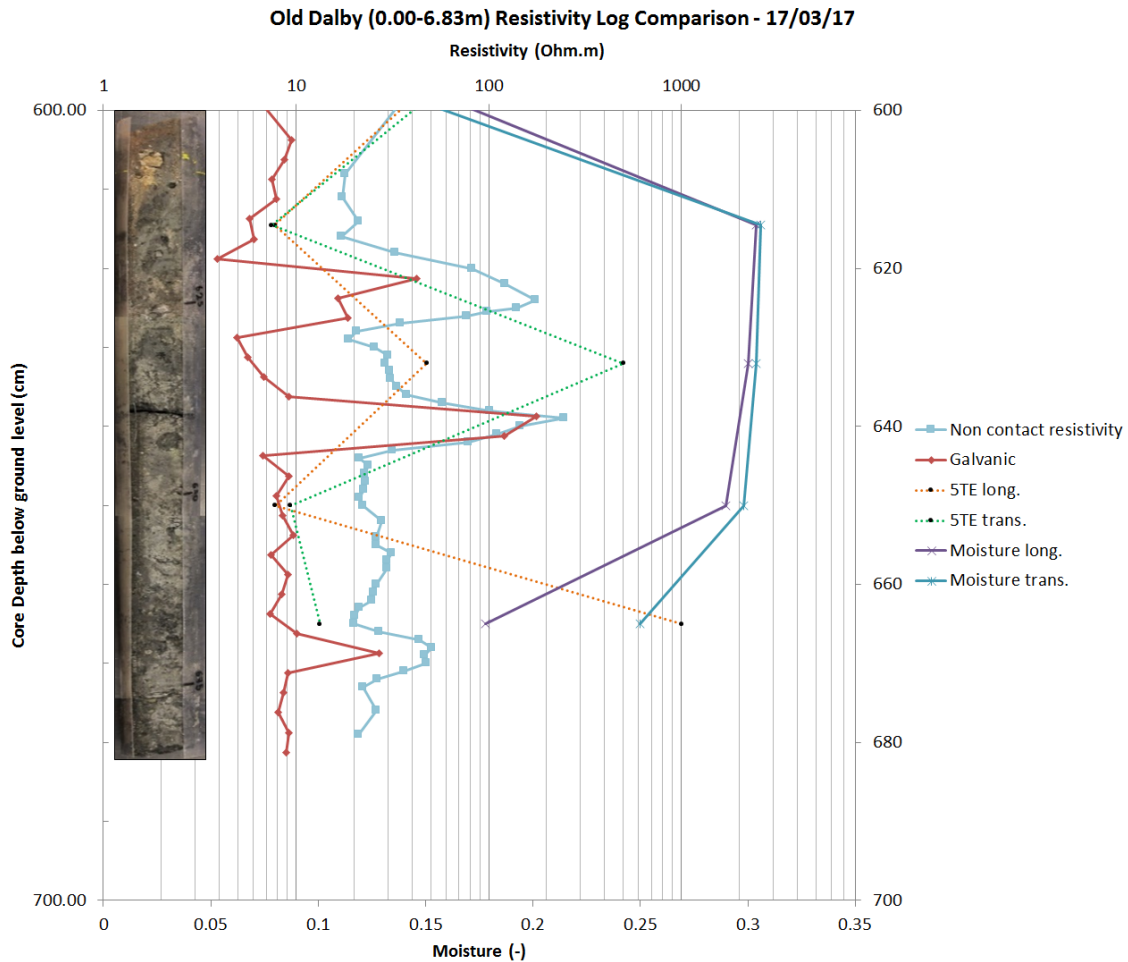


Figure 4.3: Old Dalby core. Comparison of the non contact resistivity imaging, with the galvanic resistivity measurements and the 5TE resistivity and moisture measurements

4.4 Landslide mechanism and activity

The Old Dalby landslide is a relict landslide that has a rotational mechanism. It is likely to have taken place within the tills or the underlying mudstone, but local investigations should be done to confirm it. The geological context of the Old Dalby landslide is schemed at FIGURE 4.4. The thickness of the layer labelled as the Westbury Formation is unsure and could be misinterpreted as a disturbed zone in the Blue Anchor Formation. Nevertheless, the resistivity values of this layer is less than $10 \Omega.m$, which is consistent with Westbury mudstones. Also, it is common for slip planes to develop in mudstones of the Westbury Formation in the vicinity of the studied area (D. Gunn, Personal Statement, 2017).

People who remember the slide recall the material slipping onto the tracks, which was removed to clear the tracks and spread over local playing fields. The disturbed, slipped soil that normally accumulate at the toe of a landslide is therefore no longer present. And the talus-like horizontal platform below the landslide is in fact a cut within the Blue Anchor that acts as a small berm to prevent any material falling from the unstable upper slope (D. Gunn, Personal Statement, 2017).

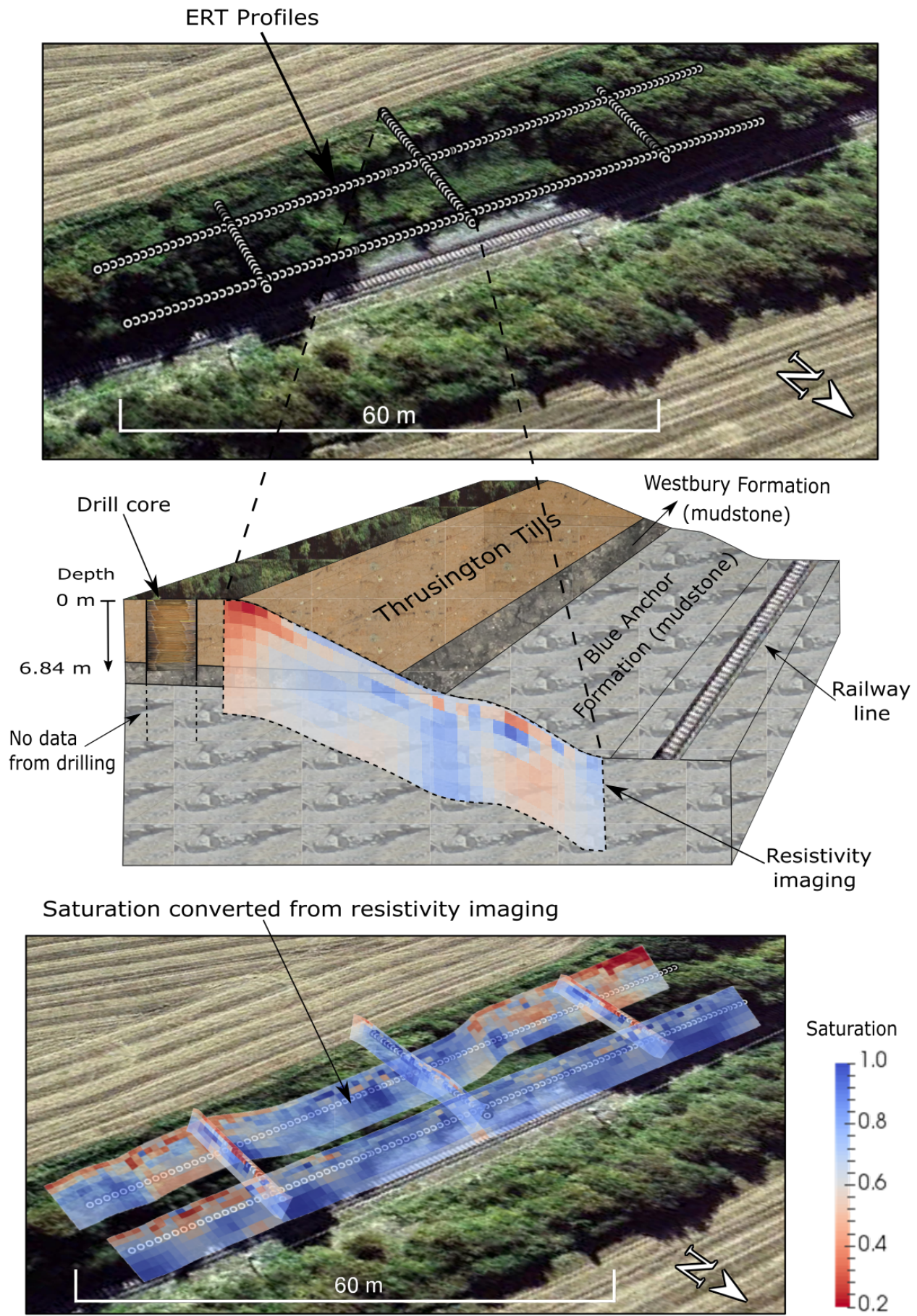


Figure 4.4: Old Dalby landslide geological context

4.5 Monitoring (Prime System)

The Old Dalby landslide is monitored by the PRIME System (Proactive Infrastructure Monitoring and Evaluation). The PRIME system is a new low cost (\approx £7K) - low power (10 W) 4D ground resistivity imaging system for critical zone monitoring.

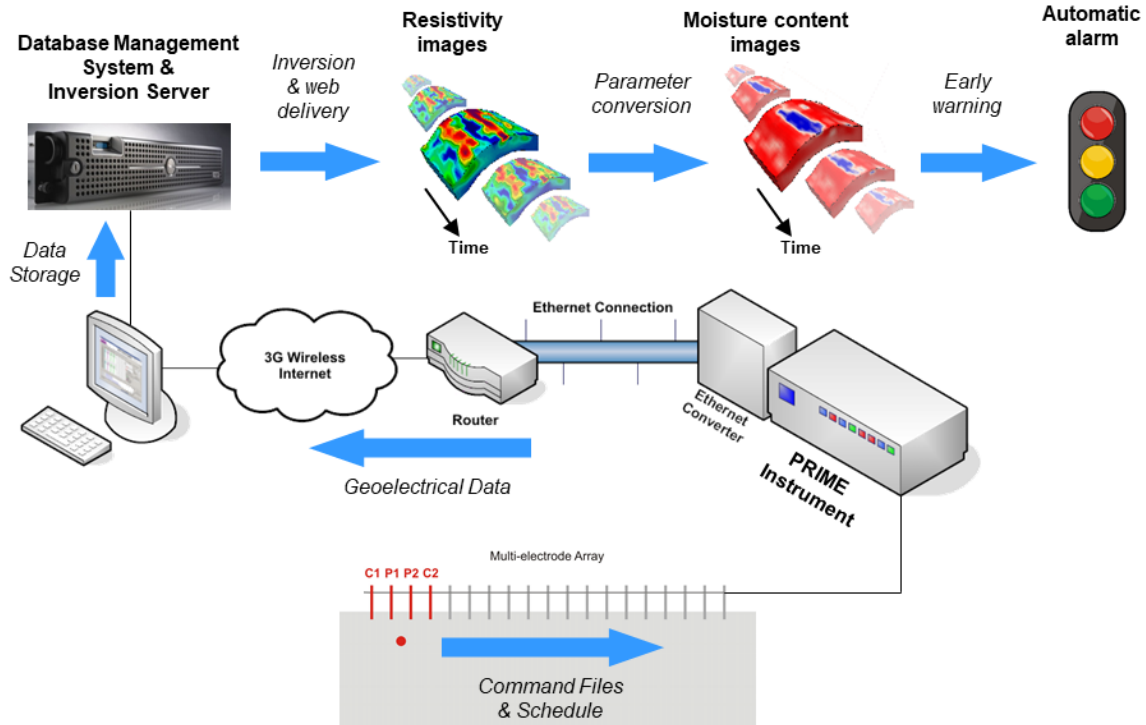


Figure 4.5: Prime system principle

It is developed at the BGS and is applicable to a wide range of monitoring applications (e.g. groundwater saturation, contaminants transport). The data acquisition is based on electrical resistivity tomography. Thus the PRIME system is rapid and non-invasive and based on laboratory measurements it is able to provide volumetric information about moisture content. The setup and control operated with a command file accessible via Ethernet. In addition to the ERT monitoring, the PRIME system also includes a weather station and Decagon 5TE moisture sensors installed within the subsoil. The meteo station can record multiple variables such as the temperature, the rainfall and the humidity. The Decagon 5TE sensors are able to record 3 variables: the temperature, the moisture content and the electrical conductivity.

The Old Dalby landslide is monitored by 5 geoelectrical profiles (FIG. 4.1) with multi-electrode array. Daily measurements are made and transmitted to the database by internet (FIG. 4.5). The measurements are inverted with RES2DINV to obtain resistivity images that can be converted into moisture content images after parameter conversion. The objective of the method is to provide an early warning when the subsoil reaches a certain saturation level. In addition to the resistivity monitoring, 5TE probes are present at different depths of the subsoil. These probes measure the temperature of the subsoil, which makes it possible to develop a temperature model of the subsoil. They also measure the volumetric moisture content of the soil, which can be compared to the measured local precipitations as well as the inverted moisture content data.

Chapter 5

Laboratory characterization

The mechanical properties of the subsoil of Old Dalby have been studied in laboratory and a laboratory relation between the moisture content, the suction and the resistivity of the subsoil has been established. The following tests were performed on the samples:

- Atterberg limits (plastic and liquid limit)
- Particle size analysis
- Compaction tests
- Suction tests
- Resistivity-moisture measurements

The suction and resistivity-moisture measurements were realised on compacted material from three boreholes drilled on site (BH1, BH2 AND BH3, see Fig. 4.1). To make the samples preparation reproducible and have samples close to the in-situ material, the material was compacted using the standard 'light' proctor compaction test (BS1377:Part 4:1990:3.3) assuming the optimum moisture content (OMC) was close to their plastic limit. The optimum moisture content was not evaluated as the available material was not sufficient.

5.1 Atterberg limits

5.1.1 Liquid limit

The liquid limit is evaluated by interpolating the moisture content that would produce a 20 mm penetration. The results are shown at Fig. 5.1 where we deduce that the values of the liquid limit for BH1, BH2 and BH3 are respectively 39%, 38% and 44% (Table 5.2). BH3 shows a liquid limit relatively higher than BH1 and BH2. We could try to relate this observation to the PSA of BH3 which has a higher sand content, but it is not reliable as the liquid limits normally decrease as the sand content increase. This could be due to the weathering of the material, following Hobbs et al. (2002) the liquid limit of the Mercia Mudstone that is similar to the studied tills tends to increase with the weathering.

5.1.2 Plastic limit

The results of the plastic limit are shown at Table 5.1. The values for the different samples are similar, ranging between 17% to 19%.

5.1.3 Plasticity index

In our case, the Old Dalby samples have a plasticity index greater than 20 (Table 5.2), thus being classified as highly plastic, which is consistent with the clay content of the samples (Fig. 5.2).

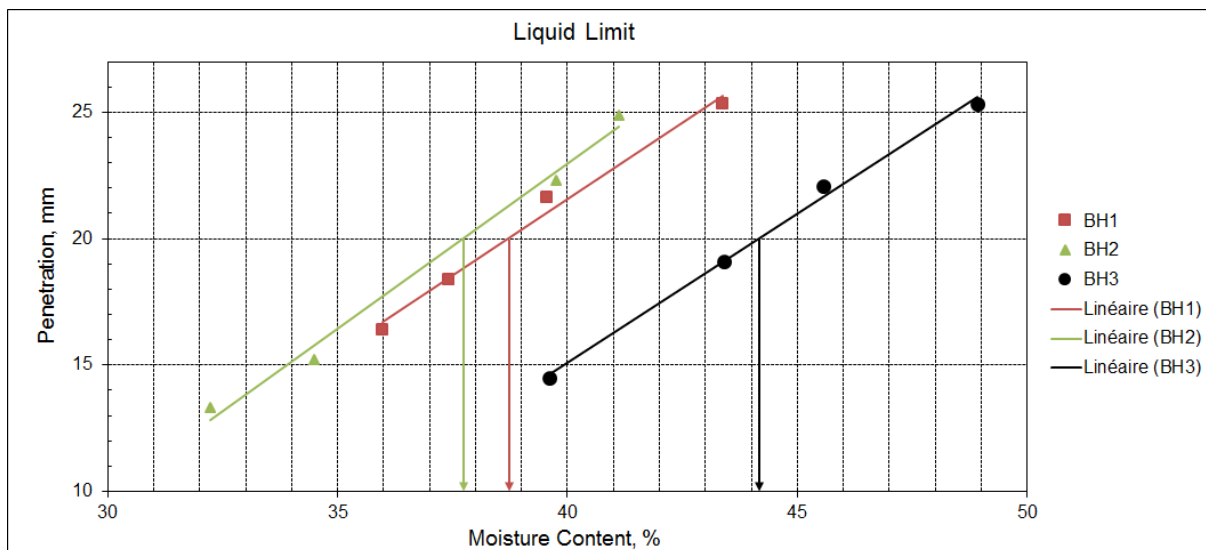


Figure 5.1: Liquid limit

Borehole	1	2	3
Value 1 (%)	18.1	16.8	19.1
Value 2 (%)	19.2	17.7	19.5
Plastic Limit (%)	19	17	19

Table 5.1: Plastic limit (in GMC)

5.2 Particle size analysis

The particle size analysis obtained for our samples is represented in Fig. 5.2. The particle size distribution is similar for the three samples, however the samples from the borehole 3 has a significantly larger sand proportion (Table 5.3). The analyses of the PSD for all 3 samples shows that those are all poorly sorted. This is typical for many UK glacial tills. Regarding to the PSD, the engineering geological description for those soils would be sandy clay.

5.3 Resistivity-moisture content characterization

5.3.1 Resistivity coffins preparation

The samples were prepared using the standard 'light' proctor compaction test (BS1377:Part 4:1990:3.3) assuming the optimum moisture content (OMC) is close to their plastic limit. Once compacted, the soil was left 48 hours in a sealed bag so the water content could equilibrate properly. Four resistivity

BH	1	2	3
Plastic Limit (%)	18.7	17.2	19.3
Liquid Limit (%)	39.0	38.0	44.0
Plasticity Index (%)	20	21	25

Table 5.2: Plastic limit, liquid limit and plasticity index (in GMC)

BH	1	2	3
Gravel (%)	7.2	2.0	4.3
Sand (%)	26.3	28.3	36.7
Silt (%)	29.9	32.6	23.4
Clay (%)	36.5	37.1	35.5

Table 5.3: Proportion of gravel, sand, silt and clay

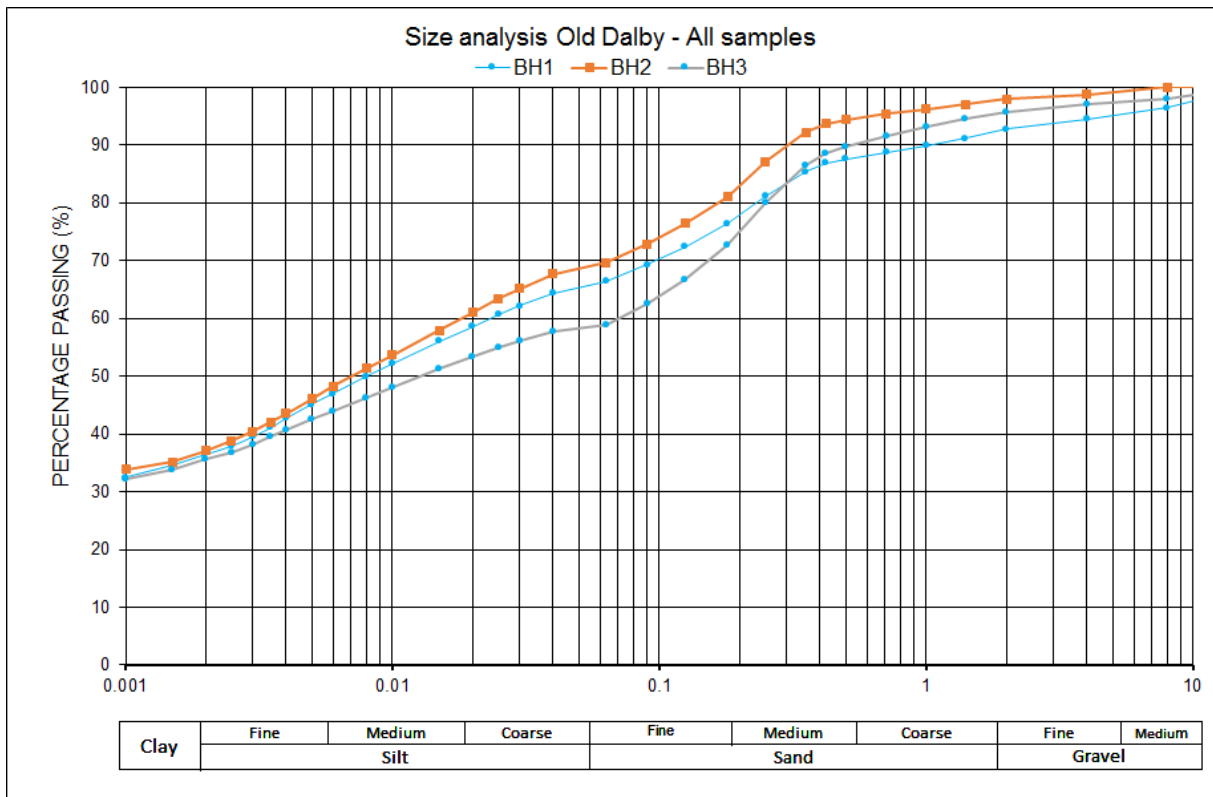


Figure 5.2: Old Dalby Particle Size Analysis

coffins were made from the compacted material. Three samples were taken horizontally and the last one was taken vertically (FIG. 5.3).

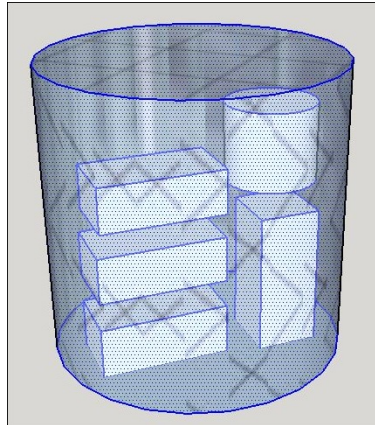


Figure 5.3: Samples cutting in proctor mould

5.3.2 Measurements

The time required to let the water contents within the samples to equilibrate prevented from doing more than one measurement per day. Measurements were done in the morning. The samples were then left unsealed in the laboratory room for a few hours so that their moisture content could decrease, before being sealed again until the next morning. The drying speed of the samples was around 0.2-0.25% GMC/hour when the samples had a GMC of $\approx 18\%$. The more the samples were dry and the more time they needed to loose their contained water. Before each measurement the resistivity coffins were weighted to track the variation of moisture content.

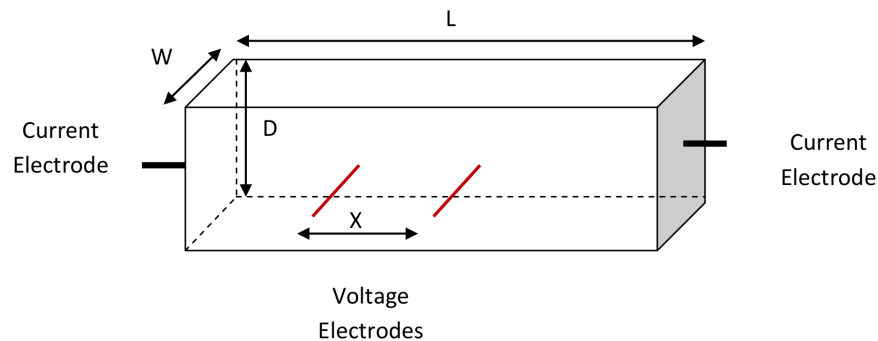


Figure 5.4: Resistivity coffins

The resistivity measurements were made using the ABEM TERRAMETER on the resistivity coffins (FIG. 5.4). The resistivity coffins are made of plastic and have one metallic plate at each ends where the current is injected. Two holes are present to place the measurement electrodes in the middle of the coffins with an electrode spacing, x , of 2.5 cm. The measurement electrodes are placed after introducing the soil sample in the coffins. They stay in place during all the measurements. The metallic plates are compressed with two elastics so that the plates stay in contact with the samples when they shrink. The length and the width of the sample is taken before each measurement. Each resistance measurement is made using 4 stacks and both normal and reciprocal measurements are taken. The resistance value obtained from the ABEM TERRAMETER is converted into resistivity

using

$$\rho = \frac{(R_1 + R_2).l.h}{2.x} \quad (5.3.1)$$

with R_1 the normal resistance, R_2 the reciprocal resistance, l the width of the sample measured before measurement (in case of shrinkage), h the height of the sample and x the measurement electrodes spacing ($x = 2.5$ cm).

When the samples started to be very dry ($<1\%$ moisture content), the resistivity of the samples could not be measured because of really poor plate sample electrode contact. This was overcome by wetting the plates a little bit so that the current could propagate through the samples.

5.4 Waxman-Smits

A very large set of moisture-resistivity measurements (FIGURE 5.5) was completed in laboratory, aiming to fit a Waxman-Smits model on the laboratory data.

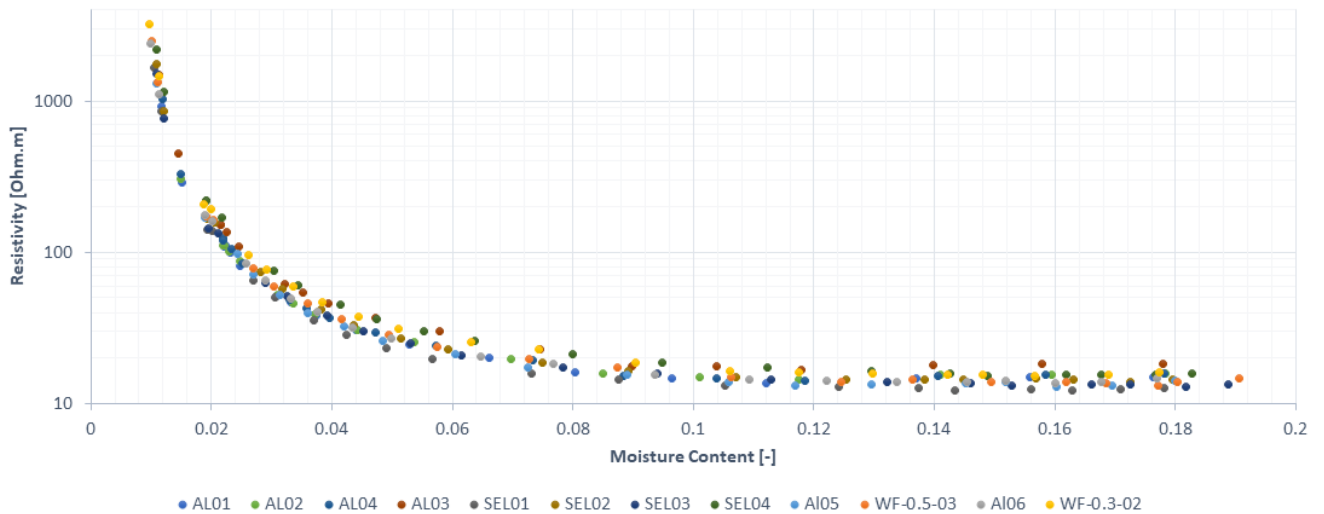


Figure 5.5: Resistivity-Moisture dataset from the laboratory characterization of re-compacted samples from Old Dalby

The weight and the dimensions of the resistivity samples were taken before every measurements. From this we can evaluate the saturation at every moment, writing m_s and V_s respectively the mass and the volume of the soil sample, we can write

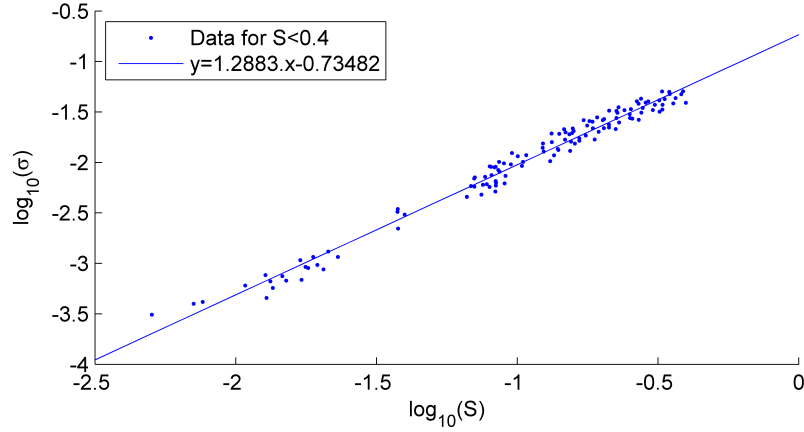
$$S = w \left(\frac{m_s}{\left(V_s - \frac{m_{dry}}{d_s} \right) d_w} \right) \quad (5.4.1)$$

We assume $d_w = 1$ g/cm³ and $d_s = 2.65$ g/cm³. From equation (3.5.12), we can determine the parameter n analytically. Expressing the logarithm of expression (3.5.12) we have

$$\log_a \sigma_0 = (n - 1) \log_a S + \log_a \left(\frac{\sigma_{e,sat}}{F} \right) \quad \text{if } S \text{ is small} \quad (5.4.2)$$

From the linear regression (Fig. 5.6), we have $n = 2.2883$. The intercept $p = -0.735$ of the linear predictor constraint the ratio $\sigma_{e,sat}/F$. Thus, we have

$$F = \sigma_{e,sat}.a^p \quad (5.4.3)$$

Figure 5.6: Linear fit for $S < 0.4$.

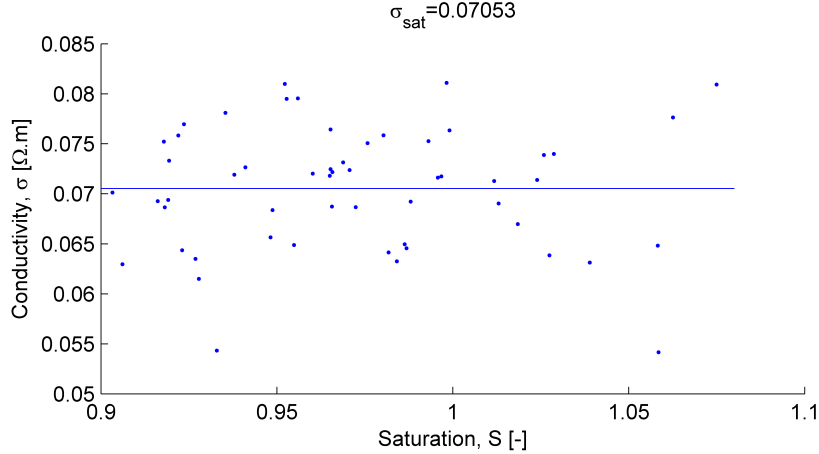
At saturation ($S = 1$), we have

$$\sigma_{sat} = \frac{1}{F} (\sigma_w + \sigma_{e,sat}) \quad (5.4.4)$$

Considering the relation between F and $\sigma_{e,sat}$, expression (5.4.4) rewrites

$$\sigma_{e,sat} = \frac{\sigma_w}{\sigma_{sat} \cdot a^{-p} - 1} \quad (5.4.5)$$

The value of σ_{sat} was calculated by considering the mean value of the conductivity around saturation (FIG 5.7). This yields to $\sigma_{sat} = 0.0705$

Figure 5.7: Evaluation of σ_{sat}

The resistivity samples were prepared using deionised water. As we let some time to the samples to equilibrate, we assume that the water contained in the pores equilibrated with the ions present in the clayey material. Thus, we don't have any control on the parameter σ_w , and we assume a value of $\sigma_w = 1$ S/m. From equations (5.4.3) & (5.4.4), we have $\sigma_{e,sat} = -1.625$ and $F = -8.82$. The negative values of $\sigma_{e,sat}$ and F could not be explained, but the same problem was observed when using an automatic fitting of the parameters.

In the unsaturated area, the porosity is assumed to be constant and from equation (A.0.12), we know that the saturation can be expressed

$$S = \frac{wd_s(1 - \phi)}{d_w \phi} \quad (5.4.6)$$

with d_s the grain density, d_w the water density and ϕ the porosity. Thus, if the porosity is constant, we can write:

$$\phi = \frac{d_s}{md_w + d_s} \quad (5.4.7)$$

Where m is the slope of the linear fit on the partially saturated area of FIG. 5.8. We have $m = 8.234$ which yields to $\phi = 0.25$.

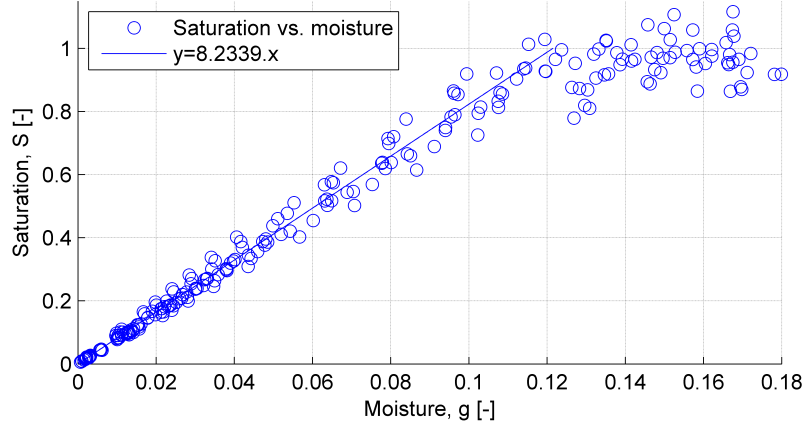


Figure 5.8: Moisture-saturation scatterplot.

Table 5.4: Parameters estimated to establish the Waxman-Smits model for Old Dalby site

Parameter	σ_{sat} [S/m]	n [-]	F [-]	σ_w [S/m]	$\sigma_{e,sat}$ [S/m]	ϕ [-]	d_w g/cm ³	d_s g/cm ³
Value	0.705	2.288	-8.823	1	-1.625	0.25	1	2.65

All the determined parameters are summarized at TABLE 5.4. Inserting the required parameters in the Waxman-Smits model leads to

$$\rho = \left(\frac{S^n}{F} \left(\sigma_w + \frac{\sigma_{e,sat}}{S} \right) \right)^{-1} \quad (5.4.8)$$

We can compare the measured data to our model. The results are shown at FIGURE 5.9. The pearson correlation coefficient of the fit is equal to 0.962. As the resistivity values covers has a exponential behaviour, hence covering a broad range of values, the pearson coefficient was also evaluated for the logarithm of the resistivity, which yields to a pearson coefficient of 0.993. The last subplot of FIGURE 5.9 represents the error between the model and the data, which was calculated following

$$\text{error} = \frac{\rho_{model} - \rho_{data}}{0.5 \cdot (\rho_{model} + \rho_{data})} \quad (5.4.9)$$

We see that for a moisture content ranging from 0.02 to 0.06, the Waxman-Smits model tends to overestimate the resistivity. Also, the error rise up to 40% for part of the data. This uncertainty of the model is non negligible as it will further add to the uncertainty of the inverse resistivity data.

This section showed that neither automatic fitting, neither analytical fitting were able to fit a Waxman-Smits model with realistic values of the parameters. Thus, the fitting describe here will not be used in the study. The appropriate fitting is described in SECTION 7.1.2, where the resistivity data and the saturation were normalised to take into account the heterogeneity of the formation factor and the effect of residual saturation.

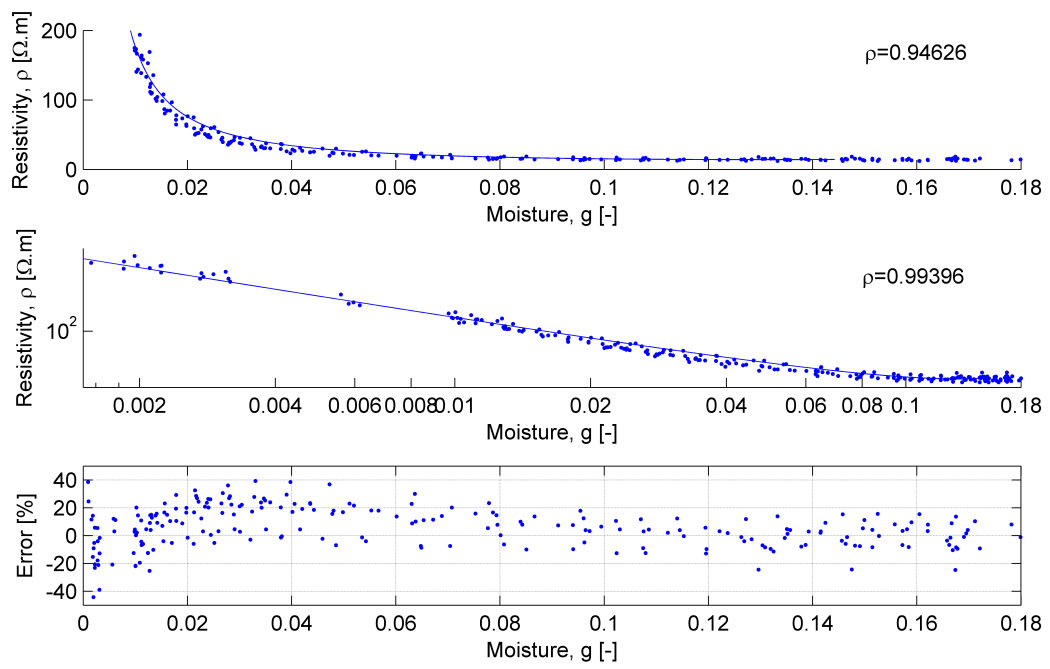


Figure 5.9: Waxman-Smiths model

Chapter 6

Field investigation

6.1 Data processing

Prior to the inversion, it is important to have a good understanding of the available data to make sure that the measurements are consistent. Also we need to process the data and remove the outliers to minimize the effect of bad data on the inversion. We pointed out (FIG. 6.1) that the number and the quality of the measurements per day was not constant and that it is important to select the data carefully in order to optimize the information we will return from the inversion.

We first present the raw electrical monitoring data and compared it to complementary data (temperature measurements, moisture probes, rainfall data) to make sure that the measurements are consistent with independent measures. Also, we showed that the analyses of the raw resistance data already gives an idea of the seasonality of the measurements, with a maximum resistivity reached in winter. Moreover, this raw resistance data were shown to be consistent with the infiltration data.

6.2 Electrical resistivity monitoring data

The geophysical data available for the Old Dalby landslide comprises daily measurement. The measuring sequence comprised conventional dipole-dipole measurements and each of the measurements was made in normal ρ_n and reciprocal configuration ρ_r , with the measured value ρ_m being defined as the mean of the normal.

Due to local conditions (e.g. bad electrode contact), measurements could not be performed every day. To make sure that the time-lapse data are comparable and to avoid inversion artefacts (e.g. temporal aliasing), a subset of resistivity data was selected every N days (FIG. 6.1). Also, to keep a sufficient time gap between the subsets and ensure that the selected subset comprised sufficient measurements, every subset was selected the day of the first n days ($n < N$) for which the number of measurements was maximal.

Despite this processing, there were still a few period of time that could not be represented through the inversion due to extended period where the monitoring system could not register any measurements.

6.2.1 Number of measurements vs. time

At FIG. 6.1 we can see that some days do not contain any measurements. Especially we can see that a lot of days are lacking measurements in winter 2015 and that in summer 2016 the number of measurements is more sparse, which is likely to be caused by bad electrode contact because of dry clay at the surface.

We also see that despite the selection of data every 7 days, there is still some periods where no data is available due to extended periods without measurements. Especially, we see that the line 2,

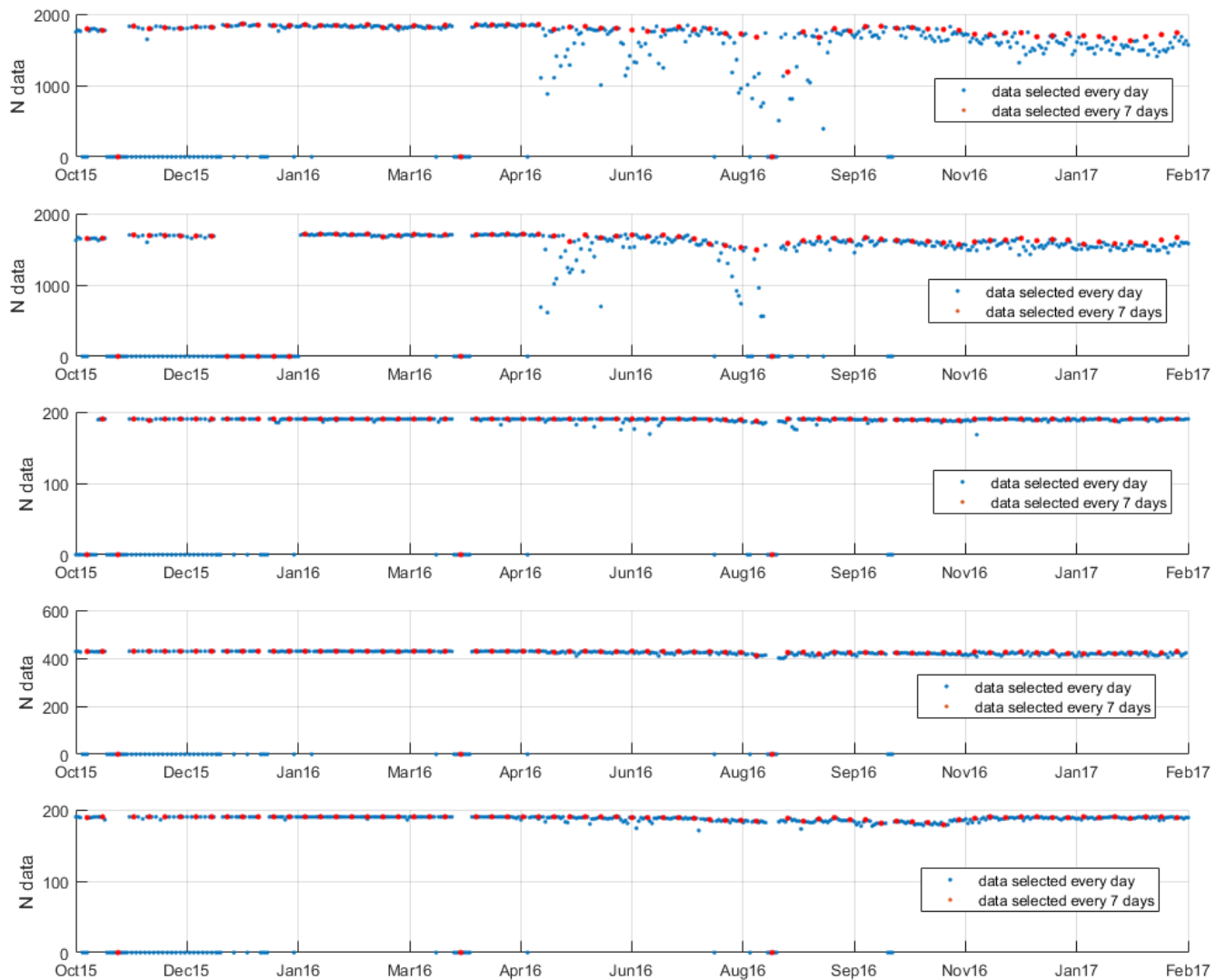


Figure 6.1: Number of data per day and per selected subset, line 1 to 5 from top to bottom

has an extended period without measurements in January. Apart from this problem with the line 2 and three small periods with no measurements in November 2015, April 2016 and August 2016, the rest of the subsets have a stable amount of measurements. This is the first step of the measurement selection and the outliers still have to be removed.

6.2.2 Resistance vs. time

6.2.2.1 Outliers

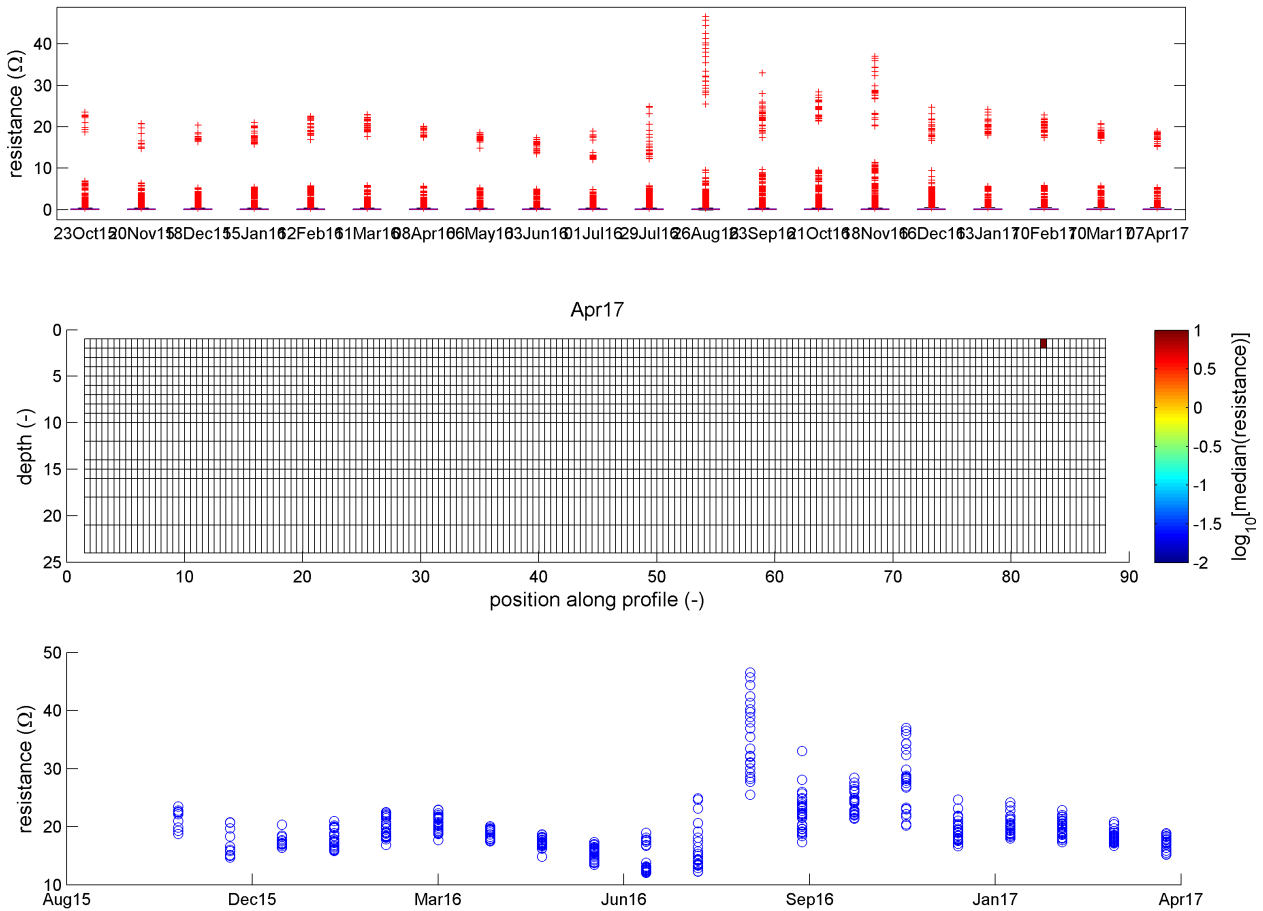


Figure 6.2: Outliers in line 1

We see in FIG. 6.2 that the data from line 1 has a subset of points for which the resistance is very high. The second subplot of FIG. 6.2 shows that this group of points is due to one particular electrode configuration. Thus, these points are considered as outliers and will be removed from the dataset prior to the inversion. Considering the graph (FIG. 6.2), all the measurements for which the apparent resistivity exceeds $12 \Omega.m$ will be deleted.

For line 2 (FIG. 6.3), we observe measurements with very high values of the resistance (FIG. 6.3, subplot 1). These measurements are non realistic and will be removed from the dataset. Also, starting in July 2016, we start measuring negative resistances (FIG. 6.3, subplot 3). Those measurements could be located to the "left" part of the profile: the position on the pseudosection for every negative resistance measurements is shown at the second subplot of FIGURE. 6.3. No investigation were done to explain the origin of those negative measurements. Hence, these negative measurements are considered as outliers and are removed prior to the inversion.

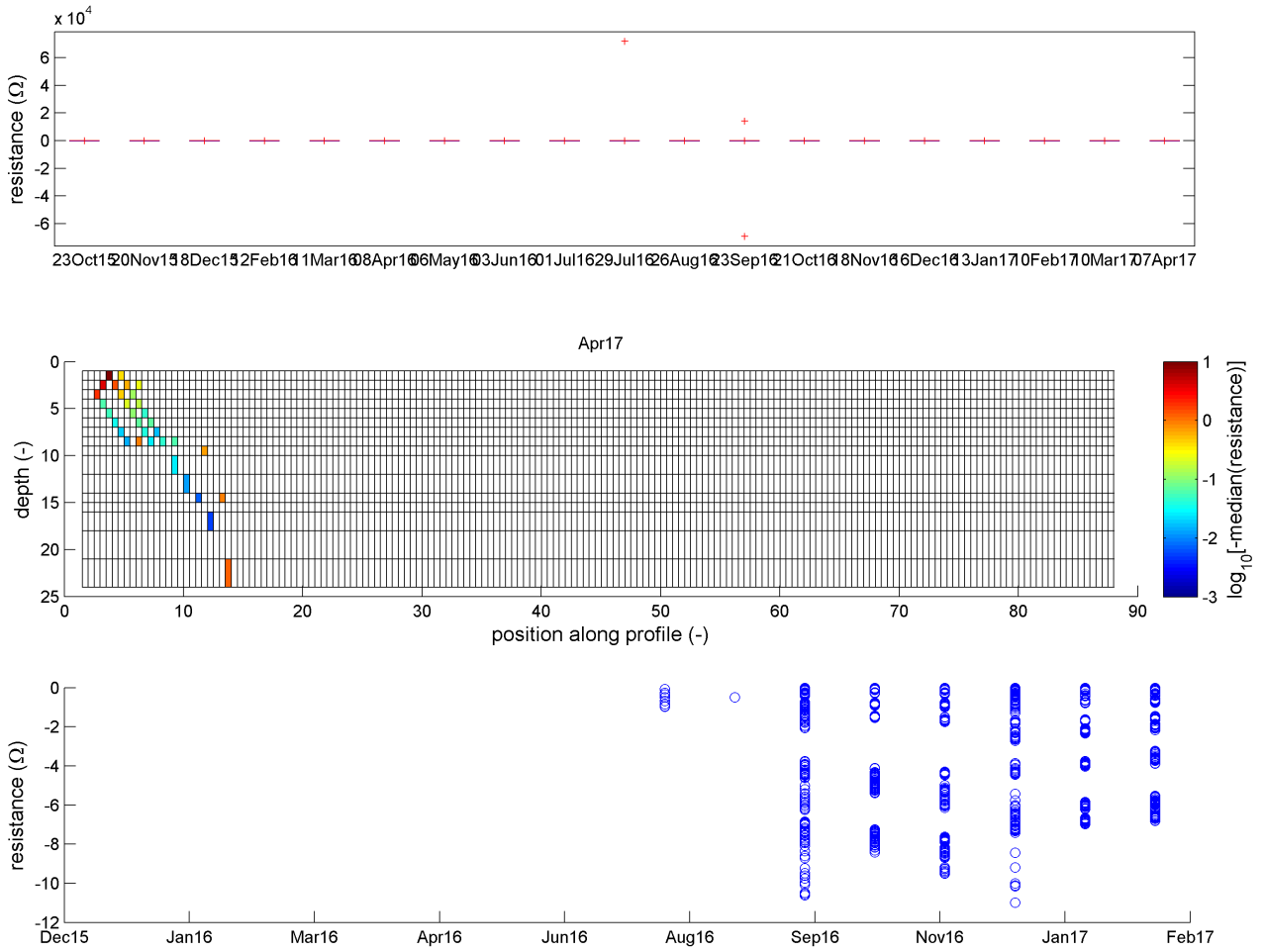


Figure 6.3: Negative data in line 2

6.2.2.2 Seasonality of the resistance

Once the outliers have been removed, we can look more precisely to the behaviour of the resistance over time (FIG. 6.4). First of all we see that there is a strong seasonality within the measurements. The seasonality is clearly seen when we analyse the behaviour of the maximum measured resistance through time, but it is also noticeable when we analyse the trend of the median or whatever statistical percentile.

Looking at the plot relative to line 1 and line 4 (subplot n°1 & n°4, Fig. 6.4), we see that the seasonality is much less marked for these profiles. The line 1 is located below the slope along the railway and the line 4 is located perpendicular to the railway over the relict landslide (FIG. 4.1). The reduced seasonality effect might be linked to a different dynamic of the groundwater under the relict landslide and below the slope. Those two lines are located in areas with less vegetation, where the evapotranspiration and the runoff are different from the other lines. Those differences affect the infiltration, thus having an impact on the dynamic of the groundwater and should explain the lowered seasonality effect.

6.2.3 Data error analysis

The relative error was calculated by dividing the absolute error by the measured resistance. The dependence of the error on the resistance and on the period of the year was studied (FIG. 6.5). For each line we observe a logarithmic decrease of the relative error with increasing resistance. The minimum of the relative error is generally in the vicinity of $10^0 \Omega$ and tends to increase again beyond this threshold. Also we observed that for similar resistance, the relative error tends to be higher in summer: the error is rather constant in winter, then starts to rise in May, before decreasing again at the beginning of October.

6.3 Rainfall and air temperature monitoring

Rainfall and air temperature were logged on site using a Vaisala weather station located on top of the railway cutting (FIG. 4.1). The air temperature measurements were used to estimate the daily evapotranspiration on site with the software Hydrus1D. The effective rainfall or infiltration was then determined by subtracting daily evapotranspiration from daily precipitation (FIG. 6.6). To make the reading of the infiltration chart easier, the cumulative infiltration was calculated. For every date, the cumulative infiltration corresponds to the total infiltration since the first measurement. Thus, it corresponds to the integral of the infiltration over time. We will see that the cumulative infiltration is particularly convenient in ground moisture studies as it correlates very well with the resistivity and the moisture data.

6.4 5TE monitoring

The moisture content (FIG. 6.7), the temperature and the conductivity were logged on site with 5TE moisture sensors. The measurements were made in three different areas and at different depth. The following labels were used to design those three areas:

- “Old Dalby” is a sensor cluster located on top of the railway cutting, it contains the weather data and two moisture sensors located at 0.1 m and 1.5 m depth. Data monitoring starts in February 2015.
- “Woods” is a sensor cluster located in the vegetated area surrounding the relict landslide. It contains five moisture sensors logging the VMC, the temperature and the conductivity of the subsoil. Data monitoring starts in August 2016.

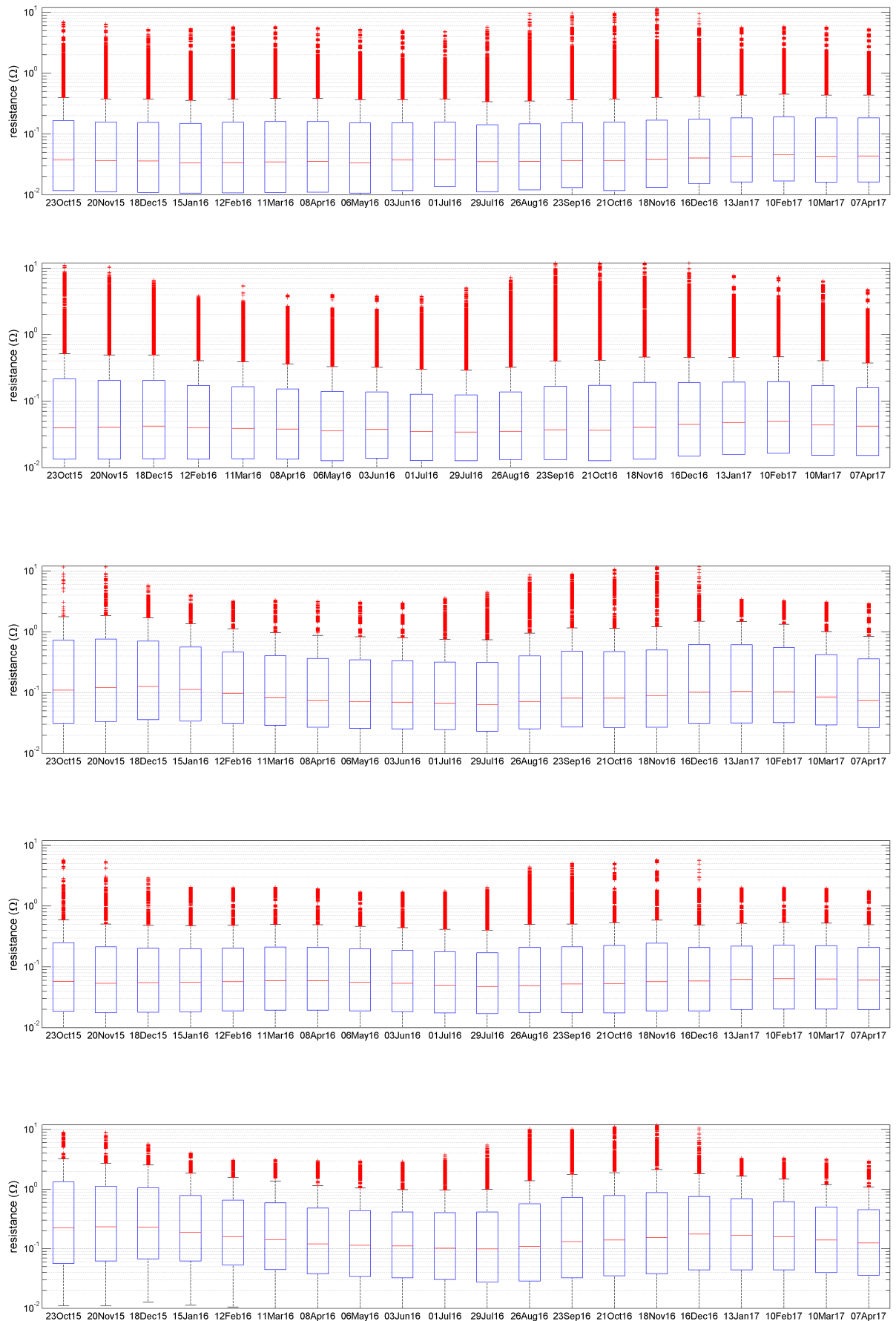


Figure 6.4: Resistance versus time (respectively line 1 to 5 from the top to the bottom)

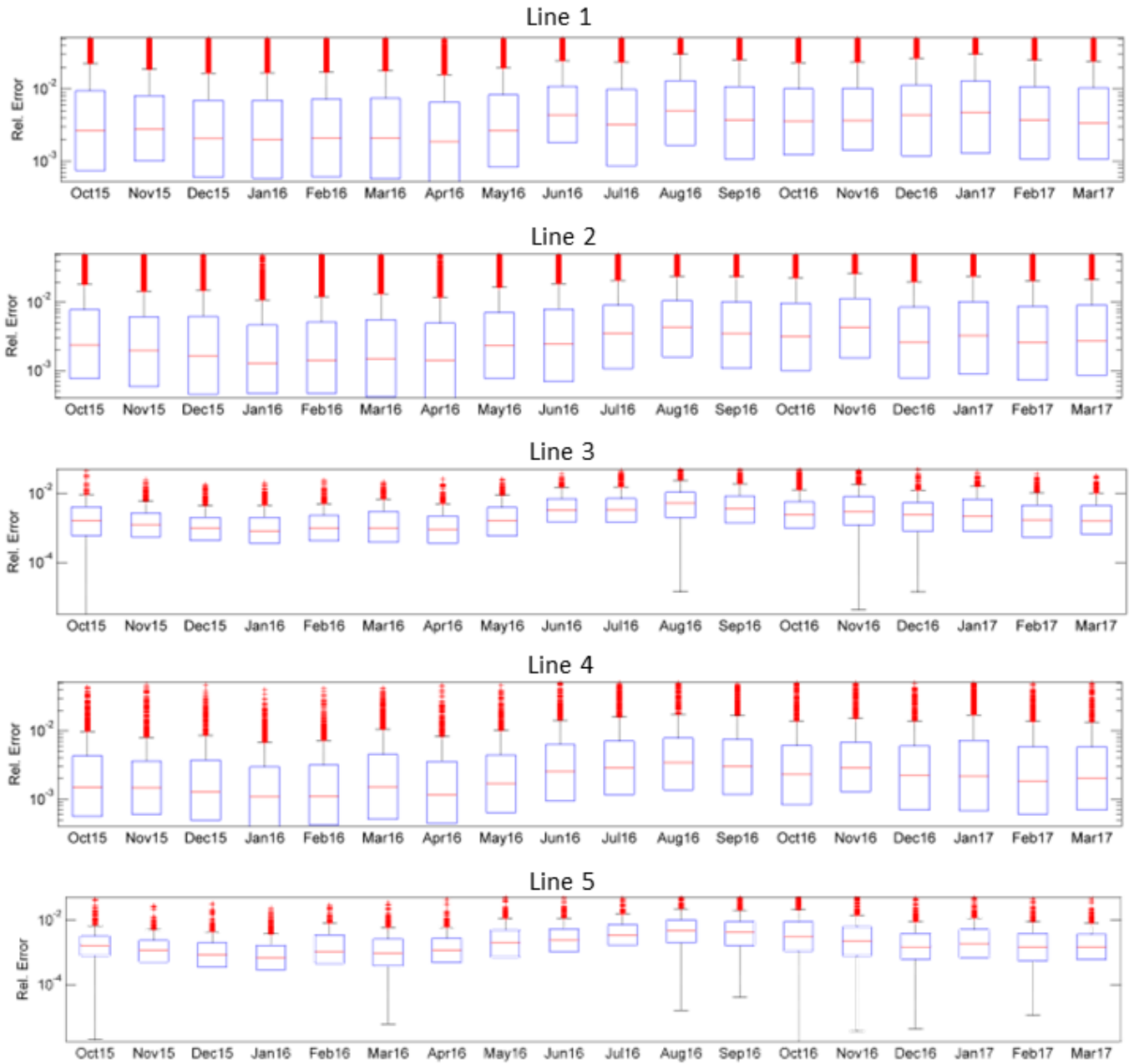


Figure 6.5: Relative error versus time

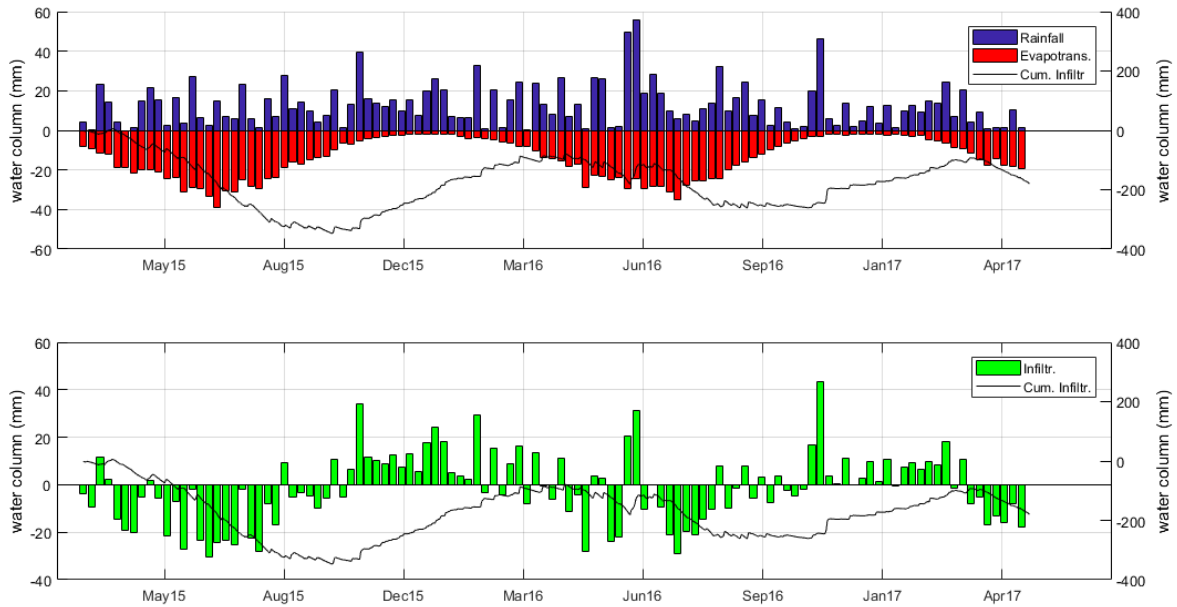


Figure 6.6: Comparison between rainfall, evapotranspiration and infiltration data

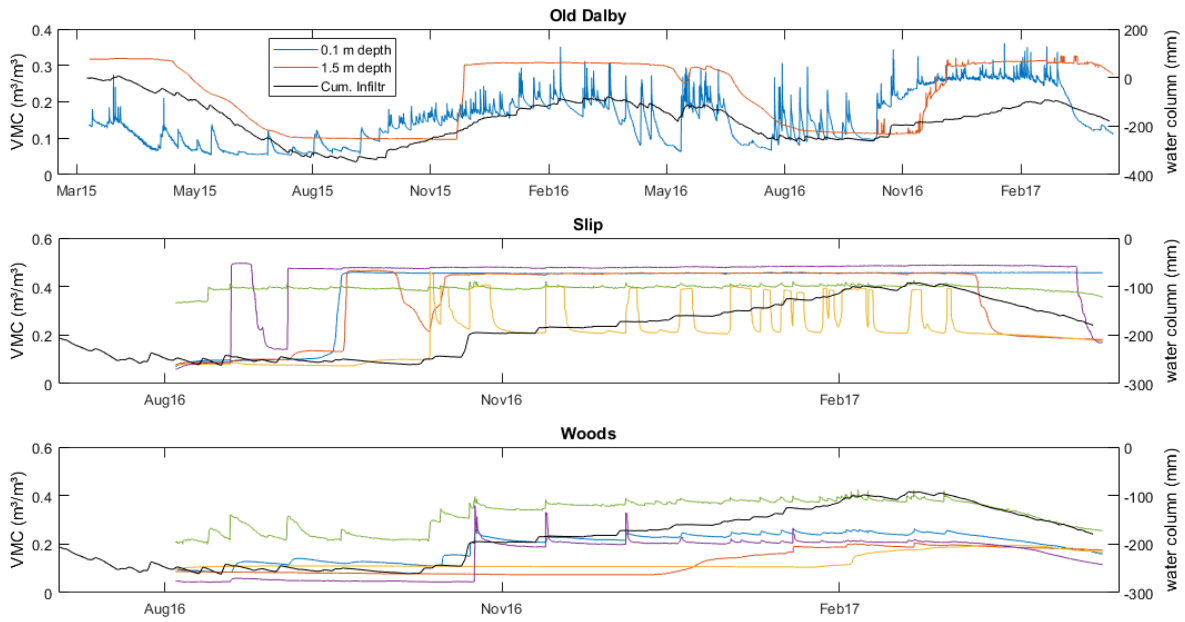


Figure 6.7: Comparison between cumulative infiltration data and in-situ 5TE moisture sensors

- "Slip" is a sensor cluster located within the Old Dalby landslide. It contains five moisture sensors logging the VMC, the temperature and the conductivity of the subsoil. Data monitoring starts in August 2016.

The 5TE conductivity measurements are based on 2-points measurements, thus being affected by contact resistance. This makes the 5TE measurements less reliable, especially at low moisture content where the contact resistance is maximal. Thus large contact resistance can lead to an overestimation of the soil resistivity (Hen-Jones et al., 2017). Even if 5TE sensors are less reliable than the 4-points measurements driven in the laboratory, they remain a useful complementary tool as they measure in-situ subsoil properties in real-time.

The temperature measurements are used to correct the temperature effect on resistivity, which is automatically corrected by the 5TE sensor (Decagon Inc., 2015).

Sensor ID	Sensor Type	Distance from top electrode [m]	Depth [m]	Backfill	EM50 Port
Cluster 1 - Next to Line 5 - "Woods"					
N1-1	5TE	8	0.5	0.1 m in-situ 0.4 m bentonite	1
N1-2	5TE	7.6	1.1	0.1 m in-situ 1.0 m bentonite	2
N1-3	5TE	3.75	2.45	0.1 m in-situ 2.35 m bentonite	3
N1-4	5TE	3.75	0.55	0.1 m in-situ 0.45 m bentonite	4
N1-5	GS3	6	0.15	backfilled with in-situ material	5
Cluster 2 - Next to Line 4 - "Slip"					
N2-1	5TE	10.3	0.82	0.1 m in-situ 0.72 m bentonite	1
N2-2	5TE	13.8	0.85	0.1 m in-situ 0.75 m bentonite	2
N2-3	5TE	15.8	0.68	0.1 m in-situ 0.58 m bentonite	3
N2-4	5TE	12.9	1.5	0.1 m in-situ 1.4 m bentonite	4
N2-5	GS3	12.6	0.15	backfilled with in-situ material	5

Table 6.1: Characteristics of "Woods" and "Slip" 5TE clusters

The effect of the resistivity temperature correction is shown on the Old Dalby 1.5 m depth sensor at Fig. 6.8.

6.4.1 Temperature modelling

Decagon RT1 multi-level temperature probes were used to monitor the seasonal temperature changes in the subsurface. This information is used to correct the temperature effects influencing the time-lapse ERT images. Equation 3.7.30 allows to model the seasonal temperature changes in the subsurface:

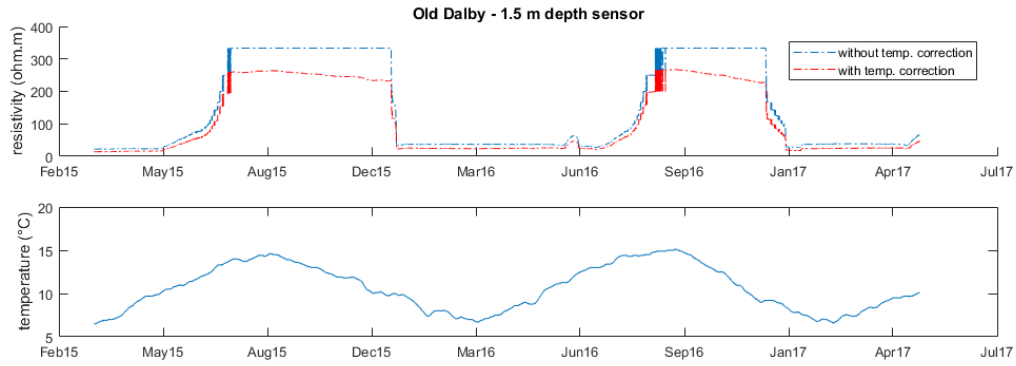


Figure 6.8: Effect of temperature correction on resistivity data

$$T(z, t) = T_{mean} + \frac{\Delta T}{2} e^{-(z/d)} \sin\left(\frac{2\pi}{365}t + \phi - \frac{z}{d}\right) \quad (6.4.1)$$

The parameters of the model were fitted so that they minimize the root mean square of the difference between the calculated model and the measurements. The solution of the problem was solved in Python using the `scipy.optimize.fmin` function. It uses a non linear optimization algorithm, the Nelder-Mead simplex algorithm, to find the minimum of a function of one or more variables. This algorithm is appropriate for non linear optimization problems for which derivatives may not be known. The initial model was set to $[T_{mean}, \Delta T, d, \phi] = [10 \text{ }^\circ\text{C}, 14^\circ\text{C}, 2 \text{ m}, -2]$ and converged to the solution showed at Table. 6.2

T_{mean} ($^\circ\text{C}$)	ΔT ($^\circ\text{C}$)	d (m)	ϕ (-)
10.631	13.183	2.748	-1.914

Table 6.2: Parameters fitted for the temperature model

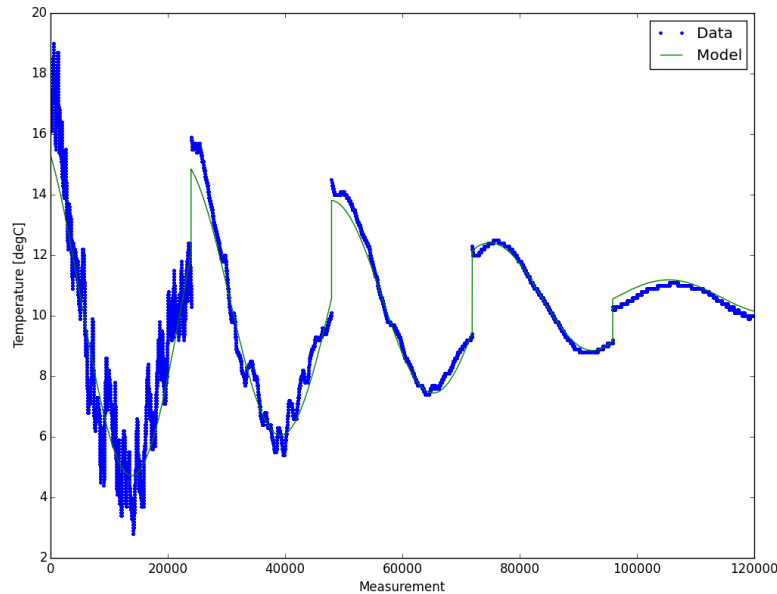


Figure 6.9: Temperature model of the Old Dalby subsoil

6.5 Effect of water infiltration on 5TE based soil moisture

At FIG. 6.10, 6.11 & 6.12, we investigate the relationship between water infiltration in the subsoil and the volumetric moisture content logged by the 5TE sensors. We see that the 5TE moisture measurements correlates very well with the cumulative infiltration curve especially for the sensors located in the woods. Also, we see that the spikes observed on the VMC measurements are representative of the infiltration episodes as they correlates in time with the episodic rises observed in the infiltration curve. Furthermore, we observe that these VMC episodic spikes are particularly present for the sensors located close to the surface and tends to be attenuated and delayed at higher depths. This naturally indicates that the parts of the subsoil closer to the surface are more reactive to infiltration episodes as they show shorter period moisture dynamic. Also, the graphs from FIG. 6.10, 6.11 & 6.12 show that the whole system is connected as the sensors buried deeper in the subsoil reacts in accordance with the sensors buried at lower depth but with a certain delay. We also observe that the range of moisture content logged by the 5TE sensors is comprised between 10% and 45% volumetric moisture content but that the local order of magnitude of the moisture variation varies with the position of the sensors, hence indicating that the dynamic of the system is not homogeneous.

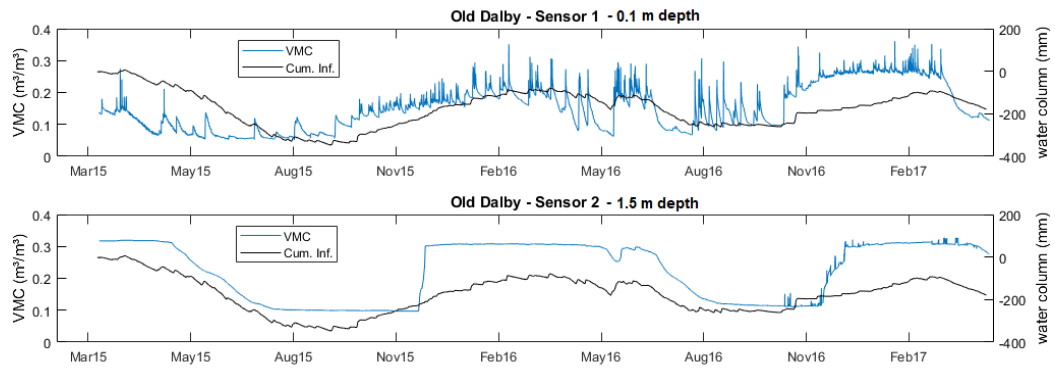


Figure 6.10: Comparison between the 5TE moisture content measurements and the effective infiltration calculated from the weather monitoring

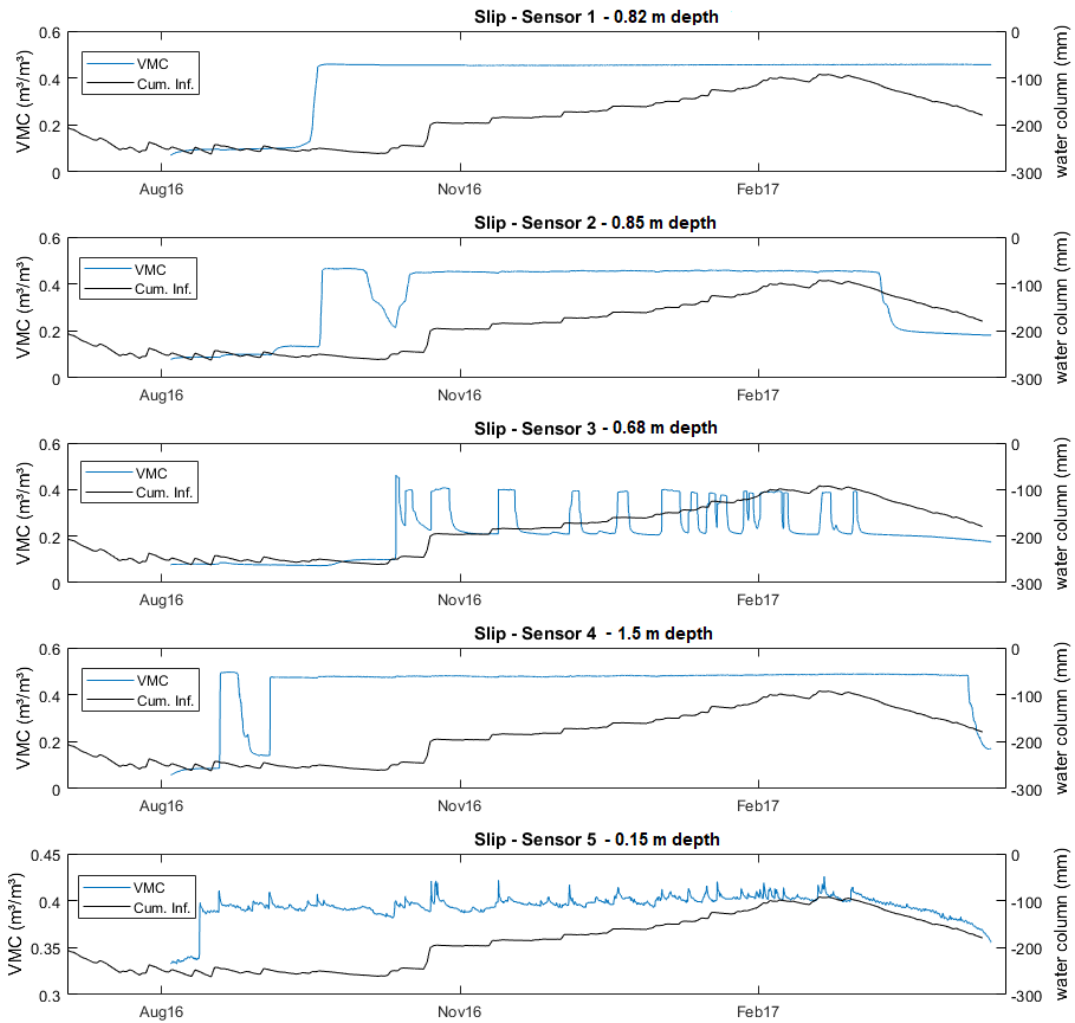


Figure 6.11: Comparison between the 5TE moisture content measurements and the effective infiltration calculated from the weather monitoring

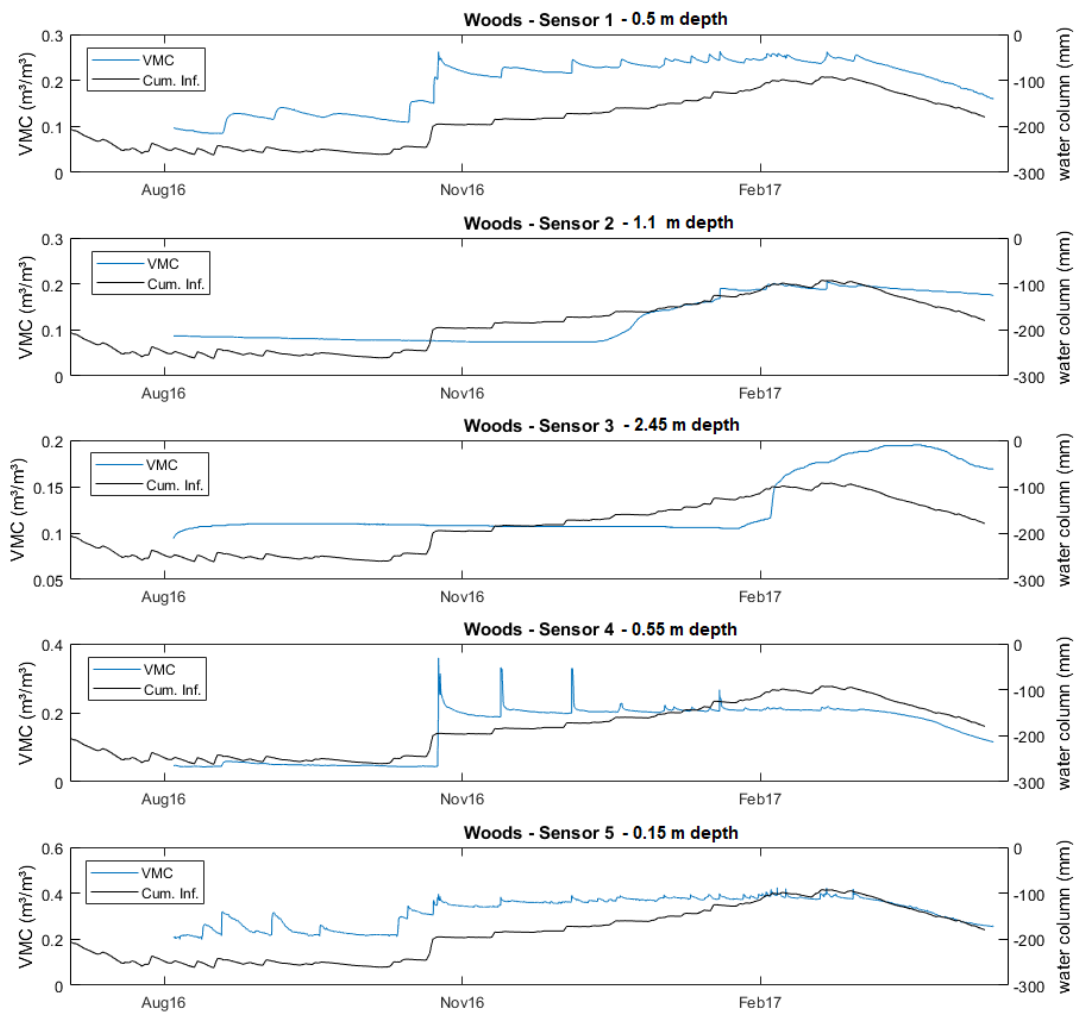


Figure 6.12: Comparison between the 5TE moisture content measurements and the effective infiltration calculated from the weather monitoring

6.6 Reliability of 5TE based VMC/resistivity measurements for Waxman-Smits model fitting

In this section we will focus on the resistivity behaviour relative to the VMC variations to see how good is the correlation and if the resistivity measurements are affected by noise. Especially considering that one of the issues with the 5TE resistivity measurements is that they are affected by the contact resistance because the resistivity is based on 2-point measurements. The 2-point measurements makes the results less reliable, which have been discussed by Hen-Jones et al. (2017) where they showed that the contact resistance was more present at high values of resistivity (low VMC). Nevertheless, in his study, Hen-Jones et al. (2017) showed that, at least at high moisture content, the 5TE in-situ measurements were close to the four-points measurements (see FIG. 6.13). Thus the bad quality of two points measurements observed in laboratory would be attenuated in-situ. This was attributed to very low contact resistances due to good soil-sensor contact resulting from the sensors being embedded at depth and to low in-situ anisotropy.

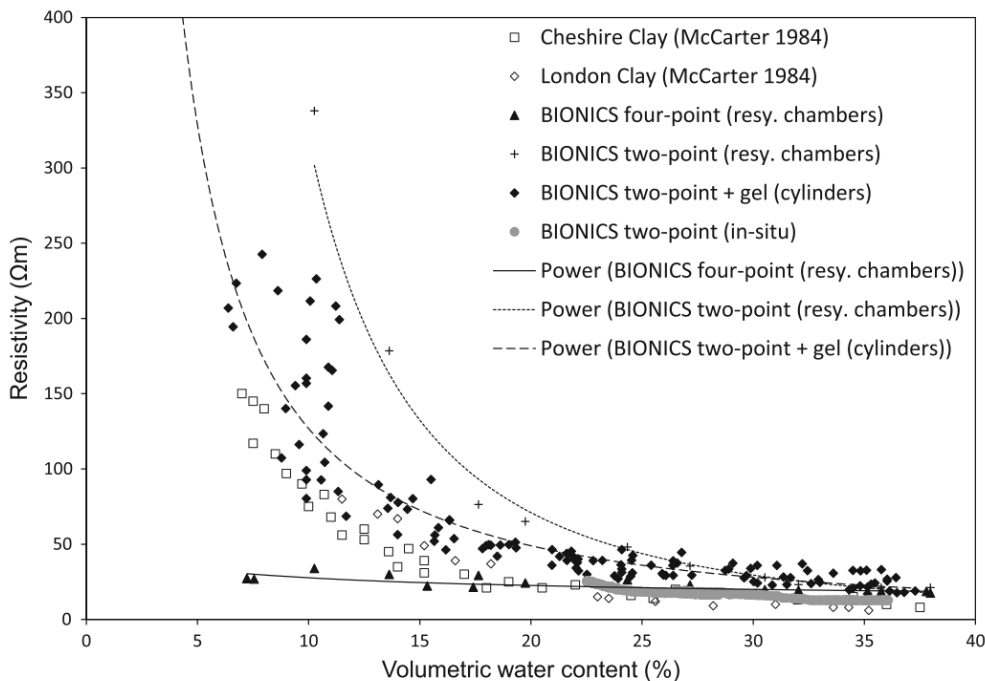


Figure 6.13: Water content-resistivity relationship (from Hen-Jones et al., 2017)

Especially, considering the great correlation between the infiltration, the moisture content and the resistivity measurements (FIGS. 6.14 & 6.15 & 6.16), it is legitimate to assess that the measured resistivity are representative of the subsoil. We can also investigate the error on the 5TE resistivity data: for every set of resistivity measurements in a given VWC range, we calculated the 1st, the 5th, the 50th, the 95th and the 99th percentile of the resistivity measurement (FIG. 6.17). We see that the data from the "slip" cluster is very well distributed, whereas the data from the cluster "woods" shows higher order of variations, especially for the sensor located at 0.55 m depth. For the cluster "Old Dalby" we see that the data is still very well distributed but that the resistivity values for a given VWC varies much more. Considering that the "Old Dalby" cluster contains data from 2 years of monitoring it is logical to see such variations in the resistivity distribution as the hysteresis between the loading and the unloading can have a significant effect on the resistivity measurements.

FIG. 6.17 shows that the way the resistivity changes in response to the VMC variations of the medium can vary a lot depending on the location in the subsoil. Thus applying one unique Waxman-

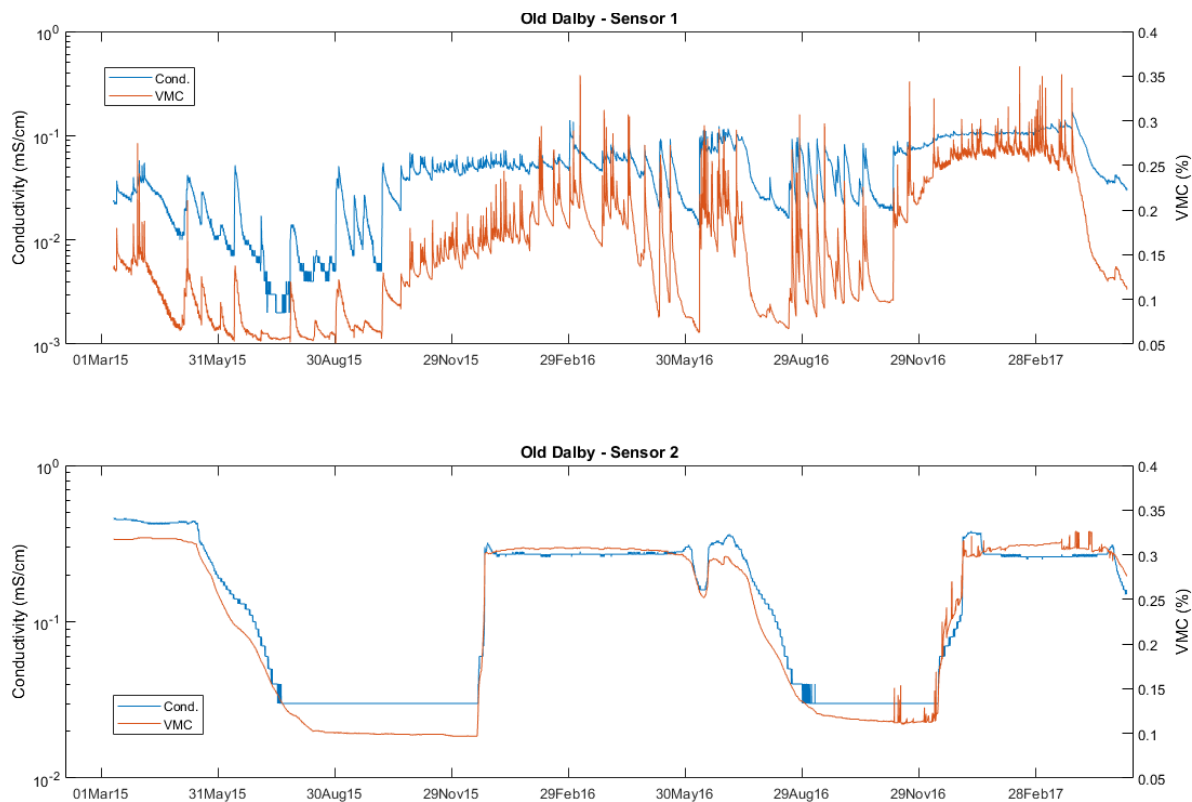


Figure 6.14: Comparison between the conductivity and the moisture measurement of the 5TE. Moisture and conductivity are evaluated with independent measurement methods.

Smits model to the whole system seems inadequate. If we now compare the laboratory resistivity-moisture measurements with the in-situ 5TE measurements (FIG. 6.17), we see that, except for the "slip" cluster and one of the sensor in the "woods", for a given moisture content the 5TE resistivity measurements are systematically higher than the laboratory measurements. Interestingly, we see that the data from the "Slip" cluster shows a trend very similar to that of the laboratory data, even if at high moisture we observe a behaviour not replicated in laboratory. This similitude in the measurements could be due to a good soil-sensor contact associated to poorly altered clay and could indicate that when similar conditions are met, the 5TE measurements are representative of resistivity behaviour relative to moisture content variations.

At low moisture content, we see that some of the sensors shows resistivity significantly higher than the others. Considering that the soil-sensor contact is good at low moisture content, such high resistivity values might not only be due to high contact resistance and could indicate that the laboratory relation is not applicable to the whole system. In this way, I decided to normalize the resistivity and the saturation in the Waxman-Smits model to take into account the formation factor heterogeneity and the effect of residual water saturation. The 5TE based VMC/resistivity measurements were selected and added to the laboratory measurements to broaden the dataset and check if the normalization was justified.

6.7 Normalization of the Waxman-Smits model

6.7.1 Resistivity normalization

As said previously, the 5TE sensors indicate that the subsoil resistivity at saturation is not constant over the whole study site. Thus the formation factor F of the Waxman-Smits equation will have a

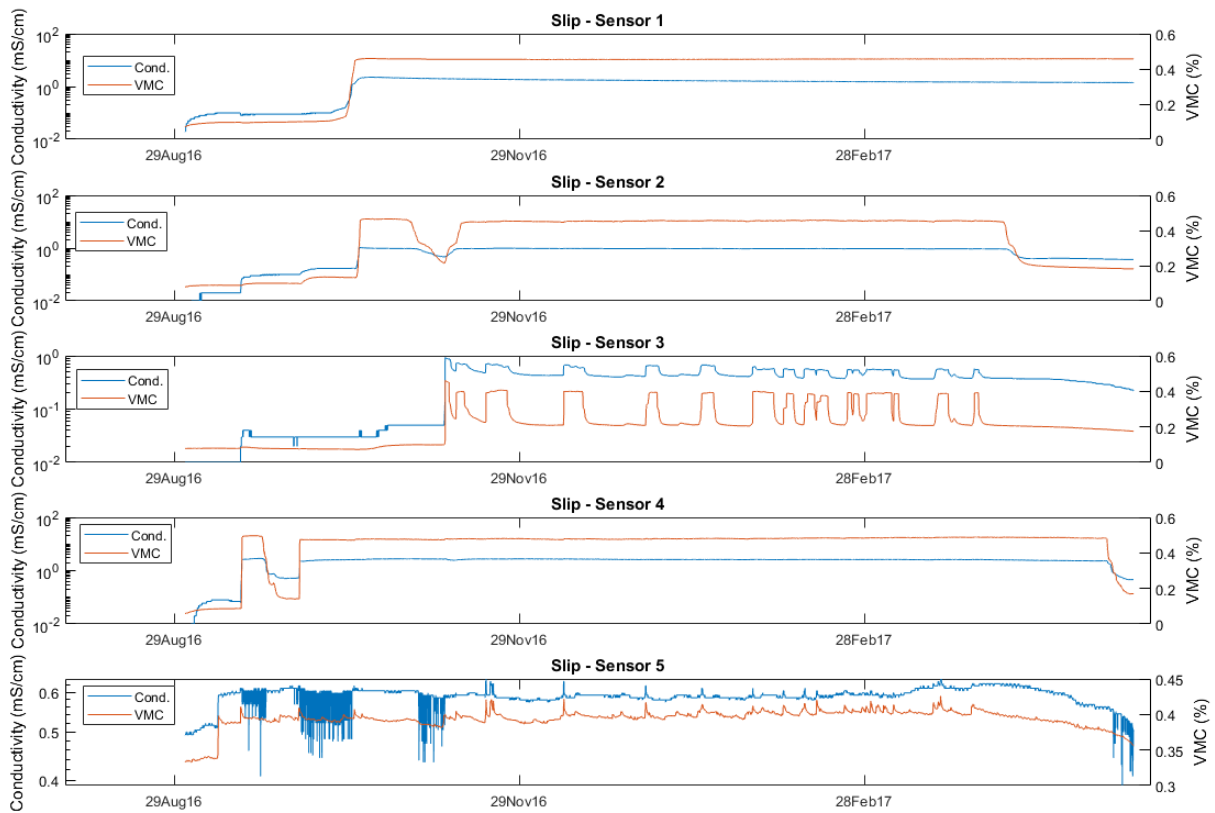


Figure 6.15: Comparison between the conductivity and the moisture measurement of the 5TE. Moisture and conductivity are evaluated with independent measurement methods.

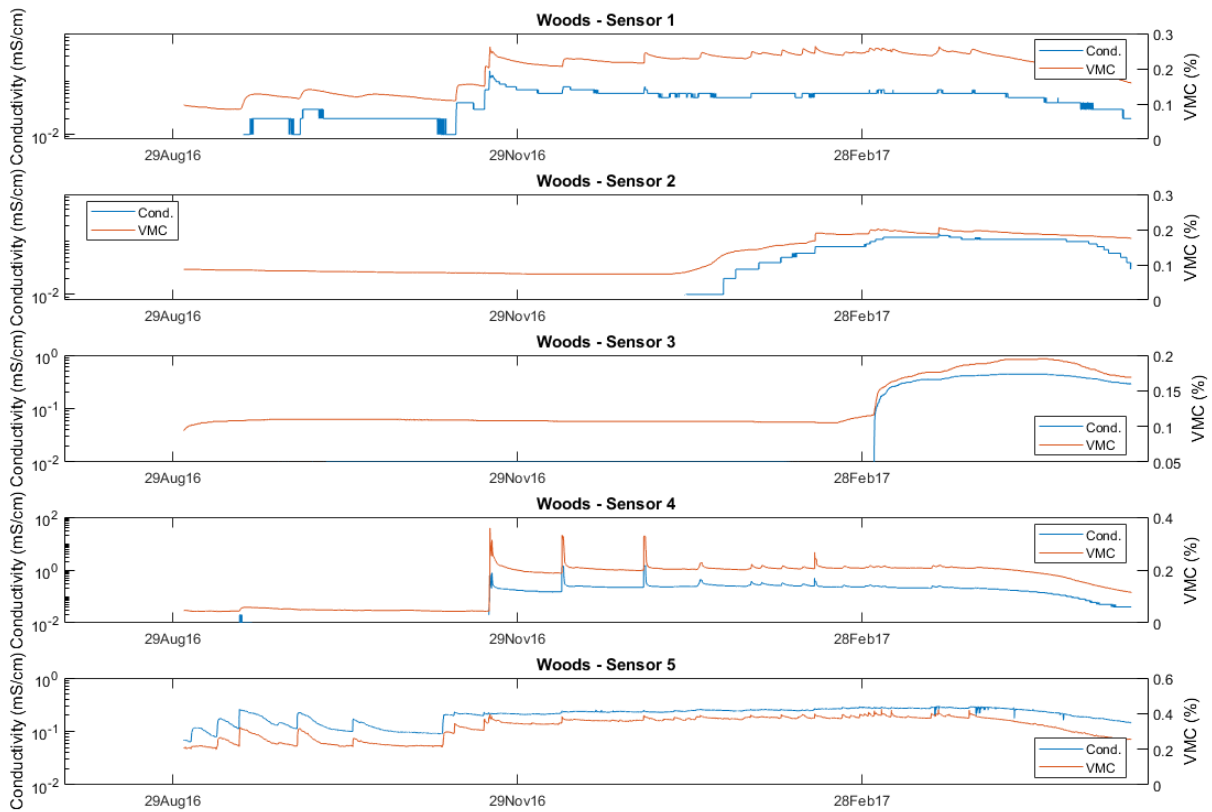


Figure 6.16: Comparison between the conductivity and the moisture measurement of the 5TE. Moisture and conductivity are evaluated with independent measurement methods.

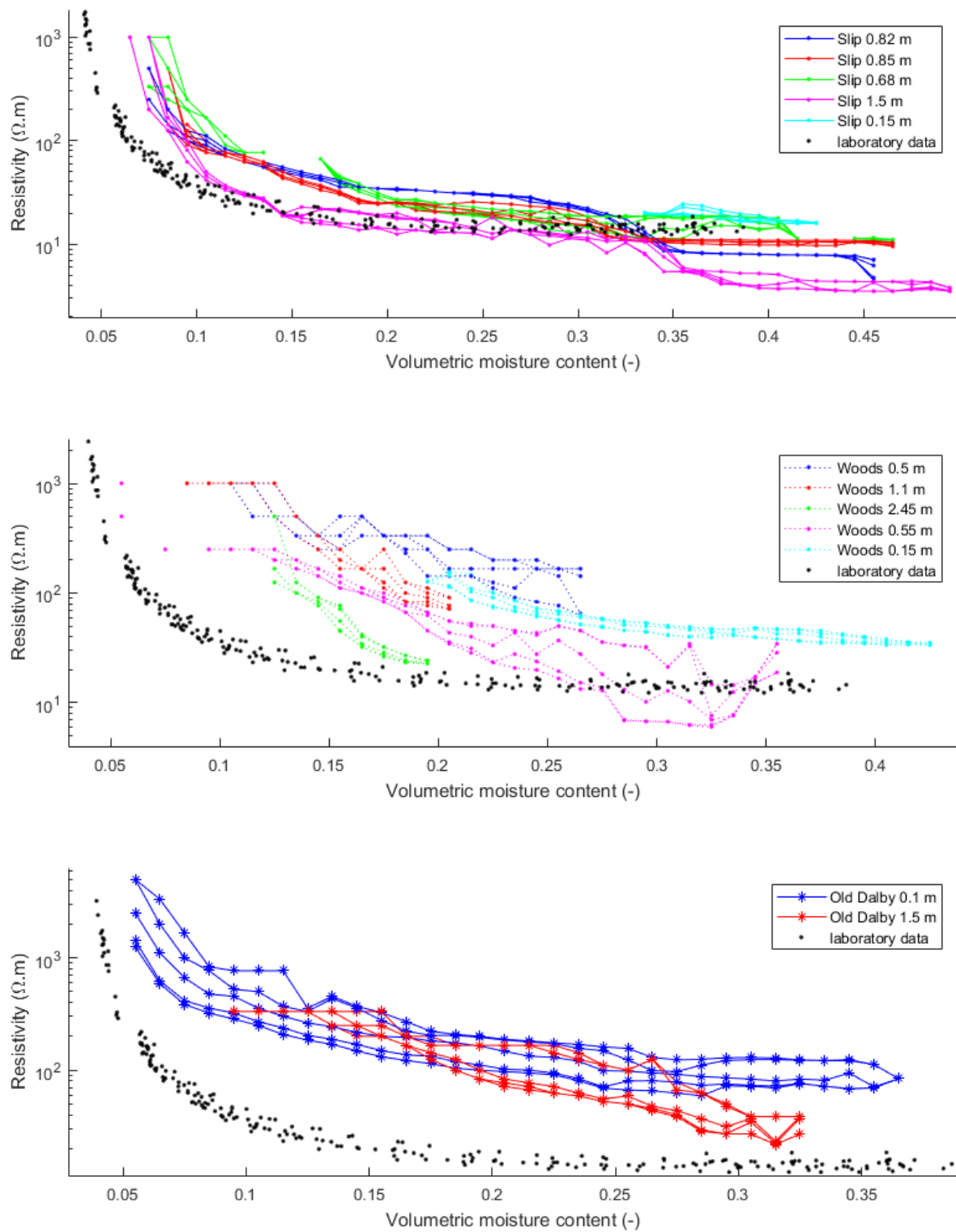


Figure 6.17: Error on the resistivity measurement. For each sensor the 1st, the 5th, the 50th, the 95th and the 99th percentile of the resistivity measurement is shown.

significant impact on the moisture imaging. If we are able to image the saturated resistivity, ρ_{sat} , of the subsoil, it would be possible to get rid of this effect. In fact, the resistivity ratio $I = \rho_0/\rho_{sat}$ is independent of the formation factor F since (Waxman and Smits, 1968)

$$I = S^{1-n} \left(\frac{1 + \rho_w \cdot \sigma_{e,sat}}{S + \rho_w \cdot \sigma_{e,sat}} \right) \quad (6.7.1)$$

Considering that the monitoring data extends over a 1.5 years period, that the depth of the study site is relatively low (< 10 m) and that the climatic conditions in the UK are ideal for water infiltration (high precipitations, low temperatures), the assumption that every volume of the subsoil monitored by the electrical resistivity tomography reaches full saturation over this 1.5 years period seems reasonable. From this assumption, it is possible to calculate the saturated resistivity of the subsoil for each cell of the inversion grid (FIG. 6.18).

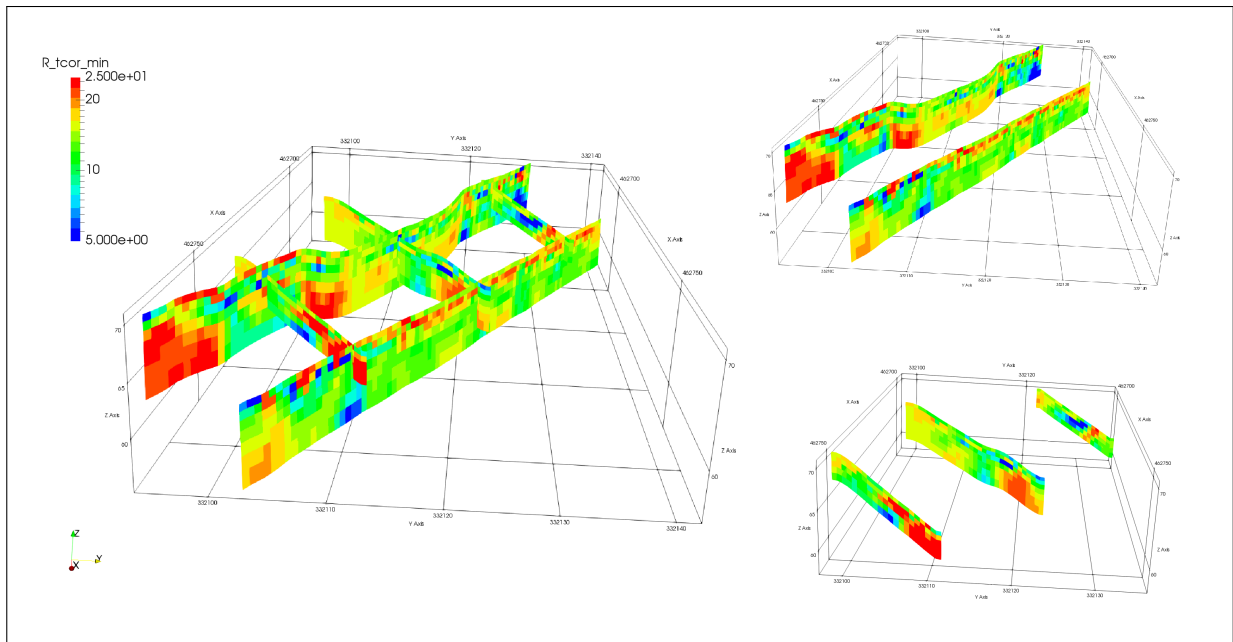


Figure 6.18: Minimum resistivity observed for each cells (expressed in $\Omega.m$). The minimum observed resistivity is supposed to be close to the saturated resistivity

We observe at FIG. 6.18 that the minimum resistivity is not constant over the study site and that it varies between $2.11 \Omega.m$ and $43.35 \Omega.m$ (TABLE 6.3). Hence both the 5TE measurements and the electrical resistivity tomography suggest that the subsoil's saturated resistivity is not homogeneous.

If we divide the resistivity value associated to each cell by its minimum resistivity, we can image the resistivity ratio I of the subsoil, which can be later converted into saturation using equation 6.7.1.

Table 6.3: Minimum and maximum values of the calculated saturation resistivity

Resistivity at saturation ($\Omega.m$)	Line 1	Line 2	Line 3	Line 4	Line 5
Minimum	2.1107	2.7586	3.3382	4.1903	4.9669
Maximum	43.3472	25.6429	23.0499	21.7154	34.057

The resistivity ratio I is calculated by dividing the measured resistivity by the minimum measured resistivity. Similarly, the saturation is evaluated by dividing the measured volumetric (resp. gravimetric) moisture content by the volumetric (resp. gravimetric) moisture content at which the minimum resistivity is observed. In this way we ensure that $I = 1$ for $S = 1$.

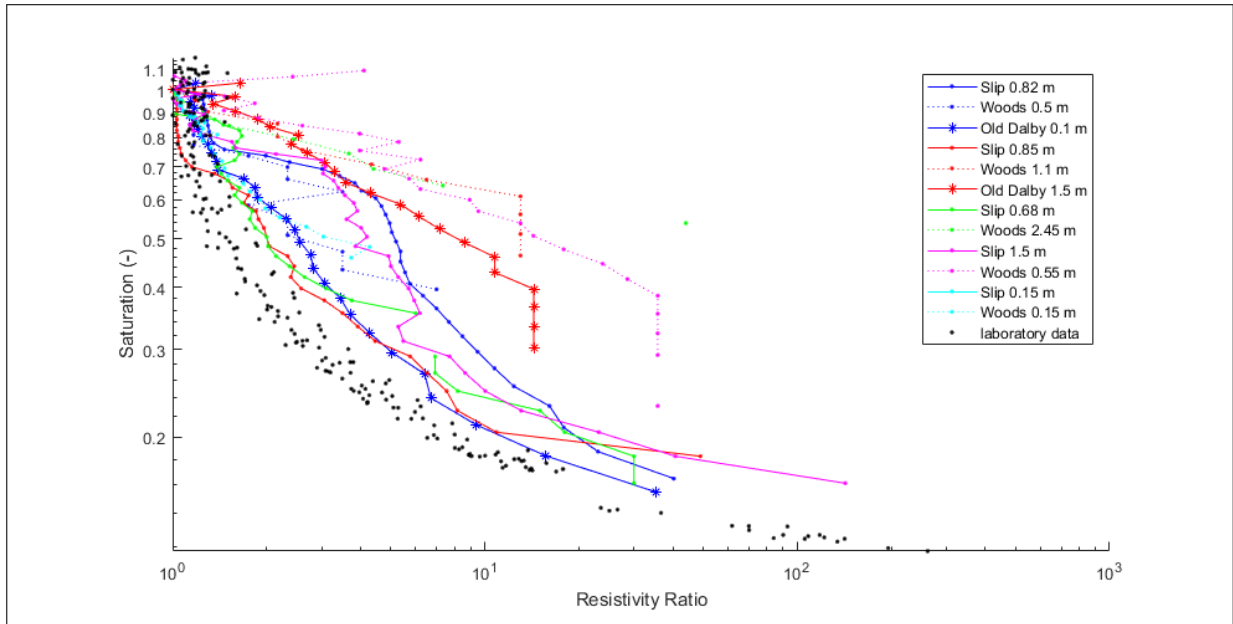


Figure 6.19: Waxman-Smits on resistivity ratio

6.7.2 Normalization of the saturation

If we plot the saturation S (estimated from the laboratory and the in-situ sensors) in function of the resistivity ratio I on a logarithmic scale (FIG. 6.19), we see that the data do not behaves how predicted by Waxman-Smits theory (Waxman and Smits, 1968). In fact, the resistivity tends to infinity for a saturation value higher than zero. This observation is not negligible as it will lead to poor fitting of the Waxman-Smits model coupled to unrealistic parameter values (see SECTION. 5.4). For this reason, I decided to modify the Waxman-Smits equation and to incorporate a parameter S_{lim} that enables to model the sharp resistivity rise that appears before that the medium is fully desaturated. This leads to the following equation:

$$I = \left(\frac{S - S_{lim}}{1 - S_{lim}} \right)^{1-n} \left(\frac{1 + \rho_w \cdot \sigma_{e,sat}}{\frac{S - S_{lim}}{1 - S_{lim}} + \rho_w \cdot \sigma_{e,sat}} \right) \quad (6.7.2)$$

The relation 6.7.2 is consistent with Waxman-Smits equation as we can retrieve equation 6.7.1 for $S_{lim} = 0$ and we still have $I = 1$ for $S = 1$ for every value of S_{lim} . This approach proved it efficiency by allowing much better results in terms of fitting.

6.8 Importance of residual water saturation in Waxman-Smits model

The parameters for the Waxman-Smits model were evaluated in SECTION 5.4. We showed in that section that the fitting of the model lead to unrealistic values of the parameters. For this reason I decided to add a parameter, S_{lim} , in the Waxman-Smits equation. This parameter models the residual water saturation and enables to explain the sharp resistivity rise observed before the sample being fully desaturated. The introduction of this parameter showed to greatly increase the quality of the fit while allowing realistic parameters of the model.

Indeed, we see at FIG. 6.20 that the curve delimited by the measurements does not follow Waxman-Smits theory (the points should tend to a finite resistivity at low moisture content or have a log-linear behaviour like the green curve in (FIG. 6.20)). Hence, the only way to fit the points

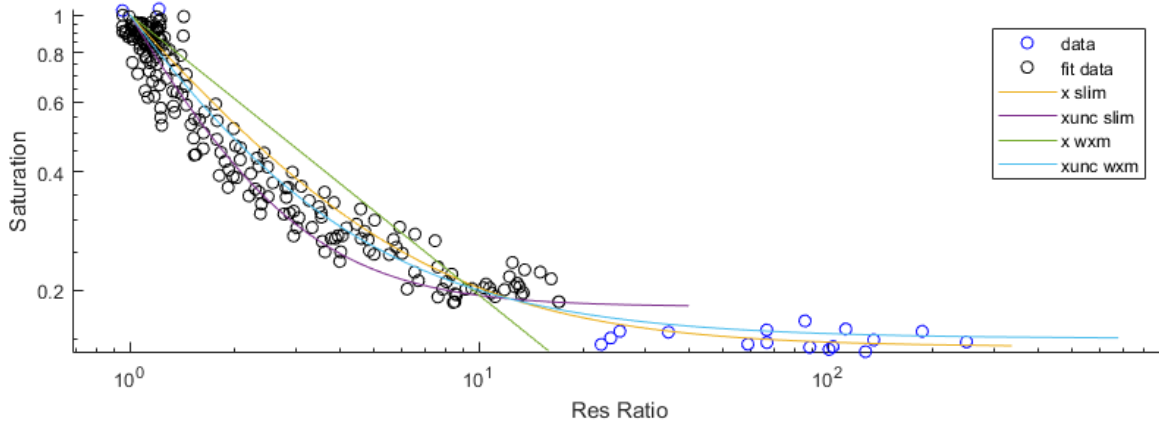


Figure 6.20: Effect of 2 different physical models and 2 different fitting methods. Here the models are fitted on the points in black ($S > 0.18$), for detailed results see TABLE. 6.4

Table 6.4: Results of the different fit of FIG. 6.20

Waxman-Smits	Starting model	X WXM	XUNC WXM	Fixed
n [-]	1	2.4039	0.6606	no
ρ_w [$\Omega.m$]	1	4607	-1.572	no
Q_v [eq/l]	1	1	1	yes
Iterations	0	34	16	no
Algorithm	-	<i>trust-region-reflective</i>	<i>quasi-newton</i>	yes
Mean relative error [%]	-	<i>27.14</i>	<i>15.25</i>	-
Waxman-Smits (modified)	Starting model	X SLIM	XUNC SLIM	Fixed
n [-]	1	1.8605	1.5487	no
ρ_w [$\Omega.m$]	100	100	100	yes
Q_v [eq/l]	1	1	1	yes
S_{lim} [-]	0	0.1432	0.1812	no
Iterations	0	27	14	no
Algorithm	-	<i>trust-region-reflective</i>	<i>quasi-newton</i>	yes
Mean relative error [%]	-	18.2	17.13	-

correctly is to allow negative surface conductivity, which is unrealistic and leads very small values for the saturation exponent (TABLE. 6.4).

At FIG. 6.20, we observe that the yellow curve is very satisfying in terms of fitting. Especially considering that it was fit on the points in black and that it predicts with precision the behaviour at lower saturation (blue points). This curve, and the purple one, were fitted using the modified Waxman-Smiths equation which includes the additional parameter S_{lim} . Looking at (TABLE 6.4), we see that the introduction of this parameter seems relevant as it reduces the mean absolute relative error and allows realistic values for the traditional parameters of the Waxman-Smiths equation (n , ρ_w , Q_v).

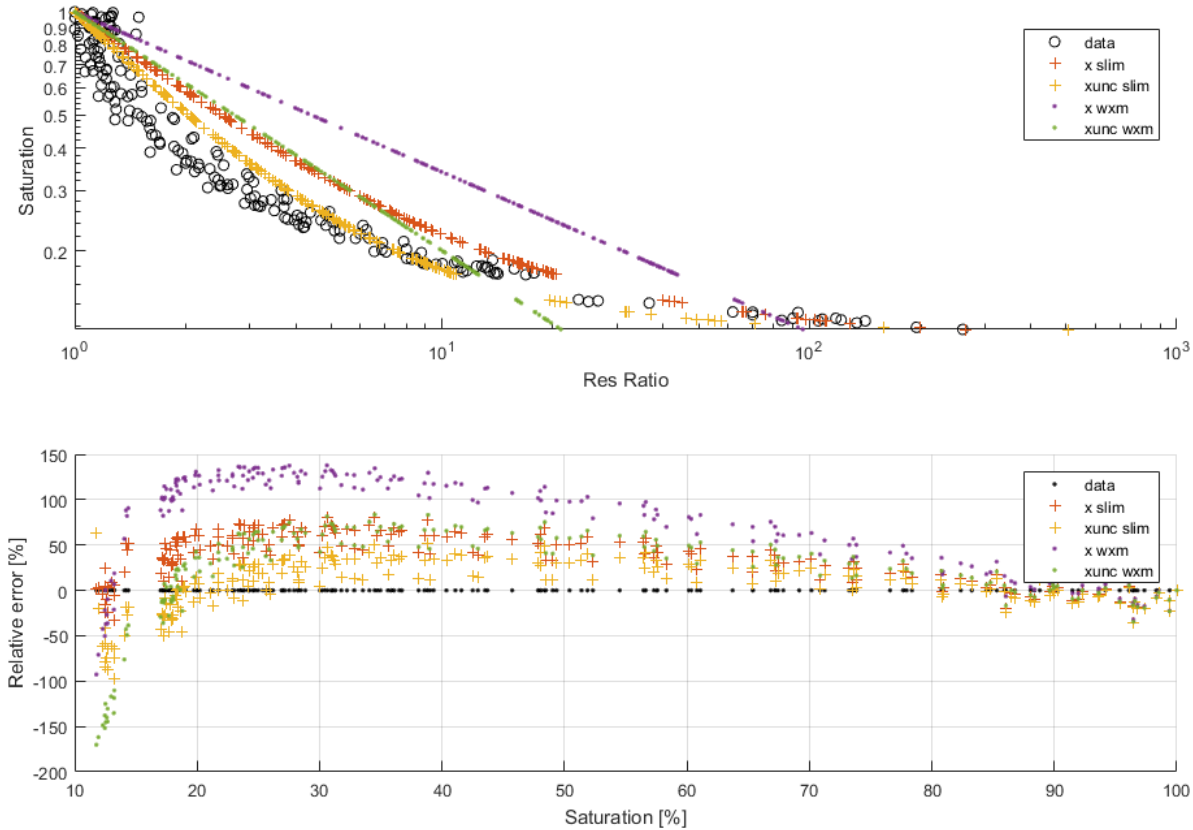


Figure 6.21: Comparison between 2 different physical models and 2 different fitting methods. Here the models are fitted on all the points, for results see FIG. 6.5

At FIG. 6.21 the fit is realised on the whole laboratory dataset. For both TABLE 6.4 & 6.5 the model 1 is computed using the non-linear data fitting MATLAB function *lsqcurvefit*, which solves the problem in a least-square sense. The model 2 is computed using the MATLAB function *fminunc*, this function allows to specify the algorithm used (here *Gauss-Newton*) and the function to minimize. In our case we can write the objective function to minimize:

$$\Phi(x) = \sum_i \left(\frac{F(x, xdata_i) - ydata_i}{F(x, xdata_i) + ydata_i} \right)^2 + \sum_j x_j^2 \quad (6.8.1)$$

Meaning that, as for the levenberg-marquart algorithm, we control both the direction and the magnitude of the model. As the parameters are not independent, this ensures that the fitting do not create unjustified high values of the model parameters.

Table 6.5: Results of the different fit of FIG. 6.21

Waxman-Smits	Starting model	X WXM	XUNC WXM	Fixed
n [-]	1	3.1332	1.4486	no
ρ_w [Ω .m]	1	25599	0.0016	no
Q_v [eq/l]	1	1	1	yes
Iterations	0	33	12	no
Algorithm	-	<i>trust-region-reflective</i>	<i>quasi-newton</i>	yes
Mean relative error [%]	-	<i>82.95</i>	<i>44.83</i>	-
Waxman-Smits (modified)	Starting model	X SLIM	XUNC SLIM	Fixed
n [-]	1	2.1061	1.8489	no
ρ_w [Ω .m]	100	100	100	yes
Q_v [eq/l]	1	1	1	yes
S_{lim} [-]	0	0.112	0.1172	no
Iterations	0	33	12	no
Algorithm	-	<i>trust-region-reflective</i>	<i>quasi-newton</i>	yes
Mean relative error [%]	-	38.9	23.42	-

6.9 Resistivity error model for weighted data fitting

We have shown that the error on the resistivity measurements increases with decreasing saturation. Hence, if we build a model of the standard deviation $\sigma_\rho(S)$ of our measurement, it could be used to weight the objective function.

Evaluating the standard deviation of the measurement for successive range of saturation values (FIG. 6.22), we see that the standard deviation follows an exponential law. We see at FIG. 6.22 that adding a corrective factor to the saturation

$$S_{corr} = \frac{S - 0.1}{1 - 0.1}$$

allows a much better fit. Thus we will consider the following law to model the standard deviation of the laboratory data:

$$\sigma_\rho = 0.5998 \left(\frac{S - 0.1}{1 - 0.1} \right)^{-1.992} \quad (6.9.1)$$

At FIG. 6.23 we see that weighting the data with its standard deviation improves the fit at low moisture content. Nevertheless, as the model X SLIM was fit minimizing the relative error and considering that both the resistivity and the standard deviation exponentially increase with decreasing saturation, it is logical that the two models give similar results.

Let us write σ the standard deviation, m the model vector, and (x, y) the values of the data, the objective function to minimize can be written:

$$\phi(x) = \sum_i \left(\frac{F(m, x_i) - y_i}{\sigma(x_i)} \right)^2 + \sum_j m_j^2 \quad (6.9.2)$$

The use of a regularization parameter in the objective function is equivalent to using a Levenberg-Marquardt algorithm.

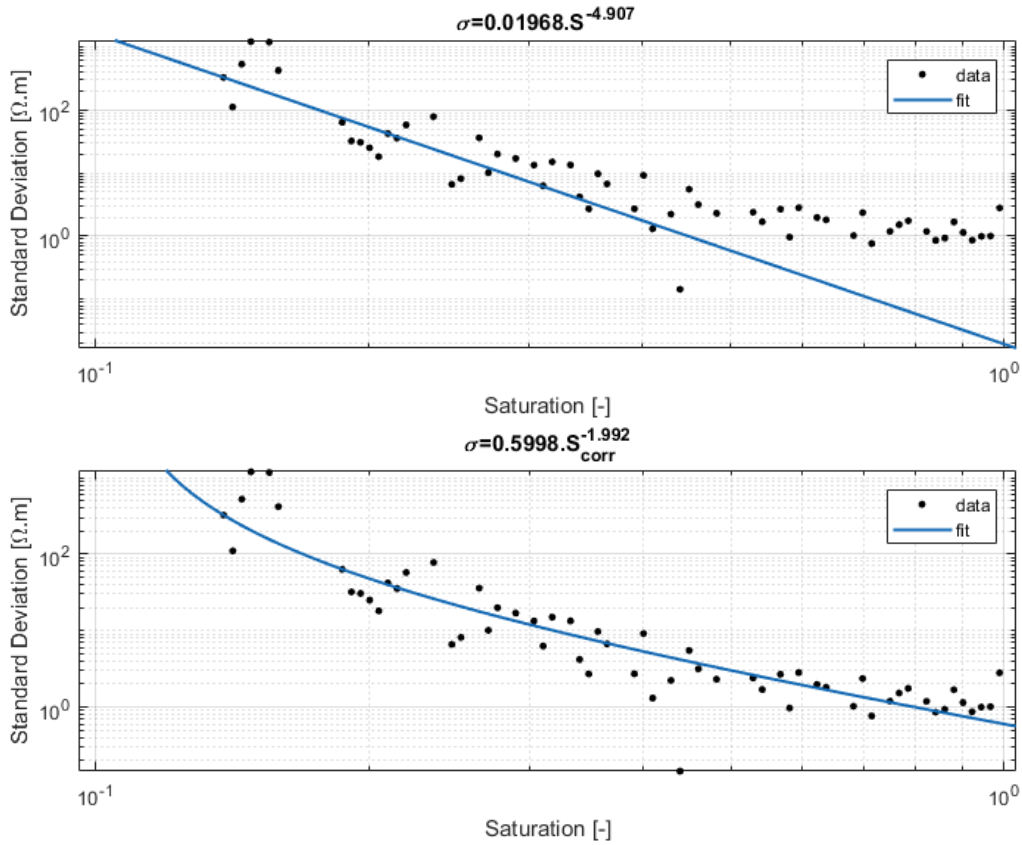


Figure 6.22: Standard deviation model based on the laboratory measurements

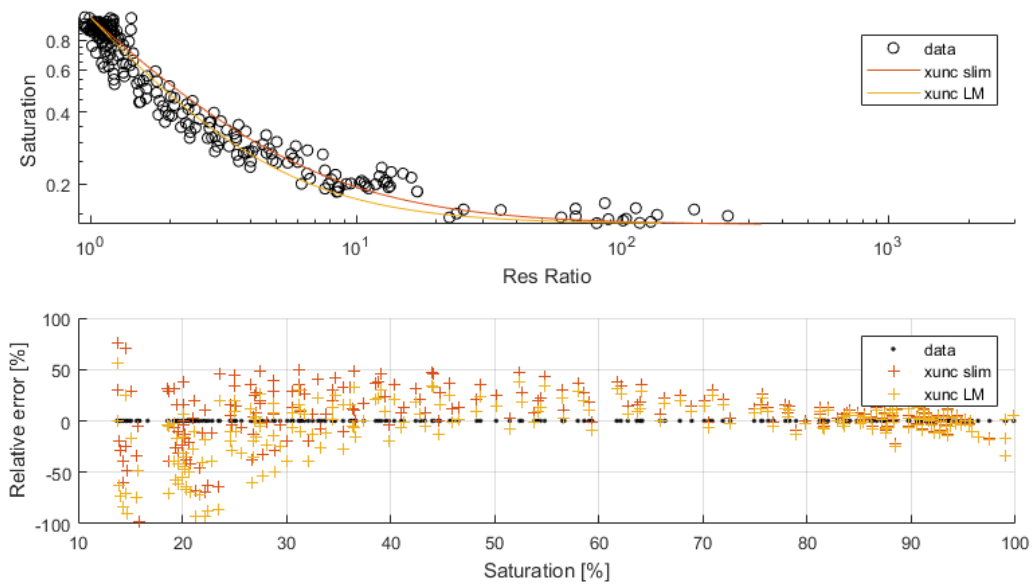


Figure 6.23: Comparison between weighted data fitting and unweighted data fitting on the laboratory measurements

Table 6.6: Results from the different fits of FIG. 6.23

Waxman-Smits (modified)	Starting model	XUNC SLIM	XUNC LM	Fixed
n [-]	1	1.8578	1.73	no
ρ_w [Ω .m]	100	100	100	yes
Q_v [eq/l]	1	1	1	yes
S_{lim} [-]	0	0.1355	0.1366	no
Iterations	0	14	6	no
Algorithm	-	<i>quasi-newton</i>	<i>quasi-newton</i>	yes
Mean relative error [%]	-	21.84	23.55	-

Chapter 7

Results

7.1 In-situ Waxman-Smiths model

7.1.1 Data selection

We discussed previously the need to normalize the moisture measurements (which is equal to working with saturation) and the resistivity measurements in the Waxman-Smiths model. We have shown that fitting an unique in-situ Waxman-Smiths model describing all the 5TE measurements and the laboratory measurements was problematic considering the discrepancy of the resistivity-moisture data relative to the chosen sensor (FIG. 7.1, RIGHT).

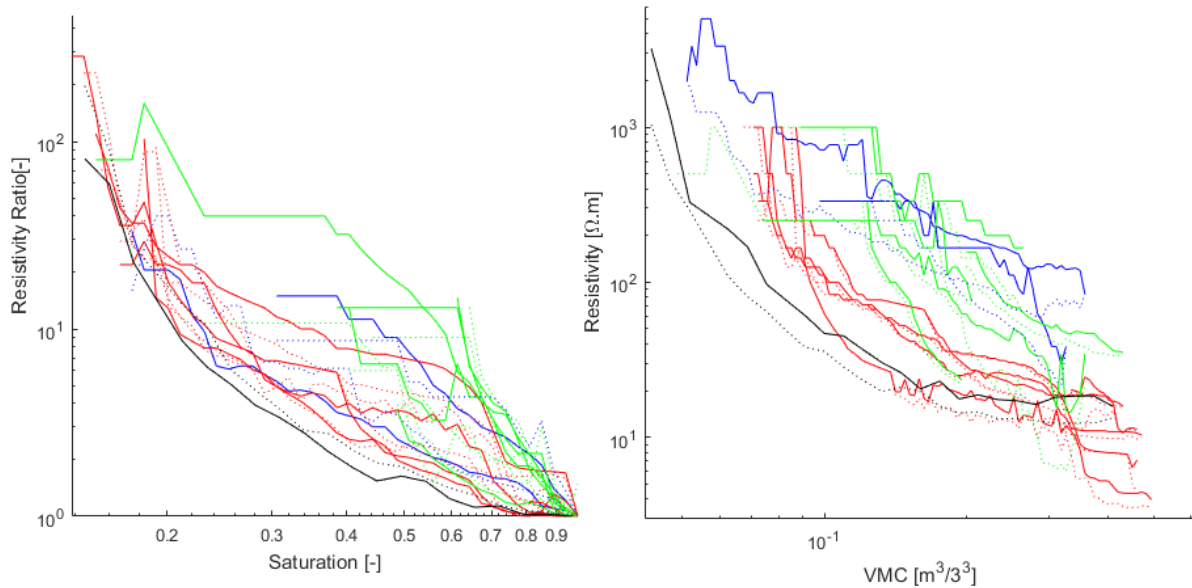


Figure 7.1: In black laboratory data, in blue Old Dalby cluster, in red, slip cluster, in green woods cluster. In solid (resp. dashed) line 99th (resp. 1st) percentile of the corresponding saturation (left) or VMC (right) range.

The 5TE volumetric moisture content measurements are converted into water saturation, S , using:

$$S = \frac{\Theta}{\Theta_{sat}} \quad (7.1.1)$$

With Θ_{sat} the minimal VMC for which saturation is reached. Θ_{sat} is supposed to be close to the VMC for which the resistivity starts to be constant. For every sensor, the resistivity at saturation,

ρ_{sat} , used to normalize the resistivity is supposed to be equal to the resistivity for which Θ_{sat} is reached.

We clearly see in the left part of FIG. 7.1 that the conversion of the data in terms of resistivity ratio and saturation reduces the discrepancy of the data. Thus, the in-situ model will be fitted on the normalized Waxman-Smiths model:

$$\frac{\rho_0}{\rho_{sat}} = \left(\frac{S - S_{lim}}{1 - S_{lim}} \right)^{1-n} \left(\frac{1 + \rho_w \cdot B \cdot Q_v}{\frac{S - S_{lim}}{1 - S_{lim}} + \rho_w \cdot B \cdot Q_v} \right) \quad (7.1.2)$$

with

$$B = 4.6 [1 - 0.6 \exp(-\sigma_w/1.3)] \quad (7.1.3)$$

FIGURE 7.2 shows, in addition to the laboratory measurements, the sensors that were used to fit the Waxman-Smiths model. If we look at the right graph of FIG. 7.2, we see that the 5TE data and the laboratory data seems to reach saturation (constant resistivity) at a volumetric moisture content of 0.35, 0.35, 0.33, 0.42, 0.28 m^3/m^3 , respectively for Old Dalby sensor 1, Slip sensor 1, 2, 3, 4 and the laboratory data. Those sensors were selected because they were the one with the most data and the less noise. Dividing all the moisture content by it corresponding saturation moisture content, and dividing the resistivity measurement by it corresponding resistivity, we obtain the left graph of FIG. 7.2. We see that the laboratory data and the 5TE data follows the same trend, so that one unique law can be applied on the data.

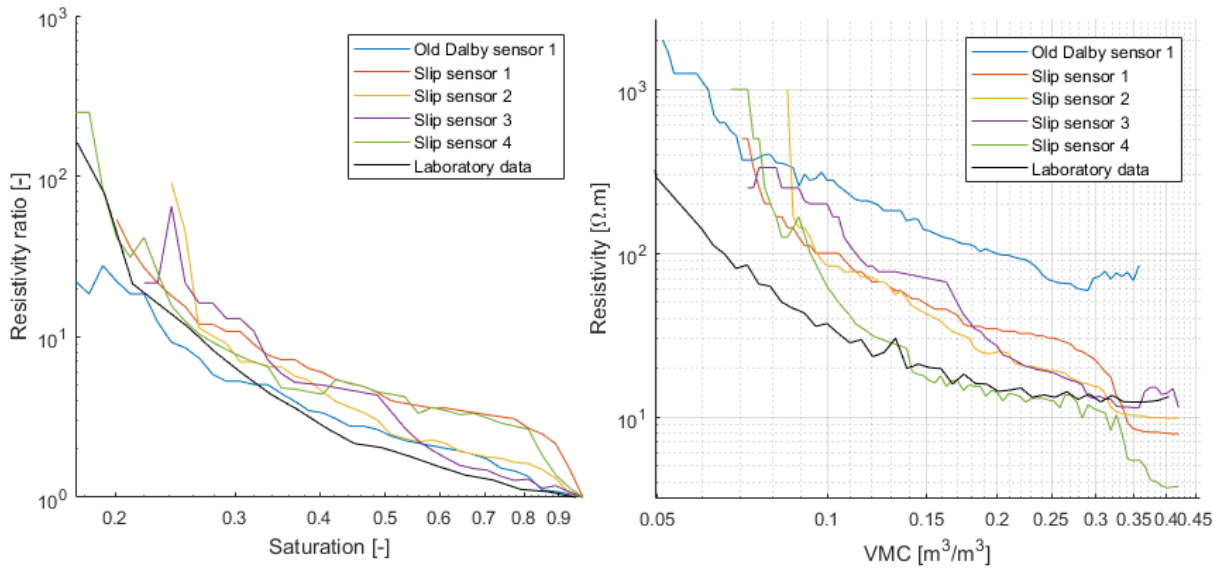


Figure 7.2: Sensors selected for fitting the Waxman-Smiths model. The plotted values corresponds to the median resistivity (resp. resistivity ratio) measured in a given range of VMC (resp. saturation).

The normalization of the data proved to minimize greatly the discrepancy between the laboratory data and the measurement made by different sensor clusters. Thus allowing the modelling of the local variations of the Waxman-Smiths model within the subsoil.

7.1.2 Fitting of the model

All the previously tested fitting methods will be compared before establishing the final model. As the R-squared is irrelevant for non-linear models, the quality of the final model will be tested by

comparing the unbiased standard error of the estimate

$$\sigma_{est} = \sqrt{\frac{\sum (Y - Y_{calc})^2}{N - 1}}$$

to the unbiased standard deviation of the data (FIG. 7.3), where the standard deviation of the resistivity ratio is assumed to vary with the saturation. 5 fitting method were tested:

- x WXM: Model fitted with the MATLAB function *lsqcurvefit*. The residual saturation S_{lim} is fixed to 0.
- XUNC WXM: Model fitted with the MATLAB function *fminunc*. The residual saturation S_{lim} is fixed to 0.
- x SLIM: Model fitted with the MATLAB function *lsqcurvefit*. The residual saturation S_{lim} is fixed to 0.16.
- XUNC SLIM: Model fitted with the MATLAB function *fminunc*. The residual saturation S_{lim} is fixed to 0.16.
- XUNC LM: Model fitted with the MATLAB function *fminunc*. The residual saturation S_{lim} is fixed to 0.16.

The objective function to minimize for the models XUNC WXM and XUNC SLIM is:

$$\phi(x) = \sum_i \left(\frac{F(m, x_i) - y_i}{F(m, x_i) + y_i} \right)^2 + \sum_j m_j^2 \quad (7.1.4)$$

The objective function to minimize for the model XUNC LM integrates the standard deviation model described by EQ. 6.9.1, it is written:

$$\phi(x) = \sum_i \left(\frac{F(m, x_i) - y_i}{\sigma_i} \right)^2 + \sum_j m_j^2 \quad (7.1.5)$$

We see at FIG. 7.3 that except the model x WXM, all the other models seems to fit well the measurements. Especially, we see at the subplot 2 & 3 of FIG. 7.3 that the standard error of the fit is very close to the standard deviation of the measurements for all the models except x WXM. Which means that most of the error can be attributed to the uncertainty of the data itself.

For all the models, the fit was established with $Qv = 1$ eq/l (see TABLE 7.1). Comparing the parameter values of the different fitted models, we see that three of the models (XUNC SLIM, XUNC LM and XUNC WXM) are to be rejected because they returned negative values of ρ_w . We have two models left, x SLIM and x WXM, comparing the error relative to the two models, we clearly see that the model x slim is more precise, thus this one will be chosen as valid.

From this we see that it is relevant to consider different fitting algorithm and/or objective function to select a model that is relevant. Also, the introduction of an additional parameter in the Waxman-Smits equation proved to significantly enhance the quality of the fit while allowing adequate parameter values.

Hence, the model that will be applied to the study site can be written:

$$\frac{\rho_0}{\rho_{sat}} = \left(\frac{S - 0.16}{1 - 0.16} \right)^{-1.252} \left(\frac{1 + 3.5296}{\frac{S-0.16}{1-0.16} + 3.5296} \right) \quad (7.1.6)$$

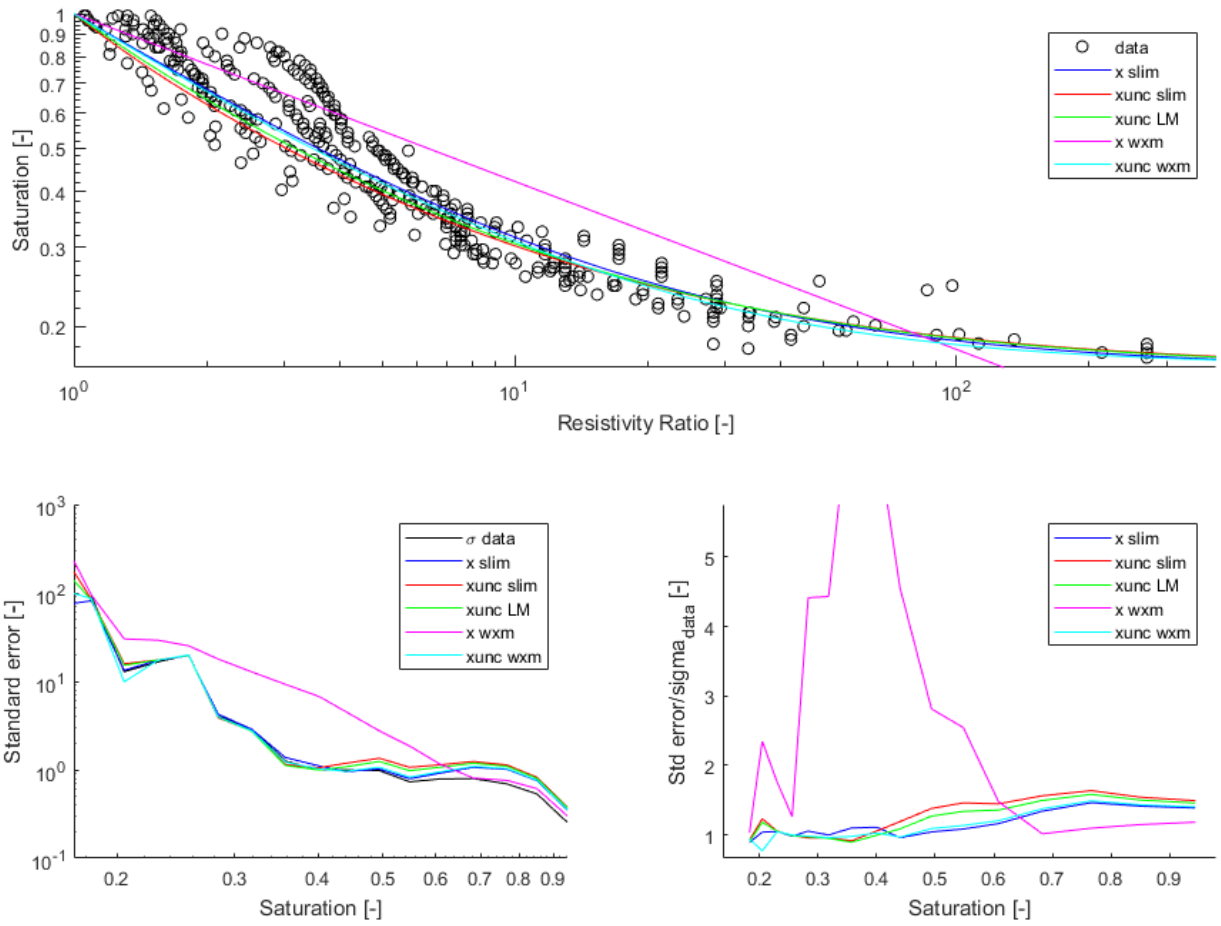


Figure 7.3: Top figure: Fitting of 5 modified Waxman-Smith model on the selected resistivity dataset. Lower figures: Comparison of the error of the fitted models with the error of the dataset

Table 7.1: Comparison between different non-linear fitting methods

Model	X SLIM	XUNC SLIM	XUNC LM	X WXM	XUNC WXM
n [-]	2.252	2.460	2.408	3.665	1.482
ρ_w [Ω .m]	1.090	-3.210	-4.383	12799.865	-1.578
Q_v [eq/l]	1.000	1.000	1.000	1.000	1.000
S_{lim} [-]	0.160	0.160	0.160	0.000	0.000
Iterations	29.000	11.000	10.000	32.000	15.000
Mean relative error [%]	26.739	29.400	28.152	53.024	26.005
Mean Std. Error/Std. Dev.	1.128	1.236	1.188	2.826	1.111

7.2 Inversion results

The inversion of the monitoring data gives a 4D imaging of the resistivity of the subsoil.

7.2.1 Inversion parameters

The inversion parameters are the following:

Damping Factor A small initial damping factor (0.1) was chosen for the inversion as the data set contained very little noise. The damping factor reduces after each iteration and the minimal damping factor was set to 0.01.

To stabilize the inversion process as the resolution of the resistivity decreases exponentially with depth, the damping factor is increased with each deeper layer by a 1.01 factor.

Thickness of layers The thickness of the first layer was set to 0.707 m, with each deeper layer increasing with a factor 1.15. The line 1, 2 and 4 contains 7 layers, so they are 7.82 m deep, and the lines 3 and 5 contains 5 layers so they are 4.76 m deep.

Robust data constraint To minimize the effect of outliers on the RMS calculation, the error due to data points for which the difference between measured and calculated apparent resistivity values are greater than 1% will be reduced.

As no sharp boundaries is expected in the area of the survey, the robust model constrain was not selected.

RMS convergence limit The cut-off value of the RMS for which the inversion process stops was set to 5% with a minimum change in RMS error of 0.2%. If those conditions are not met the program will stop after 5 iterations.

To produce a model with smooth variations in the resistivity values and avoid negative values, the computation was carried out using the logarithm of apparent resistivity.

To avoid physically unrealistic extremely large or small resistivity values, the resistivity values that the inversion process can give was constrained. The upper limit factor was set to 50 and the lower limit factor was set to 0.02. Those values accounts for the average model resistivity of the previous iteration.

Solving algorithm 3D timelapse inversion implies a very high number of points to take into account. To reduce the inversion time 'incomplete Gauss-Newton' method with data compression was chosen. This alternative method calculates an approximate solution of the least-square equation for which the user can set the accuracy of the solution. In our case the accuracy of the solution was set to 1%.

Time-Lapse inversion constrain Time lapse inversion constrain was selected, with the reference model set to the first data set. No constrain was added to minimize the changes between successive time-steps. The results of the first ERT are shown at FIG. 7.4.

7.2.2 Saturation imaging

At FIG. 7.7 we see the saturation imaging obtain from the application of the saturation-resistivity model on the inversed resistivity results. We can point out some characteristics of the study site:

- The dynamic of the area is mostly represented in the top 3 meters,

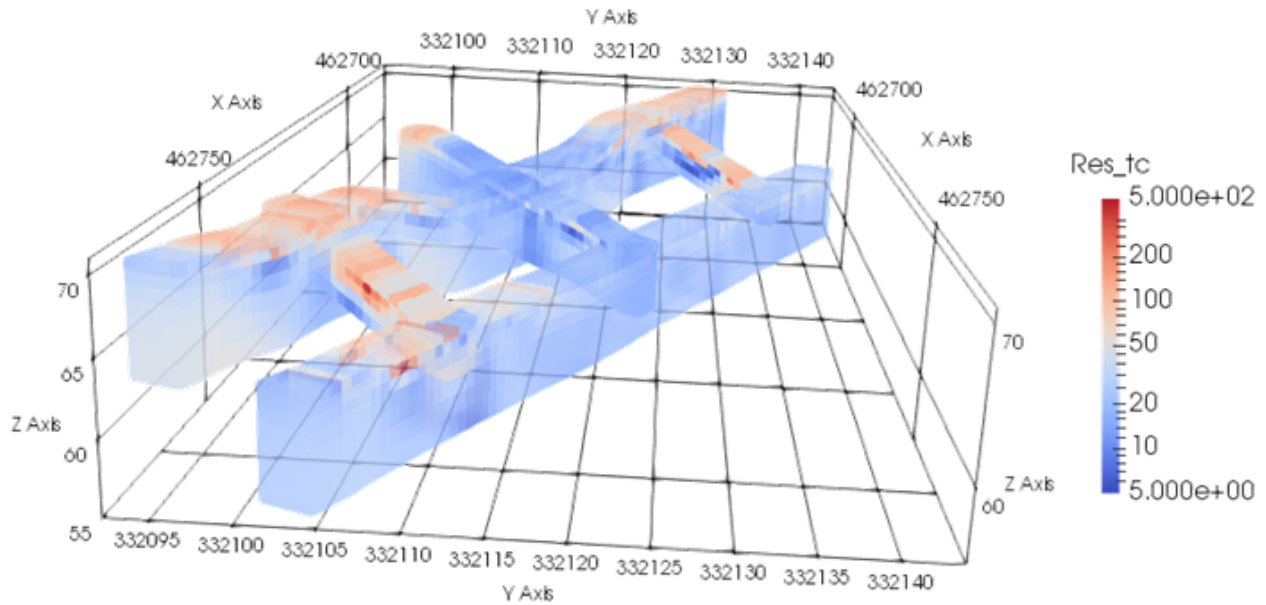


Figure 7.4: Resistivity (without temperature correction) of the first ERT. Values are expressed in $\Omega.m$

- The area of the landslide shows higher values of saturation all around the year

As the dynamic of the area is mostly contained in the first meters of soil, let compare the ERT-derived saturation results to the infiltration data. For this purpose the first 3 cells of the Line 2 were selected, the results are shown at FIG. 7.5. We see that both curves follows the same trend, which means that the saturation strictly follows the infiltration path: saturation increases when infiltration is positive and decreases when infiltration is negative.

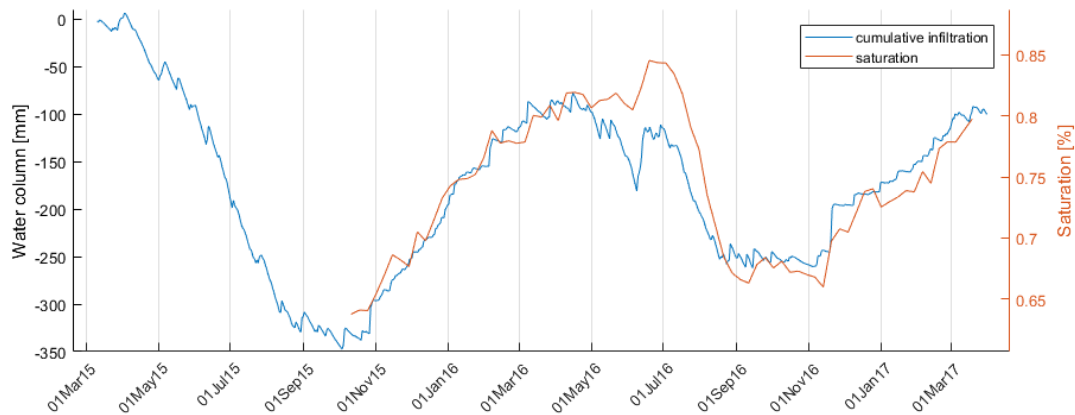


Figure 7.5: Comparison between the cumulative infiltration measured at the weather station and the mean ERT-derived saturation calculated for the top 3 meters of Line 2

It is interesting and a bit counter intuitive to observe that the maximal ERT-derived mean saturation in 2016 is reached at the end of spring (at the beginning of July 2016) and that the minimal ERT-derived saturation is reached at the end of autumn (at the beginning of November 2016). Comparing the ERT-derived saturation with the cumulative infiltration makes this observation obvious:

- despite a negative spike in June 2016, the infiltration is globally positive from November 2015 until July 2016 (maximum ERT-derived saturation),
- then the cumulative infiltration decreases quickly during July and August before being constant until November 2016 (minimum ERT-derived saturation),
- after November 2016 the cumulative infiltration rises again and the cycle restarts.

Unfortunately we do not have ERT monitoring data before October 2015, but according to the infiltration curve the maximum ERT-derived saturation in 2015 should be observed in March. Thus, the observation of maximum ERT-derived saturation in July 2016 could be characteristic of year 2016, due to an exceptionally cold and wet spring.

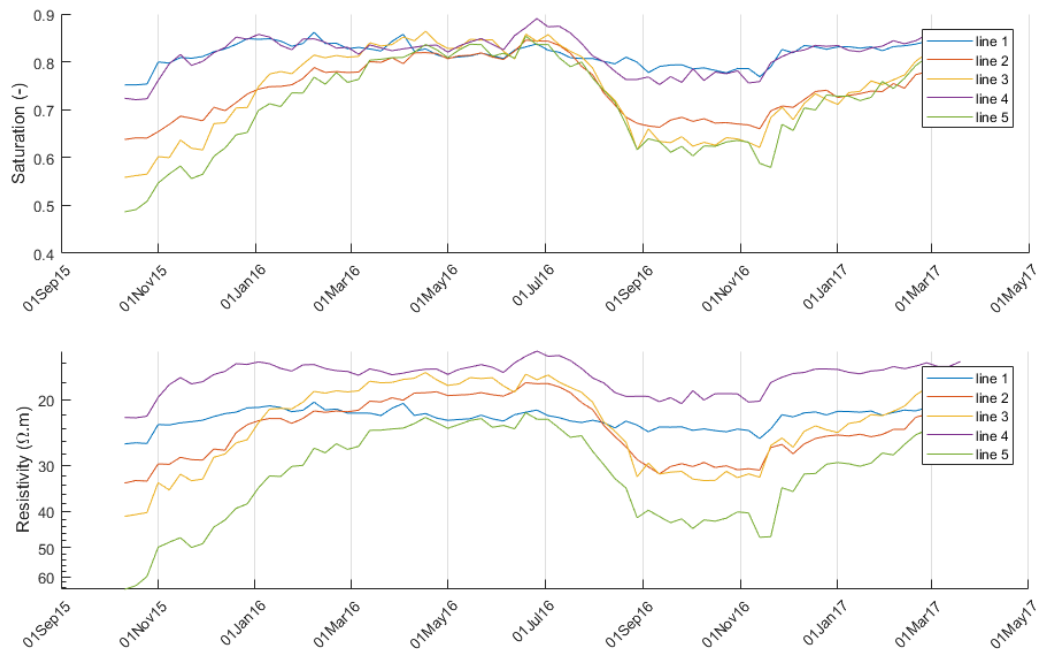


Figure 7.6: ERT-derived Saturation (subplot 1) and resistivity (subplot 2) mean values calculated for the first three meters of each lines.

We see at FIG. 7.6 that when we convert the average resistivity values into ERT-derived saturation, even if they don't have the same logarithmic average resistivity values we can group lines 2, 3 and 5 and lines 1 and 4 after saturation conversion. Considering the size of the survey and the low expected heterogeneity of the subsoil in the first 3 m, it seems coherent to observe similar saturation values for the different lines as they are subject to the same local conditions (temperature, precipitation). The saturation difference between the lines 2, 3 and 5 and lines 1 and 4 can be attributed to vegetation: lines 2, 3 and 5 are located within a vegetated area. Evapotranspiration is higher in vegetated areas, therefore it is coherent to observe cycles with lower minimal saturation for lines located in vegetated areas. During the winter, the evapotranspiration in vegetated areas is very low and the first meters of subsoil are able to reach saturation values close to saturation. Which is actually observed as the average maximum saturation is similar for every lines (FIG. 7.6).

7.2.3 Study of the decrease between June and September

To investigate more precisely the correlation between moisture movements and effective infiltration, a smaller dataset (data selected every day) was investigated for the period ranging from the month of May 2016 till the month of September 2016. FIG. 7.8 shows the time variation of the resistivity

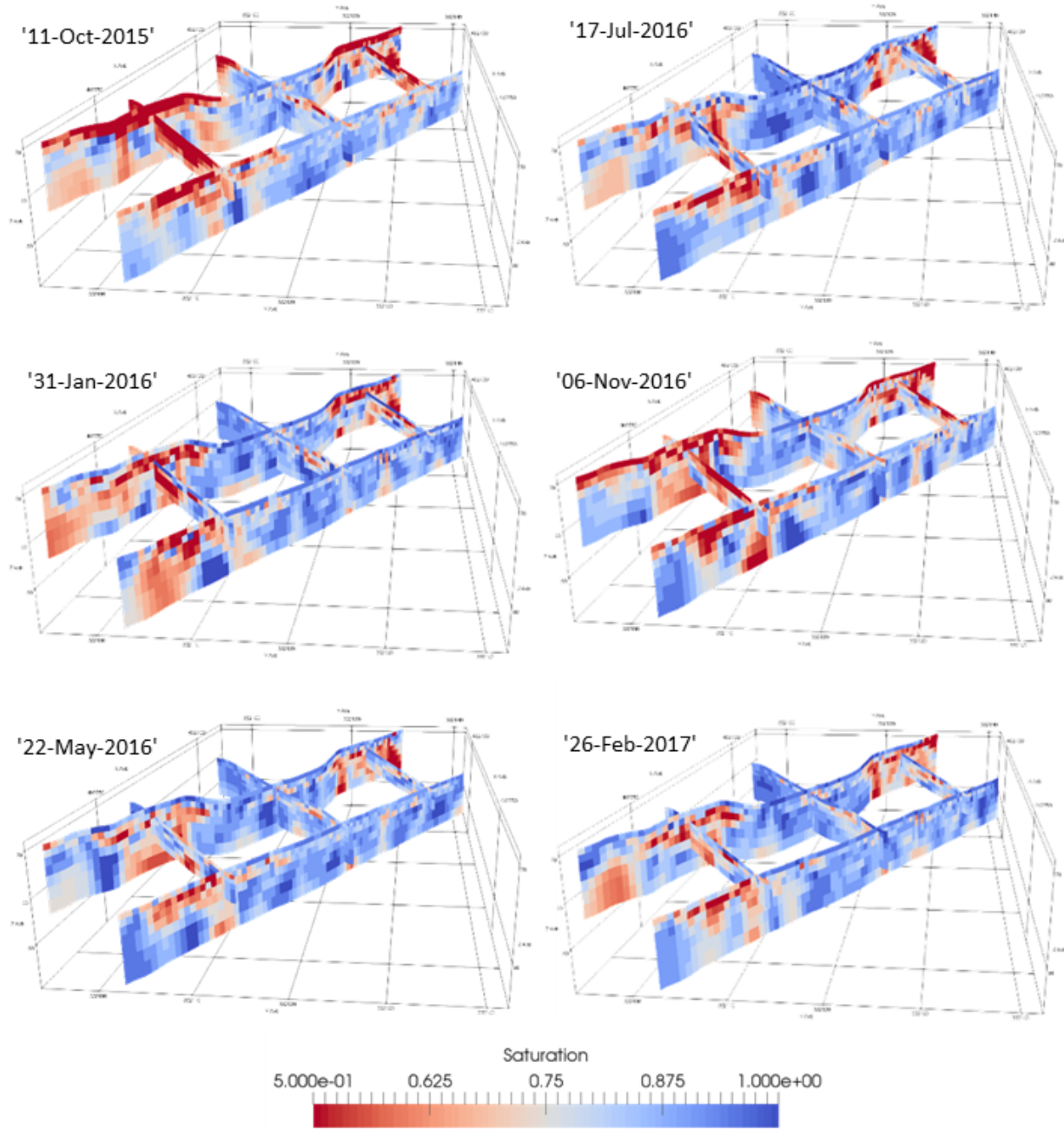


Figure 7.7: ERT derived saturation imaging of the subsoil

and ERT-derived saturation mean values of the first three inversion cells of the survey. We see that the maximum observed ERT-derived saturation is similar for each lines, but that the drying dynamic is not the same: some areas of the study site (line 2,3 and 5) dries much quicker than the others. Considering that the line 4 is located in an area with no vegetation and that the line 1 is located at the foot of the embankment and contains vegetation only at it extremities, it seems logical that these lines dries more slowly as the should be evapotranspiration lower. The same result is observed when comparing the mean ERT-derived saturation of the central part (no vegetation) of lines 1 and 2 to that of the extremities (with vegetation).

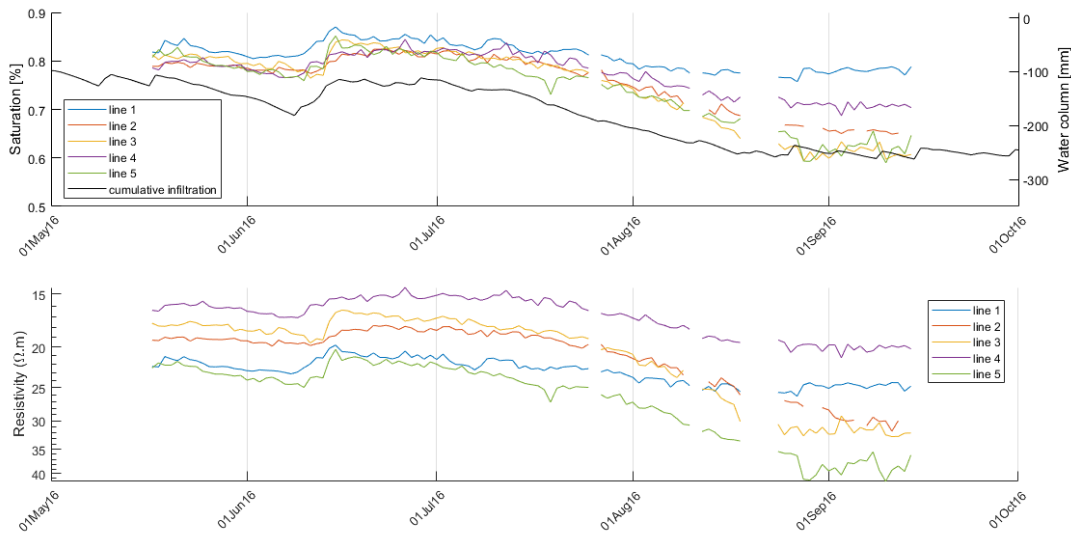


Figure 7.8: ERT-derived Saturation (subplot 1) and resistivity (subplot 2) mean values calculated for the first three meters of each lines.

The Waxman-Smiths model was used to study the impact of noise in the resistivity ratio measurements on the saturation mapping. FIG. 7.9 shows that the impact of the noise is more important at high saturation, but that in all cases the relative error induced in the saturation evaluation remains smaller than the initial relative resistivity error.

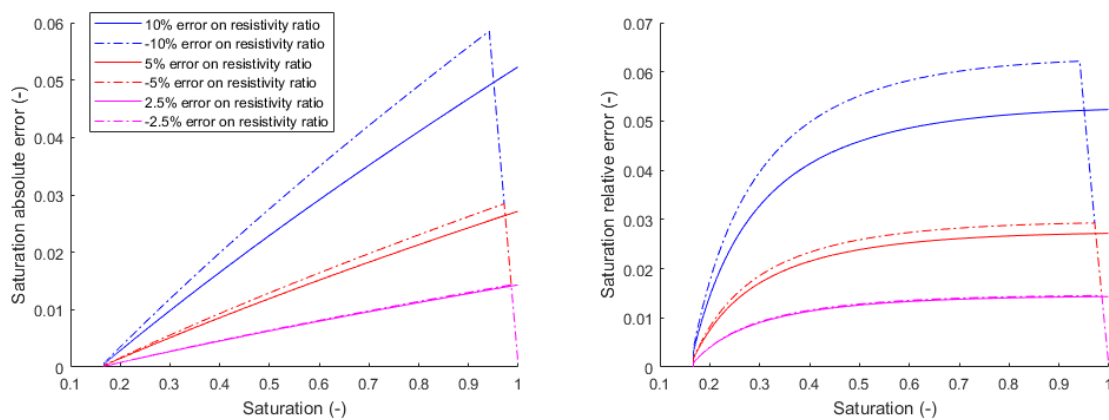


Figure 7.9: Effect of resistivity ratio error on saturation evaluation

7.3 Suction monitoring

The last part of the study consists in imaging the suction of the subsoil from the ERT monitoring. Considering that we observe a clear linear trend when the logarithm of the suction is plotted against saturation, it was decided not to fit a Van-Genuchten model and to simply consider an exponential law to model the suction drying and wetting curves (FIG. 7.10).

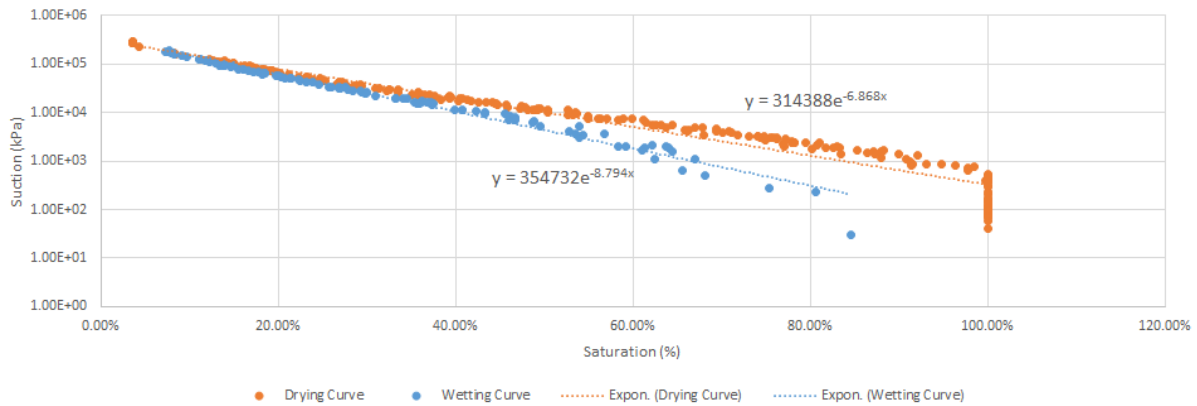


Figure 7.10: Water retention curve established from laboratory testing of compacted material drilled on site

We see at FIG. 7.10 that, for a given saturation, the wetting curve shows lower values of the soil suction. The wetting curve corresponds to the worst case scenario in terms of subsoil stability and will be used to monitor the soil suction. Applying the soil-suction - saturation relation on the saturation data, we can image the suction of the subsoil (FIG. 7.12).

We observe at FIG. 7.12 that the area of the landslide corresponds to the area with lower suction values. As the shear strength of a soil decreases with decreasing suction, this observation shows that the landslide occurred in the area with the highest risk according to soil suction mapping.

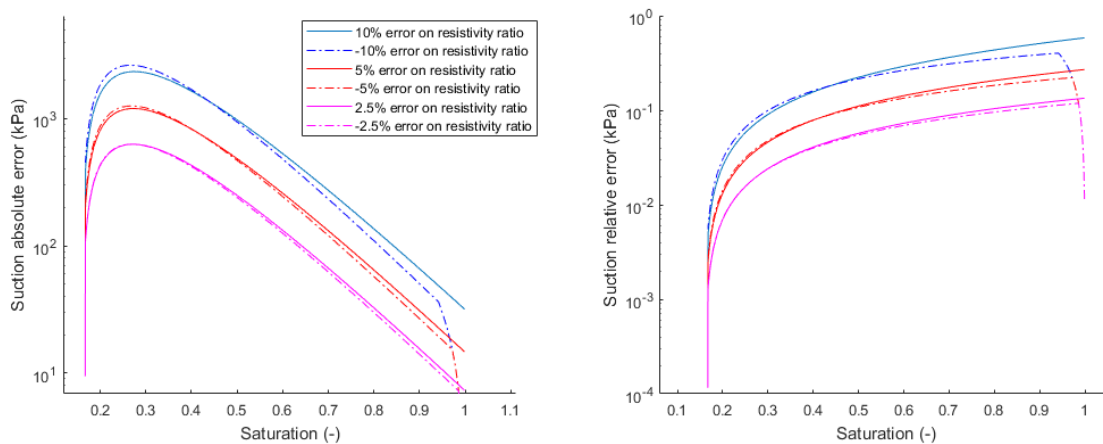


Figure 7.11: Effect of resistivity ratio error on suction evaluation

As for the saturation, we studied the impact of the resistivity ratio error on the suction evaluation. We see at FIG. 7.11 that the impact of the error is very important at high moisture content. At high saturation values the suction relative error is 4 times higher than the initial resistivity ratio relative error. This means that ERT-derived suction values in areas highly saturated are highly sensitive to noise.

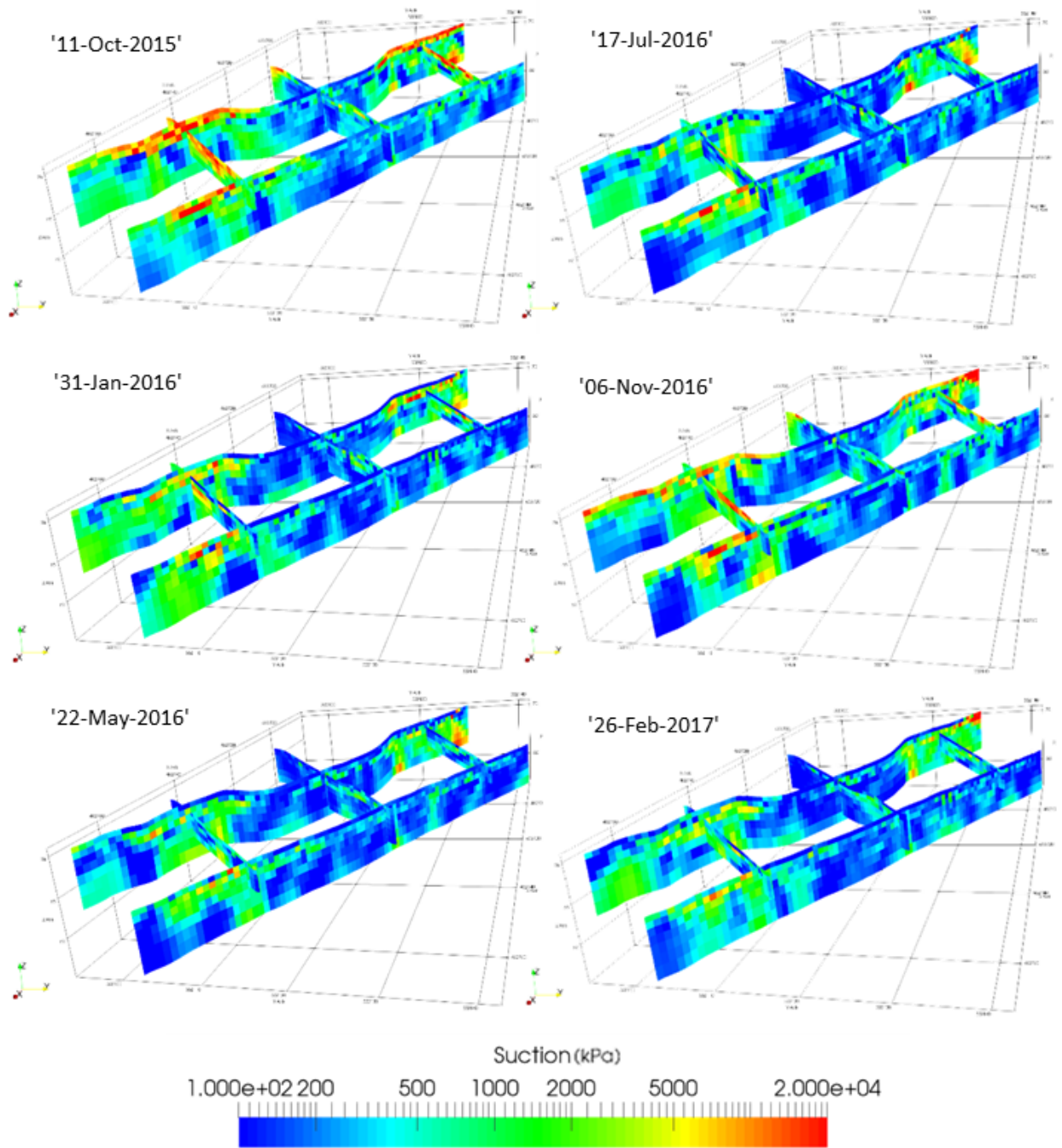


Figure 7.12: ERT-derived suction imaging of the subsoil

Chapter 8

Conclusions and recommendations for future works

Every year, unexpected landslide occurrence generates loss of serviceability, reconstruction costs and human casualties (Kirschbaum et al., 2015). High subsoil moisture is a triggering element in landslide failure, and its monitoring would allow to reduce the impact on loss of serviceability, reconstruction costs and human casualties.

The Old Dalby site is located on a subsoil composed of quaternary tills followed by a succession of Triassic mudstone layers. Those formations have poor geotechnical characteristics as tills is the UK's superficial soil in which landslides are the most reported (Trenter, 1999). In addition to the poor subsoil cohesion, the wetting/drying cycles recorded in the subsoil enhance the subsoil weathering. This weathering combined to extended periods of high water infiltration greatly increases the risk of landslide occurrence.

This study showed the efficiency of time-lapse electrical resistivity tomography to image the moisture dynamics of the subsurface. A multi-step methodology was applied to convert the time-lapse ERT data into water saturation imaging. This includes subsoil temperature modelling to correct the temperature effect on resistivity mapping and laboratory based modelling of the resistivity-saturation relation.

The study of the laboratory resistivity-moisture measurements highlighted the effect of residual moisture content on resistivity at low moisture content. In fact, we showed that without introducing a term accounting for the residual moisture content, S_{lim} , the Waxman-Smits model was unable to model the resistivity-moisture behaviour at both low and high moisture content.

The analysis of both in-situ 5TE and laboratory based resistivity-moisture measurements showed that the moisture content values needed to be normalized (which is equivalent to work with saturation values) and that parameters of the Waxman-Smits model (especially the formation factor) were varying in space. In fact, we observed that:

- the moisture content for which full saturation is reached is heterogeneous,
- for a given saturation, the associated resistivity value can vary with a factor greater than ten.

We showed that adequate data normalization allowed to unify the Waxman-Smits model for sensors from different locations (Fig. 8.1). The normalization is done by identifying the moisture content to which saturation is reached, w_{sat} , and the resistivity at saturation, ρ_{sat} .

A new approach based on saturated resistivity evaluation was considered to model the heterogeneity of the subsoil. The resistivity at saturation was imaged under the assumption that every part of the study site reaches saturation over a 1.5 year period. This approach proved its efficiency by successfully identifying the local variations of the saturated resistivity.

The introduction of the residual water saturation term, S_{lim} , associated to the saturated resistivity mapping showed that it was possible to have a unified Waxman-Smits model accounting

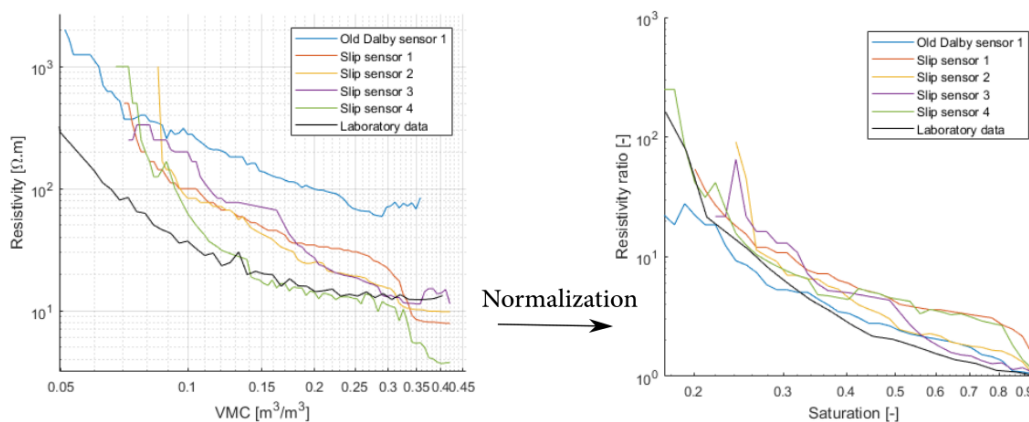


Figure 8.1: Effect of data normalization on the resistivity-moisture data

for local variations in the parameters of the Waxman-Smits model and valid at both low and high moisture content. This demonstrated the adequacy of the approach in accounting for subsoil local heterogeneity.

The results from the saturation modelling showed that, at low depth, there was a very good correlation between the mean saturation and the cumulative infiltration curve, evaluated from the temperature and raining data from the weather station located on site. It was highlighted that the dynamic of the subsoil was restricted to the first three meters of the subsoil and that at higher depth the subsoil mean saturation was nearly constant and was staying close to saturation.

Based on the study we validated the use of the 5TE in-situ measurements to fit a Waxman-Smits model. This approach has the advantage of working with in-situ data and allows to measure the in-situ hysteresis between successive wetting-drying cycles. However, it cannot be used directly because some wetting/drying cycles must be measured before a relationship can be established. Hence, the use of 5TE data is not appropriate at the beginning of studies where the saturation imaging is required directly.

The quality of the ERT-derived saturation modelling proved that it was possible to identify the areas with high saturation. Considering the great correlation between the infiltration and the subsoil moisture dynamic, the cumulative infiltration monitoring coupled with ERT measurements provides a effective tool to

- properly evaluate the periods during which the risk of slip is maximal,
- identify areas of the subsoil for which the risk of slip is highest.

Further studies should try to understand more precisely the effect of residual water content and successive wetting/drying cycles hysteresis on the resistivity behaviour. This could give information on how to interpret the hysteresis observed on the 5TE data. Especially, the variation of the amplitude of the hysteresis over successive wetting/drying cycles could be representative of the state of alteration of the subsoil.

Chapter 9

Glossary of terms

- GMC: Gravimetric moisture content (kg/kg)
VMC: Volumetric moisture content (m^3/m^3)
PI: Plasticity index (% GMC)
LL: Liquid limit (% GMC)
PL: Plastic limit (% GMC)
PSA: Particle size analysis
OMC: Optimum moisture content (% GMC)
 m_s : Mass of the soil sample (kg)
 m_w : Mass of fluid in pores (kg)
 m_{dry} : Mass of dry soil sample (kg)
 V_w : Volume of fluid in pores (m^3)
 V_{dry} : Volume of dry soil sample (m^3)
 V_s : Volume of the soil sample (m^3)
 d_{dry} : Mass density of dry soil sample (kg/m^3)
 d_s : Soil particle density (kg/m^3)
 d_w : Mass density of fluid contained in pores (kg/m^3)
 γ_w : Specific weight of fluid contained in pores (N/m^3)
w: Gravimetric moisture content (kg/kg)
 w_{sat} : Minimum gravimetric moisture content for which soil is saturated (% GMC)
 Θ : Volumetric moisture content (m^3/m^3)
 ϕ : Soil porosity (-)
S: Water saturation of porous rock (-)
 S_{lim} : Residual water saturation (-)
 Q_v : Cation concentration per unit pore volume (meq/m^3)
B: Average mobility of ions (-)
c: Cation exchange capacity ($\text{meq}/100\text{g}$)
F: Formation factor (-)
n: Saturation exponent (-)
 ϵ_r : Dielectric constant of medium (-)
 ϵ_0 : Permittivity of free space (F/m)
 ϵ : Absolute permittivity of medium (F/m)
pF: Logarithm of soil suction expressed in cm (-)
P: Soil suction (Pa)
 ψ_t : Total potential of soil water (Pa)
k: geometrical factor (-)
T: Temperature ($^{\circ}\text{C}$)
A: Activation energy of conduction (J/mol)

- R: Universal gas constant (J/mol.K)
 m: Fractional change in conductivity per degree celsius (-)
 I: Electrical current (A)
 V: Voltage (V)
 Z: Impedance ratio (Ω)
 ρ : Resistivity ($\Omega.m$)
 ρ_a : Apparent resistivity ($\Omega.m$)
 ρ_{25} : Resistivity corrected at 25°C ($\Omega.m$)
 ρ_T : Resistivity measured at temperature T ($\Omega.m$)
 ρ_0 : Bulk electrical resistivity of porous rock ($\Omega.m$)
 ρ_{sat} : Bulk resistivity of fully saturated soil ($\Omega.m$)
 $\rho_{e,sat}$: Clay exchange cations resistivity of saturated soil ($\Omega.m$)
 ρ_w : Resistivity of fluid contained in pores ($\Omega.m$)
 ρ_e : Clay exchange cations resistivity ($\Omega.m$)
 σ Conductivity (S/m)
 σ_0 : Bulk electrical conductivity of porous rock (S/m)
 σ_{sat} : Bulk conductivity of fully saturated soil (S/m)
 $\sigma_{e,sat}$: Clay exchange cations conductivity of saturated soil (S/m)
 σ_w : Conductivity of fluid contained in pores (S/m)
 σ_e : Clay exchange cations conductivity (S/m)

Bibliography

- [1] Archie, G. E. et al. “The electrical resistivity log as an aid in determining some reservoir characteristics”. In: *Transactions of the AIME* 146.01 (1942), pp. 54–62.
- [2] Aster, R. C., Borchers, B., and Thurber, C. H. *Parameter estimation and inverse problems: Elsevier Academic*. 2nd ed. Elsevier, 2013, p. 366.
- [3] Belcher, S, Slingo, J, McCarthy, R, Burton, C, et al. “Too Hot, Too Cold, Too Wet, Too Dry: Drivers and Impacts of Seasonal Weather in the UK”. In: *MetOffice, Exeter* (2014).
- [4] Chambers, J. E., Gunn, D. A., Wilkinson, P. B., Meldrum, P. I., et al. “4D electrical resistivity tomography monitoring of soil moisture dynamics in an operational railway embankment”. In: *Near Surface Geophysics* 12.1 (2014), pp. 61–72.
- [5] Constable, S. C., Parker, R. L., and Constable, C. G. “Occam’s inversion: A practical algorithm for generating smooth models from electromagnetic sounding data”. In: *Geophysics* 52.3 (1987), pp. 289–300.
- [6] Decagon Inc., D. *WP4C Dewpoint potentiometer, operator’s manual. Decagon Devices Inc.* 2015.
- [7] Department of the environment. “Landsliding in Great Britain”. In: *Her majesty’s Stationery Office* (1994).
- [8] En.wikipedia.org. *Atterberg limits*. 2017. URL: https://en.wikipedia.org/wiki/Atterberg_limits#Liquidity_index (visited on 04/27/2017).
- [9] Everett, M. E. *Near-surface applied geophysics*. Cambridge University Press, 2013.
- [10] Gibbard, P. L. and Clark, C. D. “Pleistocene glaciation limits in Great Britain”. In: *Quaternary Glaciations–Extent and Chronology–A Closer Look. Developments in Quaternary Science* 15 (2011), pp. 75–94.
- [11] Hartmann, R. *Soil water potential*. 2003. URL: <http://indico.ictp.it/event/a0261/session/33/contribution/22/material/0/0.pdf> (visited on 12/05/2017).
- [12] Hayley, K., Bentley, L., Gharibi, M, and Nightingale, M. “Low temperature dependence of electrical resistivity: Implications for near surface geophysical monitoring”. In: *Geophysical research letters* 34.18 (2007).
- [13] Head, K. H. and Epps, R. *Manual of soil laboratory testing: Soil classification and compaction tests*. 2nd ed. Vol. 1. Pentech Press London, 1992.
- [14] Hen-Jones, R., Hughes, P., Stirling, R., Glendinning, S, Chambers, J., Gunn, D., and Cui, Y. “Seasonal effects on geophysical–geotechnical relationships and their implications for electrical resistivity tomography monitoring of slopes”. In: *Acta Geotechnica* (2017), pp. 1–15.
- [15] Hermans, T. “The use of a priori information in electrical resistivity tomography for salt water intrusion studies at the Belgian coast”. PhD thesis. Universite de Liège, Belgique, 2010.

- [16] Hobbs, P., Hallam, J. R., Forster, A., Entwisle, D., et al. "Engineering geology of British rocks and soils: Mudstones of the Mercia Mudstone Group". In: *British Geological Survey Research Report* (2002), p. 106.
- [17] Jackson, P. D., Northmore, K. J., Meldrum, P. I., Gunn, D. A., Hallam, J. R., and Wambura, J. "Non-invasive moisture monitoring within an earth embankment - a precursor to failure". In: *NDT&E International* 35 (2002), pp. 107–115.
- [18] Jackson, P., Gunn, D., Flint, R., Beamish, D., Meldrum, P., Lovell, M., Harvey, P., and Peyton, A. "A non-contacting resistivity imaging method for characterizing whole round core while in its liner". In: *Geological Society, London, Special Publications* 122.1 (1997), pp. 1–10.
- [19] Jongmans, D. and Garambois, S. "Geophysical investigation of landslides: a review". In: *Bulletin de la Société géologique de France* 178.2 (2007), pp. 101–112.
- [20] Kirschbaum, D., Stanley, T., and Zhou, Y. "Spatial and temporal analysis of a global landslide catalog". In: *Geomorphology* 249 (2015), pp. 4–15.
- [21] Lee, J. R., Rose, J., Hamblin, R. J., Moorlock, B. S., Riding, J. B., Phillips, E., Barendregt, R. W., and Candy, I. "The glacial history of the British Isles during the Early and Middle Pleistocene: implications for the long-term development of the British Ice Sheet". In: *Quaternary Glaciations—Extent and Chronology, A Closer Look. Developments in Quaternary Science. Elsevier, Amsterdam* (2011), pp. 59–74.
- [22] Loke, M. "Electrical imaging surveys for environmental and engineering studies". In: *A practical guide to 2-D and 3-D Surveys* (1999).
- [23] Markwick, A. H. D. "The basic principles of soil compaction and their application. Road Engineering Division." In: *The Institution of Civil Engineers Engineering Division Papers* 3.3 (1945), pp. 1–48.
- [24] METER Group, I. U. *Soil Moisture, Temperature, and Electrical Conductivity. Engineered for accuracy.* 2017. URL: <https://www.metergroup.com/environment/products/ech2o-5te-electrical-conductivity/> (visited on 12/17/2017).
- [25] Pennington, C., Freeborough, K., Dashwood, C., Dijkstra, T., and Lawrie, K. "The National Landslide Database of Great Britain: acquisition, communication and the role of social media". In: *Geomorphology* 249 (2015), pp. 44–51.
- [26] Perrone, A., Lapenna, V., and Piscitelli, S. "Electrical resistivity tomography technique for landslide investigation: a review". In: *Earth-Science Reviews* 135 (2014), pp. 65–82.
- [27] Perry, J., Pedley, M., and Reid, M. *Infrastructure embankments: condition appraisal and remedial treatment.* London: Construction Industry Research and Information Association, 2003.
- [28] Rücker, C. "Advanced electrical resistivity modelling and inversion using unstructured discretization". In: (2010).
- [29] Sharma, S. and Verma, G. K. "Inversion of Electrical Resistivity Data: A Review". In: *World Academy of Science, Engineering and Technology, International Journal of Environmental, Chemical, Ecological, Geological and Geophysical Engineering* 9.4 (2015), pp. 400–406.
- [30] Sowers, G. F. "Introductory Soil Mechanics & Foundations". In: *Geotechnical engineering* 92 (1979), pp. 114–117.
- [31] Topp, G. C., Davis, J., and Annan, A. P. "Electromagnetic determination of soil water content: Measurements in coaxial transmission lines". In: *Water resources research* 16.3 (1980), pp. 574–582.
- [32] Trenter, N. *Engineering in glacial tills.* London: Construction Industry Research and Information Association, 1999.

- [33] Uhlemann, S., Chambers, J., Wilkinson, P., Maurer, H., et al. “4D imaging of moisture dynamics during landslide reactivation”. In: *Journal of Geophysical Research: Earth Surface* (2016).
- [34] USGS. *USGS Develops Geophysical Methods to Improve Remediation Monitoring and Site Characterization*. 2017. URL: https://toxics.usgs.gov/highlights/geophysical_methods.html (visited on 06/06/2017).
- [35] Warrington, G and Ivimey-Cook, H. “Triassic”. In: *Geological Society, London, Memoirs* 13.1 (1992), pp. 97–106.
- [36] Waxman, M. and Smits, L. “Electrical conductivities in oil-bearing shaly sands”. In: *Society of Petroleum Engineers Journal* 8.02 (1968), pp. 107–122.

Appendix A

Water in soils

Writing V_w the volume of water contained in pores, V_v the volume of pores, m_w the mass of water contained in pores, m_d the dry mass of the sample and V the total volume of the sample, we have:

$$S = \frac{V_w}{V_v} \quad (\text{A.0.1})$$

and

$$w = \frac{m_w}{m_d} \quad (\text{A.0.2})$$

and

$$\phi = \frac{V_v}{V} \quad (\text{A.0.3})$$

Where S is the saturation, w is the gravimetric moisture content and ϕ is the soil porosity. Writing, V_s the volume of the solid part of the sample, we have

$$S = \frac{V_w}{V - V_s} \quad (\text{A.0.4})$$

Writing ρ the bulk density of the soil sample, ρ_s the particle density of the soil sample and ρ_w the density of the fluid contained in the pores, the expression can be written

$$S = \frac{\frac{w \cdot m_d}{\rho_w}}{\frac{w \cdot m_d + m_d}{\rho} - \frac{m_d}{\rho_s}} \quad (\text{A.0.5})$$

Which yields to

$$S = \frac{w \cdot \rho \cdot \rho_s}{\rho_w \cdot [(w + 1) \cdot \rho_s - \rho]} \quad (\text{A.0.6})$$

The volume of the sample can be split between the solid part and the pore space, thus we have

$$V = V_s + V_v = V_s + \phi \cdot V = V_s + \phi \cdot (V_s + \phi \cdot V) = V_s + \phi \cdot V_s + \phi^2 \cdot V_s + \dots = \quad (\text{A.0.7})$$

Knowing that $0 < \phi < 1$, we can write

$$V = \frac{V_s}{1 - \phi} \quad (\text{A.0.8})$$

Similarly, the density of the sample, ρ , can be expressed

$$\rho = \frac{m_d + m_w}{V} = \frac{(1 + w) \cdot m_d}{V} = \frac{(1 + w) \cdot \rho_s V_s}{V} \quad (\text{A.0.9})$$

Considering Eq. A.0.8, the density can be written

$$\rho = (1 + w) \cdot \rho_s \cdot (1 - \phi) \quad (\text{A.0.10})$$

Using EQ. A.0.10 in EQ. A.0.6, the saturation, S , can be written

$$S = \frac{w \cdot (1 + w) \cdot \rho_s \cdot (1 - \phi) \cdot \rho_s}{\rho_w \cdot [(1 + w) \cdot \rho_s - (1 + w) \cdot \rho_s \cdot (1 - \phi)]} \quad (\text{A.0.11})$$

Which simplifies as

$$S = \frac{w \rho_s (1 - \phi)}{\rho_w \phi} \quad (\text{A.0.12})$$


Assuming that the porosity is constant in the unsaturated domain, we can evaluate the value of the moisture content for which the sample starts to be saturated ($S=1$):

$$\rho_{sat} = (1 + w_{sat}) \cdot \rho_s \cdot (1 - \phi) \quad (\text{A.0.13})$$

Knowing that $S = 1$ when the sample is saturated, the gravimetric moisture content for which the sample starts to be saturated, w_{sat} , can be written


$$w_{sat} = \frac{\phi \rho_w}{(1 - \phi) \rho_s} \quad (\text{A.0.14})$$

B. Old Dalby geological log

 British Geological Survey <small>NATURAL ENVIRONMENT RESEARCH COUNCIL</small>		Project NEE5769N - 'PRIME'		Borehole No. BH 1			
Start date July 2016		Client		Borehole diameter (o.d.) NGR/lat & long 462691,332124			
End date		Locality Name OLD DALBY		Sheet 1			
Drilling method DANDO Terrier		Casing details		Ground level 50m			
Equipment		Flush		Logged by PH (MK) Scale			
				FI Fracture index, fractures per metre, min, (mode) and max			
Description strata, BS 5930:1999	Depth / Thickness m	Reduced level	Depth Hand Vane (small)	Grain size	Fractures structures	Samples/Tests/Core Logging	Field Records
						Flush SPT / return TCR	SCR RQD FI
TOPSOIL 0.07m							
Loose dk. reddish-brown (5YR 2.5/2) rounded sandy m-gravel [FILL] 0.30m	0.07m						
stiff strong brown (7.5YR 4/4) f. sandy SILT w. small inclusions of black organic & soft white calc. nodules + mm lithorelicts	0.34m						
fragments of pottery drain	0.60m						
stiff fissd. reddish-brown (5YR 4/3) clayey SILT w. occas. rounded m-gravel & calcar. inclusions [THRUSINGTON M., WOLSTON F.] (TILL) (sl. calc. angul. gravel)	0.66m						
Uniform firm-v. stiff reddish-brown (5YR 4/3) & mottled light grey (5Y6/1) & reddish-brown (2.5 YR 4/4) silty CLAY w. sandy silt inclusions [THRUSINGTON M.] (TILL) inc. inclusion loose pale red (10R 6/4) med. calc. weath. clast	1.0m						
Discon. irregular (artefacts?)	1.8m						
Uniform stiff reddish-brown (5YR 4/3) w. mottled light grey (5Y6/1) & reddish-brown (2.5 YR 4/4) silty CLAY w. sandy silt inclusions, w. f. gravel (incr. with depth) & occas. c-gravel (angular) of 1st. & sst. & (occas.) coal. (TILL) [THRUSINGTON M.] clast 2.4m	2.0m						
Discon. irreg (artefact)	2.8m						
disturbed material (drilling artefact)	3.0m						
clast c-gravel sl. calc sst.	3.08m						
(TILL) [THRUSINGTON M.]	4.0m						
grey-brown (2.5Y5/2) Discon. irregular siltstone cobble @ 4.7m (prob. artefacts)	4.70m						

Comments — This log is based on a partial inspection of the core (core not slabbed)
 — Handvane conversion (small vane): X 24.52 kPa

B. Old Dalby geological log

 British Geological Survey NATURAL ENVIRONMENT RESEARCH COUNCIL		Project NEE 5769N - 'PRIME'		Borehole No. BH.1							
		Locality Name OLD DALBY		Sheet 2							
Start date July 2016	Client		Borehole diameter Liners: 88mm / 102mm (O.D.)		NGR/lat & long 462691, 332124						
End date					Ground level 50m						
Drilling method Dando Terrier			Casing details		Logged by PH/MK Scale						
Equipment					FI Fracture index, fractures per metre, min, (mode) and max						
Flush											
Description strata, BS 5930:1999	Depth / Thickness m	Reduced level	Loss of Hand Vane (small)	Grain size	Fractures structures	Samples/Tests/Core Logging					Field Records
						Flush return	SPT / TCR	SCR	RQD	FI	
Angul. calcar sst. clast 5.1 Uniform, firm-stiff, brown to dk. brown (7.5YR4/2) gravelly silty CLAY (TILL) [THRUSSINGTON M.]	RUN 6 (88mm)	-4.5 -7.0									
5.84 Loose, uniform brown-dk. br. (6.5YR4/2) m-SAND	5.95 6.0										
Firm dk. olive grey (5Y3/2) silty CLAY w. f-m gravel Stiff v. stiff, lt. grey (5Y6/1) & v. dk. grey (5Y3/1) stiff disturbed (turbulent/flame structure) v. calc. silty CLAY w. f-m gravel [WESTBURY F.]	6.20 6.27	-5.6									
Strong clast (broken) 5Y6/1 SILTSTONE	6.38	-8.0									
Stiff black (5Y 2.5/1) silty CLAY w. occas. angular f-m gravel [WESTBURY F.] discon. irreg. (artefact?)	RUN 7 (88mm)	-5.4									
TD	6.84										
	7.0										
Comments — This log is based on a partial inspection of the core (core not slabbed) — Hand vane conversion (small vane): x 24.52 kPa											